

NAVAL POSTGRADUATE SCHOOL

Monterey, California



**Computer Aided Thermal Analysis of a Technology
Demonstration Satellite (NPSAT1)**

by

Martin Gruhlke

05 May 2003

Approved for public release; distribution is unlimited.

Prepared for: NPS Space Systems Academic Group

20030515 101

THIS PAGE INTENTIONALLY LEFT BLANK

NAVAL POSTGRADUATE SCHOOL


Monterey, California 93943-5000

RADM David Ellison
Superintendent

R. Elster
Provost

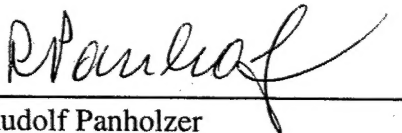
This report was prepared for and funded by the Naval Postgraduate School, Space Systems Academic Group.

This report was prepared by:



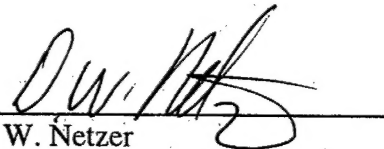
Martin Gruhlke
Leutnant, German Air Force

Reviewed by:

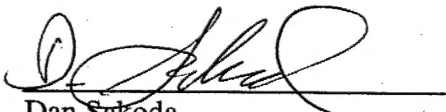


Rudolf Panholzer
Space Systems Academic Group

Released by:



D. W. Netzer
Associate Provost and
Dean of Research



Dan Sakoda
Space Systems Academic Group

THIS PAGE INTENTIONALLY LEFT BLANK

REPORT DOCUMENTATION PAGE			<i>Form Approved OMB No. 0704-0188</i>	
Public reporting burden for this collection of information is estimated to average 1 hour per response, including the time for reviewing instruction, searching existing data sources, gathering and maintaining the data needed, and completing and reviewing the collection of information. Send comments regarding this burden estimate or any other aspect of this collection of information, including suggestions for reducing this burden, to Washington headquarters Services, Directorate for Information Operations and Reports, 1215 Jefferson Davis Highway, Suite 1204, Arlington, VA 22202-4302, and to the Office of Management and Budget, Paperwork Reduction Project (0704-0188) Washington DC 20503.				
1. AGENCY USE ONLY (Leave blank)		2. REPORT DATE May 2003	3. REPORT TYPE AND DATES COVERED Technical Report	
4. TITLE AND SUBTITLE: Title (Mix case letters) Computer Aided Thermal Analysis of a Technology Demonstration Satellite (NPSAT1)			5. FUNDING NUMBERS N/A	
6. AUTHOR(S) Martin Gruhlke, Leutnant German Air Force				
7. PERFORMING ORGANIZATION NAME(S) AND ADDRESS(ES) Naval Postgraduate School Space Systems Academic Group Code (SP), 777 Dyer Rd., Rm 200 Monterey, CA 93943-5000			8. PERFORMING ORGANIZATION REPORT NUMBER NPS-SP-03-001	
9. SPONSORING / MONITORING AGENCY NAME(S) AND ADDRESS(ES) Naval Postgraduate School Space Systems Academic Group Code (SP), 777 Dyer Rd., Rm 200 Monterey, CA 93943-5000			10. SPONSORING / MONITORING AGENCY REPORT NUMBER N/A	
11. SUPPLEMENTARY NOTES The views expressed in this thesis are those of the author and do not reflect the official policy or position of the Department of Defense or the U.S. Government.				
12a. DISTRIBUTION / AVAILABILITY STATEMENT Approved for public release, distribution is unlimited.			12b. DISTRIBUTION CODE	
13. ABSTRACT (maximum 200 words) The thermal control system of a spacecraft is used to maintain all subsystems within their temperature limits. It must be able to deal with different operational states and orbital environments. Theory provides knowledge about the quality of effects of certain designs options, but for a complex system like a spacecraft, simulations are needed for quantification. This thesis has two main purposes. Critical parts concerning thermal control in the current design are identified and the thermal design for NPSAT1 is improved. Furthermore this developed design is analyzed for being appropriate and temperature-time predictions are developed. Both design objectives are accomplished with the help of EDS I-DEAS with Maya's TMG. After defining all constraints and requirements, a thermal FE model is developed, documented, and verified. Simulations with this model are used to track insufficiencies concerning the thermal design. With their help, different design approaches are analyzed to obtain sensitivity information. Proposals for design changes are made. Four worst-case scenarios are defined and the developed design is evaluated with their help. Temperature-time histories are obtained with an emphasis on the temperature sensitive electronic boxes. A special analysis is provided for the connection of the solar cells to the structure.				
14. SUBJECT TERMS FDM, FEM, NPSAT1, Satellite, Spacecraft, Thermal Analysis, Thermal Control			15. NUMBER OF PAGES 169	
			16. PRICE CODE	
17. SECURITY CLASSIFICATION OF REPORT Unclassified	18. SECURITY CLASSIFICATION OF THIS PAGE Unclassified	19. SECURITY CLASSIFICATION OF ABSTRACT Unclassified	20. LIMITATION OF ABSTRACT UL	

THIS PAGE INTENTIONALLY LEFT BLANK

ABSTRACT

The thermal control system of a spacecraft is used to maintain all subsystems within their temperature limits. It must be able to deal with different operational states and orbital environments. Theory provides knowledge about the quality of effects of certain designs options, but for a complex system like a spacecraft, simulations are needed for quantification.

This thesis has two main purposes. Critical parts concerning thermal control in the current design are identified and the thermal design for NPSAT1 is improved. Furthermore this developed design is analyzed for being appropriate and temperature-time predictions are developed.

Both design objectives are accomplished with the help of EDS I-DEAS with Maya's TMG. After defining all constraints and requirements, a thermal FE model is developed, documented, and verified. Simulations with this model are used to track insufficiencies concerning the thermal design. With their help, different design approaches are analyzed to obtain sensitivity information. Proposals for design changes are made. Four worst-case scenarios are defined and the developed design is evaluated with their help. Temperature-time histories are obtained with an emphasis on the temperature sensitive electronic boxes. A special analysis is provided for the connection of the solar cells to the structure.

THIS PAGE INTENTIONALLY LEFT BLANK

ZUSAMMENFASSUNG

Das Wärmeregelsystem eines Raumfahrzeuges wird genutzt, um zu gewährleisten, dass alle Teilsysteme ihre Temperaturgrenzen einhalten. Dies muss für verschiedene Betriebszustände und Umlaufbedingungen gewährleistet sein. Aus der Theorie sind die qualitativen Auswirkungen bestimmter Gestaltungsmöglichkeiten bekannt, aber quantitativ können sie für ein komplexes System wie ein Raumfahrzeug nur mit Simulationen beschrieben werden.

Diese Diplomarbeit hat zwei Hauptziele. Kritische Stellen der gegenwärtigen Bauweise bezüglich der Wärmeregulierung werden aufgefunden und verbessert. Weiterhin wird diese entwickelte Ausführung auf Zweckdienlichkeit untersucht und Temperatur-Zeit Vorhersagen werden gemacht.

Beide Entwicklungsziele werden mit der Hilfe von EDS I-DEAS mit Maya's TMG erreicht. Nachdem alle Bedingungen und Anforderungen definiert sind, wird ein FE-Wärmemodell entwickelt, dokumentiert und überprüft. Mit diesem Modell werden Simulationen durchgeführt, um Unzulänglichkeiten der Konstruktion bezüglich Wärme aufzufinden. Mit ihrer Hilfe werden auch verschiedene Entwurfsannäherungen getestet und Sensitivitätsinformationen gewonnen. Vorschläge für Änderungen der Bauweise werden gemacht. Vier Grenzfallezenarien werden definiert und die entwickelte Bauweise mit ihrer Hilfe bewertet. Temperatur-Zeit Verläufe unter besonderer Berücksichtigung der temperaturempfindlichen Elektronikkomponenten werden gewonnen. Eine spezielle Analyse der Verbindung Solarzellen – Satellitenkörper wird geliefert.

THIS PAGE INTENTIONALLY LEFT BLANK

DECLARATION

Hereby I declare that this Thesis has been created by myself using only the named sources and supplementary equipment.

ERKLÄRUNG

Hiermit erkläre ich, dass die vorliegende Diplomarbeit von mir selbstständig und nur unter Verwendung der angegebenen Quellen und Hilfsmittel erstellt wurde.

Monterey, 14. April 2003

Martin Gruhlke, Lt

THIS PAGE INTENTIONALLY LEFT BLANK

TABLE OF CONTENTS

I.	INTRODUCTION.....	1
II.	NPSAT1	3
	A. MISSION OBJECTIVES.....	3
	B. MECHANICAL STRUCTURE.....	3
	C. PAYLOAD ELECTRONICS.....	5
	1. Subsystems.....	5
	2. Hosted Experiments.....	6
	D. DESIGN PROCESS AND STATUS	7
III.	THERMAL DESIGN.....	11
	A. MODES OF HEAT TRANSFER	11
	B. OPTICAL PROPERTIES.....	14
	C. THERMAL ENVIRONMENTS.....	15
	D. THERMAL CONTROL HARDWARE	18
	E. BOLTED-JOINT INTERFACES	23
IV.	NPSAT1 THERMAL ANALYSIS BACKGROUND	27
	A. CONSTRAINTS AND REQUIREMENTS	27
	B. SOFTWARE AND ANALYTICAL BASICS.....	32
	1. The CAE-Software.....	32
	2. The Analytical Method	33
	C. ANALYSIS PROCEDURE	35
V.	NPSAT1 THERMAL MODEL.....	39
	A. STRUCTURAL MODEL.....	39
	B. MESHING	40
	C. MATERIALS AND PHYSICAL PROPERTIES	46
	D. COMPONENTS.....	47
	1. Structure	47
	2. Heat Generation	48
	E. CONTACT CONDUCTANCES.....	50
	F. ENVIRONMENT.....	52
VI.	DATA-TRANSFER SCRIPT.....	55
VII.	NPSAT1 THERMAL ANALYSIS AND RESULTS.....	59
	A. MODEL VERIFICATION	59
	B. DESIGN EVALUATION AND DEVELOPMENT	63
	1. Initial design	63
	2. Insulation changes.....	68
	3. Changes in surface finishes	71
	4. Heater addition.....	73
	5. Thermostat addition	74

C.	WORST-CASE SCENARIOS	78
1.	Worst-case cold 1	78
2.	Worst-case cold 2	83
3.	Worst-case hot 1	86
4.	Worst-case hot 2	89
D.	SOLAR CELL – STRUCTURE CONNECTION.....	94
VIII.	CONCLUSION AND RECOMMENDATIONS.....	99
	APPENDIX A. PRELIMINARY THERMAL ANALYSIS RESULTS.....	101
	APPENDIX B. EQUATION CORRECTION FROM GLUCK.....	103
	APPENDIX C. BETA ANGLE HISTOGRAM.....	105
	APPENDIX D. POWER BUDGET	107
	APPENDIX E. NPSAT1 DRAWINGS.....	109
	APPENDIX F. BOX BOLT DISTANCES.....	115
	APPENDIX G. EFFECTIVE SOLAR CELL ABSORPTANCE	117
	APPENDIX H. MATERIAL THICKNESSES	119
	APPENDIX I. CAPACITANCE CALCULATIONS	121
	APPENDIX J. GROUND STATION COVERAGE	125
	APPENDIX K. DUTY CYCLES FOR LOW FREQUENCY DEVICES	127
	APPENDIX L. BATTERY HEAT GENERATION	131
	APPENDIX M. CONTACT CONDUCTANCES	133
	APPENDIX N. PYTHON SOURCE CODE.....	137
	LIST OF REFERENCES	139

LIST OF FIGURES

Figure 1.	Expanded view of NPSAT1.....	4
Figure 2.	View factor for radiation exchange between dA_u & dA_v	13
Figure 3.	Energy balance between spacecraft and space.....	16
Figure 4.	Surface properties by type of finish.....	20
Figure 5.	Three-axis satellite thermal control	23
Figure 6.	Heat conductance through contact points.....	24
Figure 7.	Beta angles for NPSAT1 orbit.....	28
Figure 8.	NPSAT1 orbits: a) beta angle 0° , b) beta angle $+60^\circ$	29
Figure 9.	Calculation points in the Element Center of Gravity method.....	35
Figure 10.	Thermal modeling and analyzing process.....	36
Figure 11.	Patch antennas and ground plate configuration.....	39
Figure 12.	Relations in an equilateral triangle.....	42
Figure 13.	Beam cross section for longeron mesh.....	44
Figure 14.	NPSAT1 mesh.....	45
Figure 15.	Flowchart of Python script for TEMPF extraction.....	57
Figure 16.	Flowchart of Python script for REPF extraction.....	58
Figure 17.	Capacitance comparison for CERTO.....	59
Figure 18.	Spacecraft temperatures during orbit.....	60
Figure 19.	Post-processed elements of solar cell mesh.....	61
Figure 20.	Solar cell temperatures on normal orbit.....	64
Figure 21.	Third deck components and patch antenna temperatures on normal orbit.....	65
Figure 22.	Subsystem temperatures on first and second deck of normal orbit.....	65
Figure 23.	Subsystem temperatures on third deck of normal orbit.....	66
Figure 24.	Deck temperatures on normal orbit.....	66
Figure 25.	Heat exchange of battery during normal orbit.....	68
Figure 26.	Transient phenomenon over a whole day.....	69
Figure 27.	Insulation comparison for battery temperature.....	71
Figure 28.	Finish comparison for battery temperature.....	73

Figure 29.	Micro heater 5 W.	74
Figure 30.	Battery temperature with constant 5 W heater input.	74
Figure 31.	Heat flow structure to battery with thermostat.	77
Figure 32.	Duty cycle of heater and adjusted battery waste heat.	77
Figure 33.	Solar cell temperatures of worst case 1.....	79
Figure 34.	Patch antenna temperatures of worst case 1.	79
Figure 35.	Subsystem temperatures on first and second deck of cold case 1.....	80
Figure 36.	Subsystems on third deck of cold case 1.	80
Figure 37.	Deck temperatures of cold case 1.	81
Figure 38.	Subsystem temperatures on first and second deck of cold case 2.....	84
Figure 39.	Subsystem temperatures on third deck of cold case 2.	84
Figure 40.	First deck temperatures with and without CERTO operation.....	85
Figure 41.	Solar cell temperatures of hot case 1.	87
Figure 42.	Subsystem temperatures on first and second deck of hot case 1.	88
Figure 43.	Subsystem temperatures on third deck of hot case 1.....	88
Figure 44.	Solar cell temperatures of hot case 2.	90
Figure 45.	Patch antenna temperatures of hot case 2.	91
Figure 46.	Subsystem temperatures on first and second deck of hot case 2.	91
Figure 47.	Subsystem temperatures on third deck of hot case 2.....	92
Figure 48.	Deck temperatures of hot case 2.	92
Figure 49.	Post-processed elements in solar cell – structure analysis.....	95
Figure 50.	Solar cells and structural panels in cold case.....	96
Figure 51.	Solar cells and structural panel in hot case.	96

LIST OF TABLES

Table 1.	Passive and active thermal control hardware.....	18
Table 2.	Orbital time parameters.....	29
Table 3.	Orbital temperatures and power requirements.....	30
Table 4.	Deck mesh parameters for free meshing.....	43
Table 5.	Optical properties of initially used materials for BOL.	46
Table 6.	Heat dissipation of high frequency devices.	49
Table 7.	Heat dissipation of low frequency devices.	49
Table 8.	Power scenarios.	62
Table 9.	Optical BOL and EOL properties for worst-case scenarios.....	63
Table 10.	Normal orbit parameters.	64
Table 11.	Insulation changes and results.	70
Table 12.	Finish changes and results.	72
Table 13.	Thermostat changes and results.	75
Table 14.	Cold case 1 parameters.	78
Table 15.	Heater power requirements of cold case 1.....	82
Table 16.	Cold case 2 parameters.	83
Table 17.	Heater power requirement of cold case 2.	86
Table 18.	Hot case 1 parameters.	87
Table 19.	Heater power requirements of hot case 1.....	89
Table 20.	Hot case 2 parameters.	90
Table 21.	Heater power requirements of hot case 2.....	94

THIS PAGE INTENTIONALLY LEFT BLANK

LIST OF ABBREVIATIONS

ACS	attitude control subsystem
BOL	beginning of life
C&DH	command and data handling subsystem
CAD	computer aided design
CAM	computer aided manufacturing
CCD	charge coupled device
CDR	critical design review
CERTO	coherent electromagnetic radio tomography
COTS	commercial off-the-shelf
CPE	configurable processor experiment
EOL	end of life
EPS	electrical power subsystem
FDM	finite difference method
FEM	finite element method
FPGA	field-programmable gate array
GPS	Global Positioning System
I/O	input/output
ICD	interface control document
IR	infrared
ITJ	improved triple junction (solar cells)
JPEG	Joint Picture Experts Group
LEO	low Earth orbit
MEMS	micro-electromechanical system
NPS	Naval Postgraduate School
NPSAT	NPS Spacecraft Architecture and Technology Demonstration Satellite
NRL	Naval Research Laboratory
PANSAT	Petit Navy Amateur Satellite

PCB	printed circuit board
PDR	preliminary design review
RAM	random access memory
ROM	read only memory
SC	solar cell
SMS	solar cell measurement system
SSAG	Space Systems Academic Group
TMG	Thermal Model Generation™
TMR	triple-modular, redundant (computer)
VISIM	visible wavelength imager
IR	infrared
MLI	multilayer insulation
UV	ultraviolet

NOMENCLATURE

<u>Symbol</u>	<u>Name</u>	<u>Unit in SI base units</u>
A	area	m^2
C	thermal conductance	$\frac{W}{K}$
D	diameter	m
E	emissive power	$\frac{W}{m^2}$
e	coefficient of thermal expansion	$\frac{1}{K}$
E'	effective modulus of elasticity	$\frac{N}{m^2}$
F	factor	
G	irradiation	$\frac{W}{m^2}$
h	heat-transfer coefficient	$\frac{W}{m^2 \cdot K}$
H	microhardness	$\frac{N}{m^2}$
k	thermal conductivity	$\frac{W}{m \cdot K}$
l	thickness	m
m	slope	
P	heat generation	W
p	pressure	$\frac{N}{m^2}$
q	heat transfer rate	W
q''	heat flux	$\frac{W}{m^2}$
r	radius	m
T	temperature	K
t	time	s
Y	yield stress	$\frac{N}{m^2}$

W	work	J
α	absorptivity	
ε	emissivity	
θ	angle	$^{\circ}$
λ	wavelength	m
η	efficiency	
ρ	Stefan-Boltzmann constant	$\rho = 5.67 \cdot 10^{-8} \frac{W}{m^2 \cdot K^4}$
σ	root-mean-square roughness	m
τ	torque	$N \cdot m$

Super- and subscripts

<i>abs</i>	absorbed
<i>al</i>	aluminum
<i>b</i>	bolted
<i>bl</i>	black body
<i>c</i>	contact
<i>ds</i>	direct solar
<i>e</i>	elastic
<i>ecl</i>	eclipse
<i>eff</i>	effective
<i>er</i>	Earth-reflected
<i>et</i>	Earth thermal
<i>f</i>	finish
<i>g</i>	gas
<i>h</i>	harmonic mean
<i>i</i>	installation
<i>int</i>	internal
<i>j</i>	joint

<i>lin</i>	linear
<i>m</i>	mean
<i>max</i>	maximum
<i>p</i>	plastic
<i>pg</i>	packing
<i>pl</i>	plate
<i>r</i>	radiation
<i>ref</i>	reflected
<i>S</i>	screw
<i>s</i>	surface
<i>sc</i>	spacecraft
<i>sol</i>	solar
<i>ss</i>	stainless steel
<i>v</i>	view
<i>x</i>	direction
<i>λ</i>	spectral

THIS PAGE INTENTIONALLY LEFT BLANK

ACKNOWLEDGMENTS

I would like to thank the participating professors Prof. Panholzer, Prof Rothe and Prof. Zeidler for supporting this extraordinary chance to do my thesis in aerospace engineering at the Space Systems Academic Group at the Naval Postgraduate School in the United States of America. Furthermore I would like to thank my advisor at the Space Systems Academic Group, Dan Sakoda, and the other members of staff, Jim Horning, Ron Phelps, and David Rigmaiden. They offered every support they could at every time. I would also like to thank Sherry del Bando for spellchecking this work.

THIS PAGE INTENTIONALLY LEFT BLANK

I. INTRODUCTION

Satellites have reached a wide variety of usage. Their field of application includes hosting experiments as well as providing equipment for direct use on Earth. Among the experiments there are some for exploring space and others for research in micro-gravity that will be beneficial for use on Earth. Among the applications for daily use there are, for instance, communications and weather forecasts. Especially the military, like the Naval Postgraduate School (NPS), is interested in satellites. It is an advantage in the area of defense compared to countries that do not possess this technology. Their applications are partly very similar to the civilian usage, like communications or surveillance. There are also special applications like putting weapons into space. The global positioning system (GPS) is a good example of how military inventions can improve our daily life.

All these benefits raise the wish for more satellite usage. Like with every product, larger quantities and lower prices go hand in hand. The development of small low cost satellites is consequently the next step after being able to build satellites at all. NPSAT1 is supposed to demonstrate that taking this step is possible today.

As a consequence, the wide usage of satellites raises the need for more engineers being able to deal with spacecrafts. The development of small satellites provides educational opportunities to schools like NPS that are not one of the major spacecraft companies.

The engineering work in this thesis is done using a computer simulation. This allows dealing with far more complex issues than is possible with theoretical methods like calculations. Compared to a series of tests it is, especially in the development of low cost equipment, of great benefit for financial reasons. But tests are still important in batch productions, especially, when there is no possibility to correct mistakes like with a satellite in space. Therefore tests are needed at least to verify the simulation results.

This thesis evaluates the thermal control system of NPSAT1. The importance of thermal issues in the design and therefore of thermal analysis of spacecrafts can be recognized in the failure of NASA's Wide-Field Infrared Explorer (WIRE) in 1999.

Electric power, created at the start-up of a component, reached pyrotechnics and ejected a cover too early in the mission. Without this cover the frozen hydrogen, which was supposed to cool a part of a telescope, was exposed to the sun. The hydrogen warmed and vented into space within 48 hours. The telescope was not usable anymore.

All in all it can be said, that satellites like NPSAT1 are a vital part of further development of opportunities in space. In particular, thermal computer analysis of small satellites is a cost- and effort-efficient way to ensure mission success.

II. NPSAT1

A. MISSION OBJECTIVES

The NPS Spacecraft Architecture and Technology Demonstration Satellite (NPSAT1) is a low-cost spacecraft developed and built by officer students, faculty and staff of the Space Systems Academic Group (SSAG) of the Naval Postgraduate School (NPS). It is a three-axis-stabilized satellite, the most common spacecraft configuration today [Ref. 5]. The orbit for NPSAT1 is a low earth orbit (LEO, typically up to 2,000 km) with an altitude of 560 km. The altitude was chosen to be in a low atmosphere density, which extends lifetime (chapter III.C) and makes attitude control easier. Low earth orbits lead to shorter periods, about 1 h 40 min for NPSAT1. The shape of NPSAT1's orbit is circular. The inclination of the orbit, which is the angle between the plane of the equator and the plane of the orbit, is 35.4 degrees. This orbit allows for good communication with the NPS ground station, located at 36.6 ° latitude.

The primary objective of the satellite project is the education of officer students at NPS in Space Systems. One goal concerning the satellite itself is to build and operate it with commercial off-the-shelf (COTS) components to decrease development time, reduce costs, and increase reliability in software development. This means employing standards already widely in use and flying consumer or industrial grade electronics. [Ref. 15] Another goal is to provide a platform for other experiments in space.

B. MECHANICAL STRUCTURE

NPSAT1 is a twelve-sided cylinder with four decks. The cylinder sides have body-mounted solar cells for energy conversion and also for experimental reasons. On the nadir facing side, as well as on the zenith side, a ground plate for antennas is attached. The nadir facing side also carries the Lightband Separation System, for separation from the launch vehicle (Delta IV) during deployment. This design is the result of different design approaches, which was chosen mainly for mechanical reasons. Since NPSAT1 is a secondary payload aboard the Delta-rocket it had to be designed very robust. No attempt

was made to save weight, following the manifesting from the mission, of which NPSAT1 will be a part. The location of the components is also more or less defined. Stress analyses were performed. Thus, location of components is fixed for this study. The material used for the structure is aluminum 6061-T6 with different coatings, which is described in chapter V.C in further detail. Fig. 1 shows an expanded view of NPSAT1. [Ref. 17] The shown coordinate system will be used in the whole thesis.

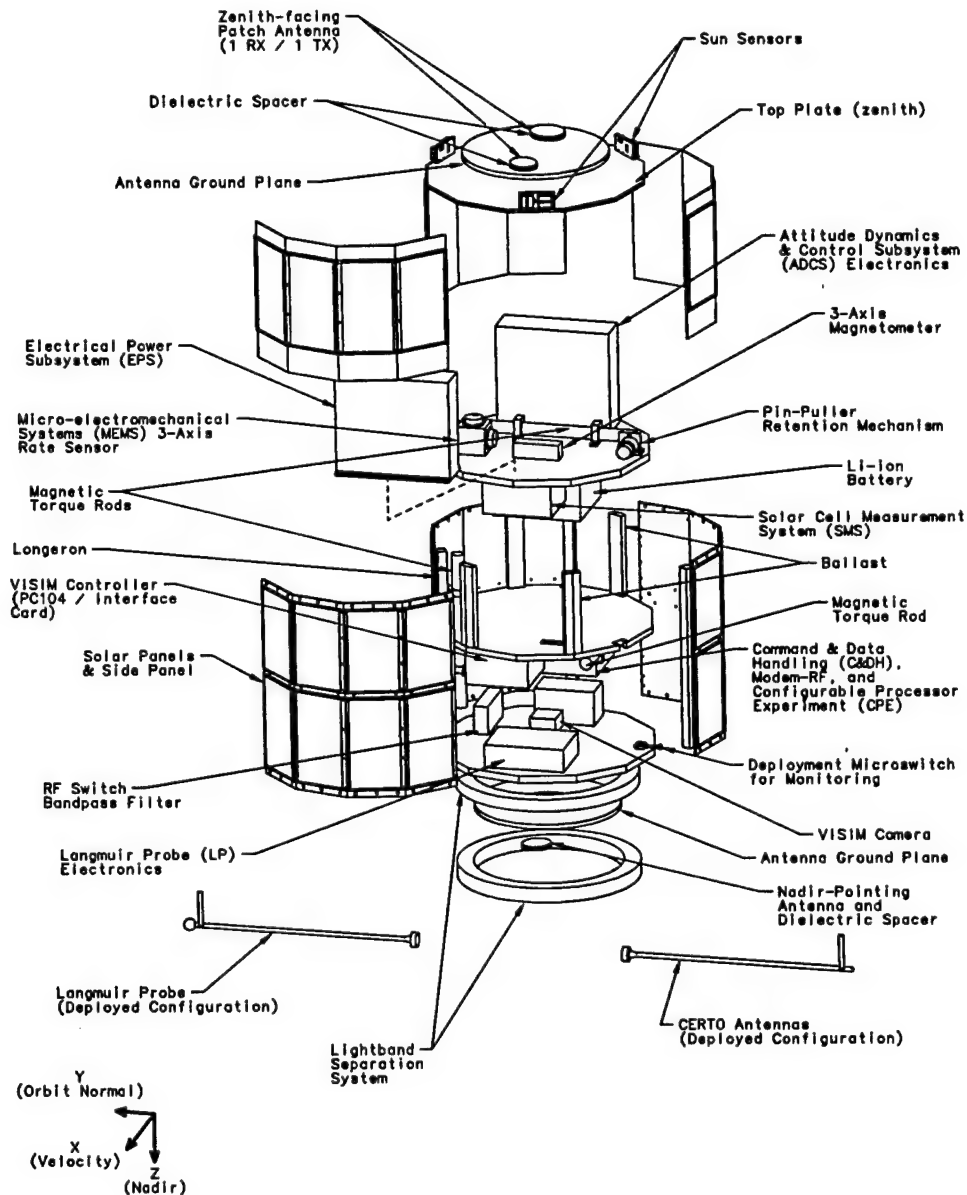


Figure 1. Expanded view of NPSAT1.

C. PAYLOAD ELECTRONICS

1. Subsystems

The electrical power subsystem (EPS) generates and distributes electrical power to the spacecraft, including solar arrays, batteries, solar-array controllers, power converters, electrical harnesses, battery-charge-control electronics, and other components. In this thesis the expression EPS refers to the controller box labeled EPS in Fig.1. Power is generated by solar cells body-mounted to all sides of the spacecraft, except at the top and bottom. Not using deployable arrays excludes the risk of mechanical failure to deploy. Two thirds of the solar cells are commercial Improved Triple Junction (ITJ) Solar Cells provided by Spectrolab. The efficiency is about 26.8 %, with a value of 22.5 % at end of life. [Ref. 19] One third of the cells are experimental also provided by Spectrolab. The battery, being part of the technology demonstration, will be Lithium-ion. This type has a high energy density. The EPS control electronics consists of a processor board with all the digital logic and an analog/switching board for power switching and telemetry gathering.

The NPSAT1 Radio Frequency subsystem (RF) is used to communicate with the satellite from the ground. It consists of receivers, transmitters, antennas, and state-of-health sensors.

The NPSAT1 Command & Data Handling subsystem (C&DH) is built using commercial hardware. It consists of electronic boards for the radio frequency subsystem (mainly amplifiers), mass storage (flash disk), A/D conversion and input/output (I/O), the power supply, a modem and the Configurable Processor Experiment (CPE). All boards are connected on an electronic bus. The operating software is a robust and highly configurable embedded Linux. Thus the desktop-PC software development is 100 % compatible with flight hardware.

The Attitude Control subsystem (ACS) senses and controls the vehicles attitude and rates. It consists of magnetic torquers as actuators, a three-axis magnetometer for sensor input, and the ACS controller. This design approach is novel and provides a very low cost solution. Onboard information of the orbit position is used as input to a table-lookup to obtain the magnetic field vector at this position. This is compared to

magnetometer information and the control algorithm attempts to null the error between the two values. Like the EPS, the ACS consists of a processor board and an analog/switching board (to drive the torque rods, taking measurements from different sensors and provide power for some components).

Another technology demonstration is the use of nonvolatile ferroelectric RAM. This has the advantage of being radiation-tolerant and will be used in EPS and ACS.

2. Hosted Experiments

The envelope containing the C&DH also hosts a configurable processor experiment (CPE), on a single electronic circuit board, with field-programmable gate arrays (FPGA). The gate arrays allow in-flight upgrades to the processor configuration. Two scenarios are considered: at first, the FPGA will be a triple-modular, redundant (TMR) computer. In the second scenario the FPGA will be a hardware image compressor for the production of JPEG representations of the VISIM data.

The nadir-facing side hosts a visible wavelength imager (VISIM), which is basically a COTS CCD-camera. The VISIM controller is a PC/104 board with a 486 processor. This experiment is only turned on for short times to take and store pictures. A typical picture will cover an area of 200 km by 150 km or smaller. Two compressions are used: a lossless one and a lossy JPEG compression for a preview of the picture. Command and storage is done in the C&DH.

The Solar Cell Measurement System (SMS) is an NPS experiment for flight demonstration of solar cells. The SMS will collect current-voltage and temperatures of the solar cells at specific points. The controller is very similar to EPS and ACS. A control algorithm is stored in a ROM but a new one can be uploaded during on-orbit operation. Experimental cells on the solar arrays will also be monitored for performance over the spacecraft's life.

The Coherent Electromagnetic Radio Tomography (CERTO) experiment and Langmuir Probe are provided by the Naval Research Laboratory (NRL). CERTO is a

radio beacon, which will allow measurements of electron content of the ionosphere. The Langmuir probe will provide on-orbit sensors for this purpose.

The last experiment is the three-axis Micro-Electromechanical system (MEMS) rate sensor. This is a COTS equipment like the VISIM system.

D. DESIGN PROCESS AND STATUS

Every spacecraft development can be divided into typical phases. This chapter explains these phases utilizing the NPSAT1 development process with focus on thermal issues. This leads to the development status of NPSAT1.

The first phase is the concept definition phase, resulting in a definition of a baseline spacecraft-configuration concept. Concerning thermal issues this meant to define and analyze, an approach to the thermal control of the spacecraft. In such a phase all elements (operational electronics, payload electronics, batteries, sensors, propulsion, antennas, etc.) for all mission phases (prelaunch testing through on-orbit operations) are taken into account. Standard thermal control techniques, like finishes and location of components, were chosen. More concern was focused on thermal-control elements with significant system-level impacts because of operating temperature limits, power requirements and development complexity, for instance batteries and solar cells. But no specific designs for these components were chosen at this early stage, because "... the input parameters upon which the thermal design is based usually change quickly, ..." [Ref. 5, p. 524].

The next stage is called validation, which consists of refining concept-phase studies and determining on a top-level stage what technologies and capabilities can realistically be achieved. The result of this phase is generally a number of documents like the interface control document (ICD). This document consists of drawings and requirements defining all the connections, mechanical as well as electrical, from the satellite to the launch vehicle.

This study is part of the so-called full-scale development. The overall effort in this phase is similar to that in the concept definition phase but in much greater detail. "The

spacecraft design is still fairly flexible at this point, and significant changes in configuration, payloads, and subsystem designs (including thermal) should be expected ..." [Ref. 5, p. 529]. Concerning thermal control the design at this point is somewhat flexible in the selection of thermal control coatings and heater needs. Typical key requirements of the full-scale development, as shown in the following list [Ref. 5], have to be identified:

- Range of mission orbits
- Normal attitude(s) of satellite
- Launch-phase configurations and attitudes
- Ground cooling needs
- Autonomy requirements
- Attitudes during stressed/failure modes
- Temperature limits and reliability requirements
- Equipment power dissipation and operating modes
- Thermal-distortion budgets
- Launch-system interfaces
- Interfaces with other subsystems
- Special thermal-control requirements for batteries etc.

NPSAT1 is categorized as a class D effort (minimum acquisition costs) according to military standards [Ref. 3 and Ref.15]. For such a spacecraft the following thermal evaluation steps apply:

- A computer thermal model is not required
- Thermal verification is not required
- Unit acceptance and qualification testing is not required
- Experiment or vehicle acceptance testing is required, but qualification testing is not required

- The thermal uncertainty margin between the thermal model predictions and acceptance testing is 11 ° C, and qualification thermal margin is 0 ° C (because no qualification testing is required)

Low cost programs contain more risk-taking than programs with a higher effort in time and money. In order to minimize these risks NPSAT1 development goes beyond class D requirements concerning thermal control.

The time between the preliminary design review (PDR) and a critical design review (CDR) is the time when most of the design and analysis work takes place. For the CDR, which took place about six month prior to the beginning of this work, a preliminary thermal analysis was performed. This was a very rough simulation. In fact it was just a cylinder with possible thermal finish properties exposed to hot and cold case orbits. However it was of great use, because it offered an idea about initial temperatures and the choice of parameters, which depend on temperatures, for this work. Results of these simulations are enclosed in appendix A. Also The Aerospace Corporation raised requirements for a more detailed thermal analysis in Ref. 23 and in Ref. 24. These are addressed in detail in chapter IV.A. During the work for this thesis the delta-critical design review (Δ -CDR) was passed and the status of the overall NPSAT1 development can be described as 85 – 90 % done. The delta-CDR dealt with concerns raised at the CDR. From CDR to launch, the focus is on hardware and not on concepts. This means addressing outcomes of the CDR and manufacturing or purchasing parts as well as planning and performing tests, for instance thermal and vibrations test. Also development and manufacturing of test equipment might be part of this phase. Concerning thermal issues, the concept phase had not ended. The most important event for the thermal engineer is the thermal-balance test. "In any event, the thermal-balance test is the critical verification of the thermal design, and a conclusive test is considered mandatory to program success." [Ref. 5, p. 534]

The last phase is the operational phase. This begins with delivery of the spacecraft for integration with the launch vehicle. For NPSAT1 this phase will need no support from a thermal engineer. Launch and on-orbit activity will be covered by sensor surveillance.

THIS PAGE INTENTIONALLY LEFT BLANK

III. THERMAL DESIGN

A. MODES OF HEAT TRANSFER

This chapter gives basic knowledge on how heat transfer works and how it can be calculated. The focus is strongly on heat transfer in space. Special space related topics are discussed in further detail whereas detailed fundamentals can be obtained from Ref. 7. Heat transfer is energy in transit due to a temperature difference. There are three different ways of heat transfer.

The first one is *conduction*. In this mode energy is transferred from the higher energetic to the lower energetic particles. This takes place on an atomic and molecular basis. Higher temperatures are associated with higher molecular energy and this energy is transferred through the constantly occurring collision between neighboring molecules. If there is a temperature gradient, heat is transferred in the direction of decreasing temperature. This takes place within materials and at every place where materials are in direct contact, for example at bolted joints in a spacecraft. The rate equation to calculate the quantity of the heat flux in the very simple case of a one-dimensional plane wall is (Fourier's law) [Ref. 7]:

$$q_x'' = -k \cdot \frac{dT}{dl} \quad (\text{III.1})$$

with: q_x'' heat flux in $\frac{W}{m^2}$

k thermal conductivity in $\frac{W}{m \cdot K}$

$\frac{dT}{dl}$ temperature gradient in direction of heat transfer in $\frac{K}{m}$

Multiplication by the diameter of the heat transfer area gives the heat flow rate in Watts.

Another mode of heat transfer is *convection*. It consists of two mechanisms. One is the random molecular motion (diffusion) and the other is the macroscopic motion of a fluid. Convection is divided into forced convection, as a result of a pressure difference,

and free convection, as a result of gravity or density variations. Since there is no fluid present, atmospheric convection is absent in space.

The last mode of heat transfer is *radiation*. Unlike the other heat transfer mechanisms mentioned previously, radiation does not require any material medium. Radiation is most effective in a vacuum, like in space. One part of radiation is an emission of energy by matter of a finite temperature. Energy transportation is done by electromagnetic waves. The emission depends on surface properties. An upper limit for emissive power is given by the Stefan-Boltzmann law [Ref. 7]:

$$E_{bl} = \rho \cdot T_s^4 \quad (\text{III.2})$$

with: E_{bl} emissive power of blackbody in $\frac{W}{m^2}$

ρ Stefan-Boltzmann constant ($\rho = 5.67 \cdot 10^{-8} \frac{W}{m^2 \cdot K^4}$)

T_s absolute temperature of the surface (K)

Every material and every finish has its specific optical properties. One of them measures how effective a surface emits energy compared to a black body. This unitless value is called emissivity (ε) with values between $0 \leq \varepsilon \leq 1$. It represents the total emissive power of a real surface at temperature T compared to the total emissive power of a black body surface at the same temperature in percent. With this value equation III.2 is transformed into:

$$E = \varepsilon \cdot \rho \cdot T_s^4 \quad (\text{III.3})$$

Another part of radiation is the absorption of incident radiation. This energy is called irradiation (G). The related optical material property is the absorptivity (α) with a value $0 \leq \alpha \leq 1$. The following equation quantifies the absorbed irradiation [Ref. 7]:

$$G_{abs} = \alpha \cdot G \quad (\text{III.4})$$

For opaque surfaces

$$G_{ref} = (1 - \alpha) \cdot G \quad (\text{III.5})$$

describes the reflected irradiation.

A third part of radiation is transmission, which applies to semitransparent surfaces. Since there are no semitransparent surfaces in the spacecraft this phenomenon is not of interest for the following studies. Reflection as well as transmission has no influence on the thermal energy of matter, because their emission and absorption are the same.

The energy exchange via radiation between two surfaces depends, besides the material, on the way they view each other. The calculation is done with the help of view factors. These view factors are already calculated for a lot of surface configurations. All these are based on the general view factor equation [Ref. 7]:

$$F_{uv} = \frac{1}{A_u} \cdot \int_{A_u} \int_{A_v} \frac{\cos \theta_u \cdot \cos \theta_v}{\pi \cdot r^2} dA_u dA_v \quad (\text{III.6})$$

The angles and surfaces can be obtained from Fig. 2 [Ref. 7]:

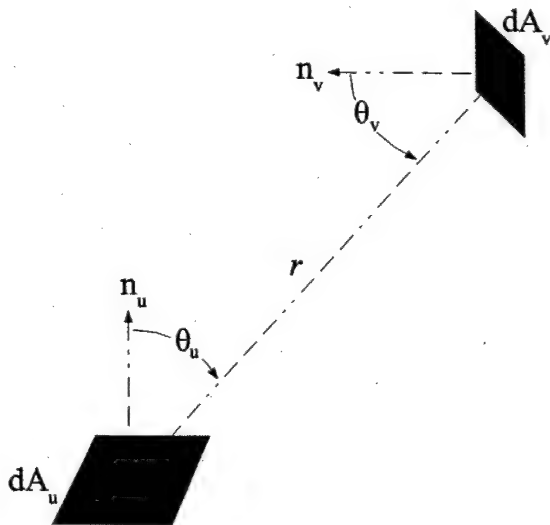


Figure 2. View factor for radiation exchange between dA_u & dA_v .

For the simple case of two black surfaces there is no reflection. Then the net rate at which radiation leaves surface u is the same as the net rate at which surface v gains radiation and can be described by [Ref. 7]:

$$q_{uv} = A_u \cdot F_{uv} \cdot \rho \cdot (T_u^4 - T_v^4) \quad (\text{III.7})$$

For real conditions, where surfaces are not black and more than two surfaces view each other, two major calculation methods are known. The Oppenheim method uses a radiosity approach. Radiosity is the sum of all the radiant energy leaving a surface (emission and reflection). For every surface in an enclosure a radiosity node is created, which is coupled to its parent with a conductance equal to $\rho \cdot A \cdot \varepsilon / (1 - \varepsilon)$. These new surface elements are then coupled using the black body view factor matrix. This approach allows efficient and accurate modeling of temperature dependent emissivity values, since it isolates the emissivity dependence. [Ref. 7] The Gebhardt method uses gray body view factors. They are defined like black body view factors except that it also accounts for intermediate reflections by other surfaces. The radiation heat transfer using this method is described by equation (III.7) multiplied with the emissivity ε . They are calculated by a matrix inversion process, using the black body view factors and the surface properties.

B. OPTICAL PROPERTIES

The optical properties emissivity (ε) and absorptivity (α) are considered to be material (surface) properties. They are used in energy balance equations for radiation.

Emissivity as defined in terms of emission intensity depends on spectrum and direction. From a definition of spectral directional emissivity (λ represent the wavelength) the total hemisphere emission can be derived [Ref. 7]:

$$\varepsilon = \frac{E(T)}{\rho \cdot T^4} = \frac{\int_0^\infty \varepsilon_\lambda(\lambda, T) \cdot E_{\lambda,bl}(\lambda, T) d\lambda}{\rho \cdot T^4} \quad (\text{III.8})$$

Equation (III.3), which is used in thermal control, can be found in this formula. Equation (III.8) shows the dependencies of emissivity. This formula uses average values for all directions and integrates over all wavelengths.

The value for absorptivity does not only depend on the material but also on the nature of irradiation [Ref. 7]. In analogy to equation (III.8) a formula for total hemisphere absorption is derived from the concept of spectral directional incident intensity. The equation is [Ref. 7]:

$$\alpha = \frac{G_{abs}}{G} = \frac{\int_0^{\infty} \alpha_{\lambda} \cdot G_{\lambda}(\lambda) d\lambda}{\int_0^{\infty} G_{\lambda}(\lambda) d\lambda} \quad (III.9)$$

This formula contains equation (III.4). Measurements have shown, that the solar radiation is approximately that from a black surface at 5773 K. [Ref. 9] Solar absorptivity is usually used for thermal control. Based on equation (III.9) solar absorptivity is calculated from [Ref. 9]:

$$\alpha^{sol} \approx \frac{\int_0^{\infty} \alpha_{\lambda} \cdot E_{\lambda,bl}(\lambda, 5773K) d\lambda}{\int_0^{\infty} E_{\lambda,bl}(\lambda, 5773K) d\lambda} \quad (III.10)$$

where $E_{\lambda,bl}(\lambda, 5773K)$ is the spectral emission from a black surface at 5773 K.

Solar radiation is concentrated in the short wavelength region of the spectrum, whereas the emission of most surfaces takes place at much longer wavelength. Therefore, the solar absorptivity of a surface may vary from its emissivity. The ratio α/ϵ is an important engineering parameter. Small values help to reject heat from a surface; large values help to collect solar energy.

C. THERMAL ENVIRONMENTS

Heat sources for the spacecraft are its components and the environment to which it is exposed. The electronics are either continuously "on" or use duty cycles, like in

some of the experiments flown on NPSAT1. In the space environment three significant heat sources are present: direct sunlight, sunlight reflected off Earth (called albedo) and infrared (IR) energy emitted from Earth. The mode of heat transfer, which applies to all of them, is radiation. The spacecraft's temperature is the result of a balance between absorbed and emitted energy of all of these sources. This is illustrated in Fig 3 [Ref. 5].

In low Earth orbits, like NPSAT1 uses, the spacecraft altitude is small compared to the Earth's diameter. If the covered surface of the Earth changes due to the movement of the satellite on its orbit cycle, this can lead to temperature changes of sensitive parts of the spacecraft. [Ref. 5]

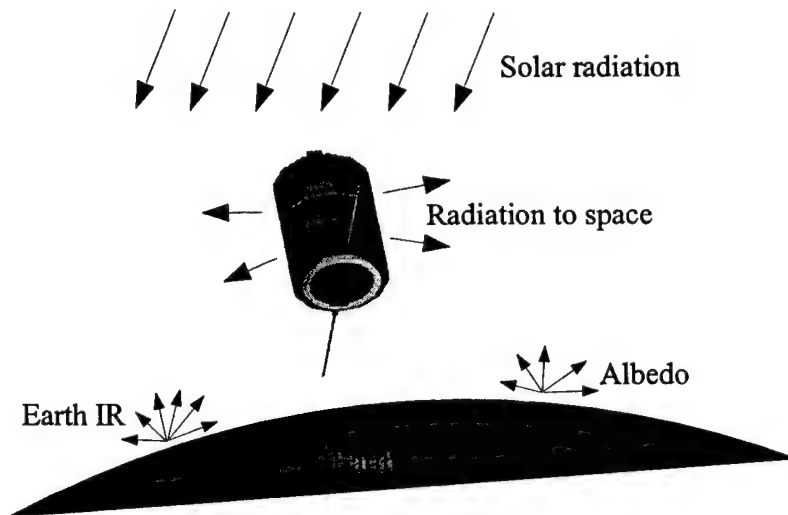


Figure 3. Energy balance between spacecraft and space.

The sun is the greatest of the external heat sources mentioned and is fairly stable. The solar radiation varies only within 1 %. But since the Earth orbits elliptically around the sun, the incident energy varies approximately ± 3.5 %. At the Earth mean distance from the sun the value is called solar constant and is 1367 W/m^2 (1358 W/m^2 [Ref. 16]). June solstice has the lowest value (1322 W/m^2) and December solstice has the highest (1414 W/m^2). [Ref. 5] Also wavelength has an influence on solar intensity, but this is included in these values.

The sunlight reflected from a planet is referred to as albedo (from the Latin *albus*, for whiteness). It is considered to be in the same spectrum as solar radiation. The planets

surface plays a role in this value as well as latitude, because of sun angle, cloud coverage etc. "These variations make selection of the best albedo value for a particular thermal analysis rather uncertain, and variations throughout the industry are not unusual." [Ref. 5, p. 23] Even if this value might be assumed fixed, the heat flux reaching the spacecraft varies during its orbit. The reason for this is, that the local incident energy per unit area decreases with the cosine of the angle from the subsolar point (the point where the sun is overhead). [Ref. 14] The value of albedo is often given as a percentage of the Earth IR.

The energy emitted from the earth varies much with local temperatures and cloud coverage. Highest values appear at tropical and desert regions. Earth IR decreases with latitude. Cloud coverage lowers Earth IR, because cloud tops are cold and clouds block radiation. These variations are significant but not as severe as the variations in albedo. [Ref. 5] The wavelength of Earth IR is approximately the same as the wavelength of the spacecraft's radiation and therefore very different from the wavelength of radiation from the sun. Ref. 9 points out, that emission is concentrated in the spectral region from approximately 4 to 40 μm , with a peak at 10 μm , because of the dependence on temperature, which ranges typically from 250 K to 320 K. This has a significant impact on the performance of thermal control hardware like radiator surfaces. The emissive power of the Earth's surface may be computed using equation III.3.

One of the heat sources that are ignored for NPSAT1 thermal analysis is free molecular heating. Free molecular heating describes the heating that occurs from molecules hitting the spacecraft in outer reaches of the atmosphere. This heat source is only effective for orbit altitudes below 180 km [Ref. 4].

Another ignored heat source is charged particle heating. In room-temperature environments it is weak compared to the other four heat sources: "Heating caused by charged particles in orbit [...] is very low and can be justifiably ignored ..." [Ref. 9, p. 87]. It is relevant only for systems at cryogenic temperatures, which NPSAT1 is not.

D. THERMAL CONTROL HARDWARE

“The purpose of a thermal-control system is to maintain all of a spacecraft’s components within the allowable temperature limits for all operating modes of the vehicle, in all of the thermal environments it may be exposed to” [Ref. 5, p. 71]. This leads to a better performance and an extended lifetime. Arrangements to reach this goal can be divided in two main groups: active and passive measures. Passive design does not use any heaters or any active mechanical or fluid devices. Table 1 provides an overview of thermal control hardware. In general every thermal control feature has an influence on other technical fields. On the other hand, some thermal control possibilities may be impossible for the current design, because of other requirements, like mechanical constraints. Typical for thermal design is, that components get too hot, therefore energy has to be conducted to space, used as a heat sink.

This chapter presents an overview of thermal control hardware that could be considered in the following chapters, i. e. in the thermal analysis. Detailed descriptions of all other thermal control hardware listed in Table 1 can be found in Ref. 4 and Ref. 5.

<i>Passive</i>	<i>Active</i>
fixed geometry	moveable geometry, or appendages
surface finishes	variable conductance heat pipes
insulations	(thermostatic) heaters
heat switches	louvers (electrically controlled)
phase change materials	
radiators	
simple heat pipes	
louvers (bimetallic)	

Table 1. Passive and active thermal control hardware

One of the basic construction elements with impact on thermal control is the *shape* of the spacecraft. Geometry influences the magnitude of a surface and therefore the sections taking part in radiation with space. Solar cells for example can be directly mounted to the body of the spacecraft or to special arrays. Location of components also influences thermal control. Components with the danger of getting too cold can be placed near hot components. Also within the boxes and on electric circuit boards a lot of thermal control can be achieved in this way.

Surface *finishes* are very well developed and are available for different purposes. Thermal coatings are the spacecraft's interface with space. The applying form of heat transfer is radiation. Since the optical properties, which account for radiation, depend on wavelength (see chapter III.C), thermal finishes are wavelength-dependent. Accordingly, they can be divided into four groups [Ref. 9]:

- Solar reflector (low α/ϵ ratio)
- Solar absorber (high α/ϵ ratio)
- Flat reflector (reflect throughout spectral range)
- Flat absorber (absorb throughout spectral range)

What is expected from a thermal coating is illustrated in Fig. 3: An energy balance between all the heat sources at the desired temperature.

Typical solar reflectors are second-surface mirrors, white paint, and silver- or aluminum-backed Teflon. Often-used finishes to minimize heat transfer in both directions are polished metals, like aluminum foil or gold plating. An overview of materials for different purposes is given in Fig. 4 [Ref. 5 and 14].

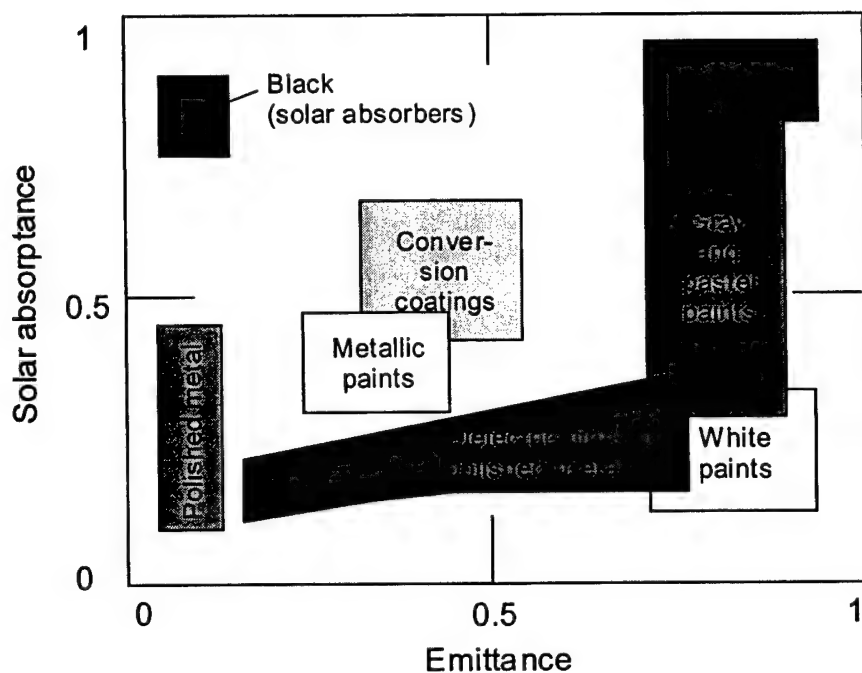


Figure 4. Surface properties by type of finish.

An important fact to consider is the degradation of thermal finishes over their lifetime. The effect of degradation is usually an increase in solar absorptivity with little or no effect on IR emittance. Reasons for this effect are [Ref. 5]:

- Contamination
- Ultraviolet radiation
- Atomic oxygen
- Charged particles
- Micrometeoroids and debris

In most cases contamination is the major contributor to optical surface degradation. Two sources for contamination exist. Particles occur usually during launch from rocket boosters, stage separation or simply already existing particles that circulate as a result of turbulences. Compound outgassing from materials like plastic films, adhesives, foams, and paints. In addition to UV radiation on Earth, "vacuum UV" is

present in space. Its wavelengths are shorter and its effects are more damaging. This UV portion varies strongly over an orbit compared to near UV, which is almost constant. For low Earth orbits, atomic oxygen is another severe cause of erosion. It damages hydrocarbon-type materials. The concentration of atomic oxygen varies inversely with altitude from 100 km to 1000 km. [Ref. 5] The choice of thermal control hardware has to take degradation into account. This is also the reason why only flight-proven coatings should be used. A detailed description of causes for degradation can be obtained from Ref. 5. It also provides lists of flight-proven materials.

Very common thermal design elements are *insulations*, divided into multilayer insulations (MLI) and single-layer radiation barriers. MLI consist of multiple layers of low-emittance films. In space heat transfer through MLIs is a combination of radiation and solid conduction, which are both minimized. MLI blankets prevent excessive heat loss from a component as well as excessive heating from the environment. Single-layer radiation barriers are cheaper and lighter. Therefore they are used where not such strong thermal insulation is required. Besides the original purpose blankets are also used as a shield against atomic oxygen, charged particles and contamination particles.

A *heat switch* is a device that is used in a heat-conduction path and can change its thermal conductance between a good insulator and a good conductor. This is mostly achieved in a passive way, but can also be due to controller signals. The conductance of a passive heat switch depends on temperature with a set point given during manufacturing. Rather than just opening or closing a heat path, heat switches are able to vary the heat conduction. Installed between a heat producing component and a heat sink, the conductance changes can control the temperature of the component. For example waste heat can be conducted to a sink until temperature falls under the set point. Then conduction decreases and heat is kept in the envelope to stabilize the temperature. The practical development of heat switches is fairly new. A common material base is paraffin.

Phase-change materials are also used to stabilize temperatures. It is attached between a component and its mounting surface. During heating of a component this heat is absorbed via phase change and can be removed via radiators during "off" portion of the duty cycle. PCM devices are heat-storage units that use PCMs to greatly increase the

effective “thermal capacitance” of a device. Four phase-change transformations are usable:

- Solid-liquid (melting and freezing)
- Liquid-to-gas (vaporization)
- Solid-to-gas (sublimation)
- Anhydrous salt transformations

Vaporization and sublimation are not of practical use, because they require large volumes. An often-used material is water. Others are inorganic salt hydrates, organic compounds, like paraffin, natural inorganic elements, like sulphur, etc.

Heaters are active thermal devices. They require power to operate and therefore influence the power budget of the spacecraft. Ideally, active devices are not needed, but are sometimes necessary when components are driven to undesired temperatures, that passive components cannot deal with. Heaters are commonly known for three applications [Ref. 5]:

- Provide heat, when electronic devices are off or during cold-case environment
- Provide precise temperature control using thermostats
- Warm up components prior to turning them on

Almost all heaters allow some control over their operation. The simplest way is a relay, controlled from the ground. This is only useful, if the heater is only used for special events or is turned on all the time. A self-controlling device is a mechanical thermostat. For reliability reasons and extended lifetime, they are increasingly replaced by solid-state controllers. A very common type of heater is the patch heater, which can be provided with or without redundancy. Another type of heater is the cartridge heater. This is used to heat material blocks or high-temperature devices. Information about the construction of heaters can be found in Ref. 5.

For a three-axis stabilized satellite the typical approach to achieve thermal control is covering its outside with Multilayer Insulations (MLI) and providing radiator areas

with low solar absorptivity and IR emittance. This is done to reject waste heat because as mentioned earlier the typical behavior is that a spacecraft is getting too hot. This is illustrated in Fig. 5 [Ref. 5]. NPSAT1 is not a typical satellite from this point of view, because as it was already shown in the preliminary analysis, the concern is, that the spacecraft is getting too cold on orbit. But the general usage of thermal control hardware can be seen in Fig. 5.

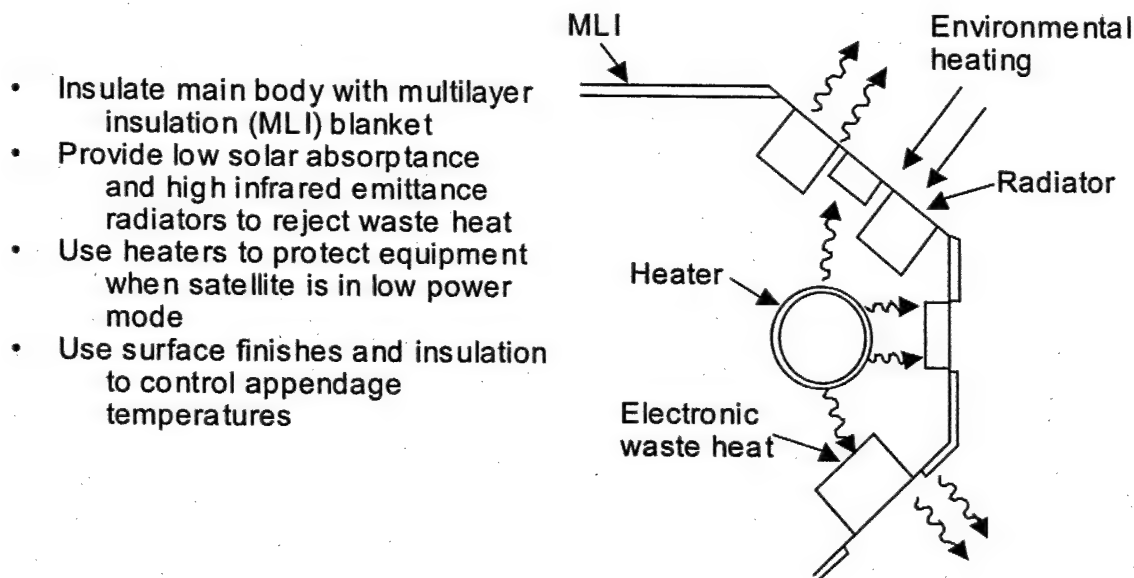


Figure 5. Three-axis satellite thermal control

E. BOLTED-JOINT INTERFACES

The thermal conductance through bolted interfaces is an important topic for thermal control in space. They represent the largest heat path between a unit and its mounting place. For a better understanding, at first the conductance between surfaces under uniform pressure is discussed. Afterwards it is dealt with the bolted-joint problem, which represents surfaces under non-uniform pressure.

Since convection is absent in space (chapter III.A) conduction becomes much more important for heat transfer than on Earth. "Unfortunately, no universal model exists

that can enable one to predict the joint resistance between any two surfaces.” [Ref. 5, p. 599] Different analytical models exist for surfaces under uniform pressure that are validated by lab tests. An appropriate one can be chosen by a close look at the surface conditions of the joint, which is to be analyzed. As Ref. 5 points out, choosing approximate contact resistance values that have been used successfully in past design efforts can be an appropriate way, if parameters required in the contact resistance models are unknown.

Every manufactured material shows imperfections and deviations from its idealized surface geometry. They can be divided into two groups. Macroscopic deviations are called waviness. They can be the result of heat, vibration or gaps in the machining equipment. Microscopic deviations are called roughness. They are due to tool shape, machining process, etc.

Because of this phenomenon, conduction only takes place through the peaks that are in contact (Fig. 6) [Ref.5]. This is only a small fraction of the whole surface (less than 2 %). Distribution of contact points depends on combination of waviness and roughness. Applying a pressure to the two surfaces in contact, the pressure at the asperities in contact is much higher than the apparent pressure. This leads to elastic deformation or, if the yield strength is exceeded, to plastic deformation.

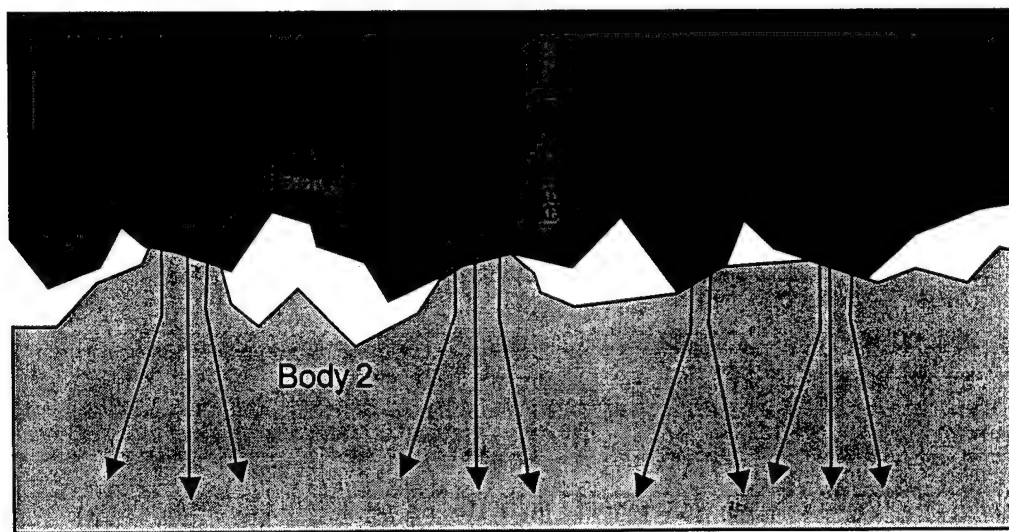


Figure 6. Heat conductance through contact points.

The parts of a surface without direct contact exchange heat via radiation. Contact-conductance is [Ref. 5]:

$$C_j = \frac{q''}{\Delta T_j} \cdot A = h_j \cdot A = (h_c + h_r + h_g) \cdot A \quad (\text{III.11})$$

This means that the contact-conductance is proportional to the ratio between the heat flux (equation III.1) and inverse proportional to the temperature drop over the interface. The conductance through the joint consists of three conductances in series: the conduction through the contacting points, the radiation through the gaps between the surfaces, and the gas conduction through the gap filling gas. "For most space applications, surface contact is in a vacuum environment, and the amount of gas present in the gaps is negligible and so is the conductive heat transfer through the gaps." [Ref. 5, p. 601/602]

For the mentioned elastic and plastic deformations Mikic has developed equations for heat-transfer coefficients, depending on the surface properties slope (m), root-mean-square roughness (σ), pressure (p), and the effective modulus of elasticity (E'), respectively microhardness (H) [Ref. 5]:

$$h_e = 1.55 \cdot \frac{k_h \cdot m}{\sigma} \cdot \left(\sqrt{2} \cdot \frac{p}{E' \cdot m} \right)^{0.94} \quad (\text{III.12})$$

$$h_p = 1.13 \cdot \frac{k_h \cdot m}{\sigma} \cdot \left(\frac{p}{H_c} \right)^{0.94} \quad (\text{III.13})$$

Bolted joints are a more difficult form of surface contacts, because the pressure is non-uniform. For reliability reasons of the unit the temperature rise across this interface should be small. Components are commonly mounted to the spacecraft structure by bolt patterns using flanges along the baseplate perimeter. For the contact region Ref. 5 provides the heat-transfer coefficient:

$$h_c = 1.45 \cdot \frac{k \cdot m}{\sigma} \cdot \left(\frac{p(r)}{H_c} \right)^{0.985} \quad (\text{III.14})$$

This is similar to equation (III.13) for plastic deformation. Pressure depends on the radius (r) of the contact region. No simple representation for the size of this contact region is available. In engineering practice, $r_c = 1.5 \cdot D_s$ is used frequently, where D_s is the diameter of the screw. [Ref. 5] Besides this theoretical treatment, which is not particularly practical, other correlations exist, developed from vacuum tests. They can be used for the typical stainless-steel bolt, aluminum plate configuration.

Bratkovich [Ref. 4]:

$$C_b = 6.3 \cdot \left(\frac{\tau_{\max} \cdot e_{al} \cdot T_{pl}}{Y \cdot l_f \cdot l_{pl,m}} \right)^{0.511} \cdot k_{al} \cdot l_{pl,m} \quad (\text{III.15})$$

Instead of roughness, this equation uses finish thickness (l_f). The coefficient of expansion (e) and l_f lack the multiplier 10^{-6} . Guidelines for the use of this equation are provided in Ref. 4.

Gluck (dimensional) [Ref. 5]:

$$C_b = 503 \cdot [\tau_i \cdot (e_{al} - e_{ss}) \cdot (T_{pl} - 200)]^{0.775} \quad (\text{III.16})$$

This equation simply uses a corrected torque for calculation of thermal conductance. The installation torque depends on the screw-type used.

Gluck [Ref. 5 and Ref. 6]:

$$C_b = 433 \cdot \left[\frac{\tau_i \cdot (e_{al} - e_{ss}) \cdot (T_{pl} - 200)}{E^1 \cdot \sigma^{2.5} \cdot D_s^{0.5}} \right]^{0.652} \cdot k_h \cdot \sigma \quad (\text{III.17})$$

This is the dimensionless form of equation (III.16) and takes more material parameters into account. This equations differs from the one in Ref. 5 from which it is obtained, because the equation in the reference contains a typo. When questioned the author of that chapter provided the corrected version, shown in App. B [Ref 6].

IV. NPSAT1 THERMAL ANALYSIS BACKGROUND

A. CONSTRAINTS AND REQUIREMENTS

This chapter deals with the constraints and requirements influencing the thermal design. They provide a basis for the simulation work. In the space environment only micro-gravity is present. Therefore convection does not apply, which reduces the available heat-transfer modes (chapter III.A). LEO is the orbit type with the highest content of atomic oxygen, which leads to degradation of surface finishes (see chapter III.D).

Because of low altitude, this orbit provides a relatively high amount of heat load from albedo and Earth IR. Fig. 7 [Ref. 17] shows the β -angle (angle between sun vector and orbital plane) of NPSAT1's orbit over a year. The β -angle, along with the orbit altitude, defines the time the satellite spends in sunlight and in eclipse. This has a strong influence on the thermal conditions, because it determines the amount and the kind of heat to which NPSAT1 is exposed. Solar and albedo heating increase with higher β -angles, whereas Earth IR is constant. [Ref. 5] For NPSAT1 energy absorbed by the solar cells covering the perimeter of NPSAT1 can be obtained from the β -angle histogram in App. C. Over a year of on-orbit operation, the beta-angle is generally about 0 ° with a maximum absolute value of 60 °, as shown in Fig. 7.

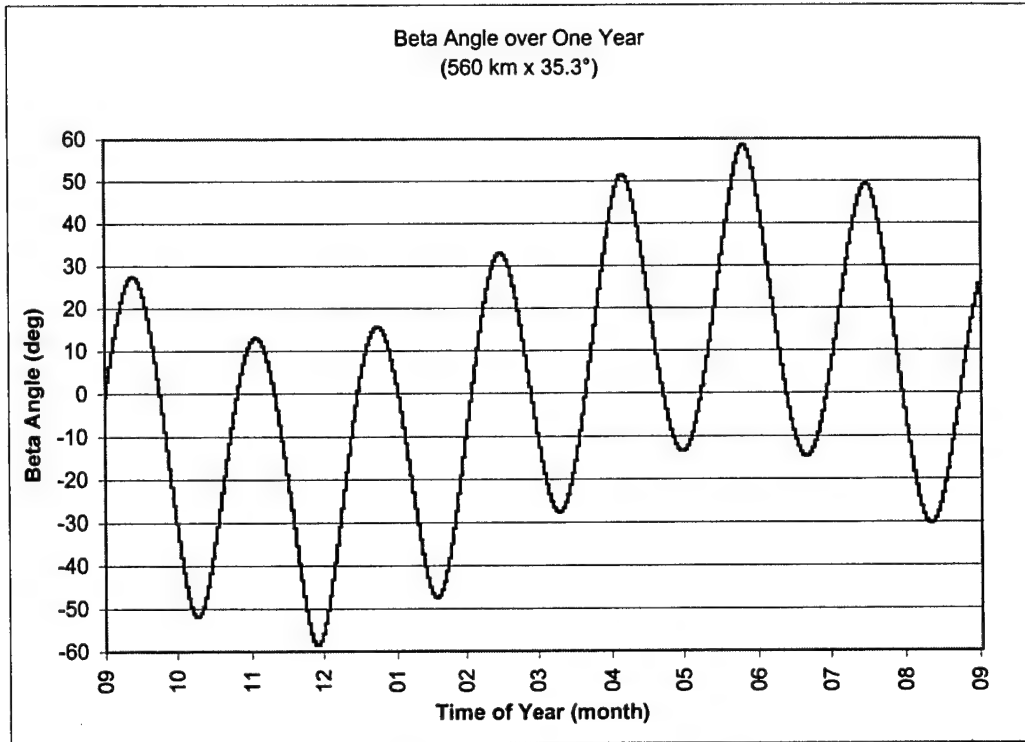


Figure 7. Beta angles for NPSAT1 orbit.

The two extreme cases, beta-angle 0° and 60° , are shown in Fig. 8. The different direction of the solar vector is due to the fact, that lowest orbital heating, which is used for the 0° cold case scenario, appears at June solstice and the highest orbital heating, which is used for the 60° hot case appears at December solstice. It can be seen, that the position of NPSAT1's orbit to the solar vector (yellow line) not only defines the time the spacecraft spends in eclipse (shadow cone in Fig. 8) during an orbit, but also determines the sides, which are exposed to direct solar heating. For the 0° beta-angle the top and the front and aft sides in direction of the velocity vector (x-coordinate in Fig. 1) face the most solar heating. In contrast, for a beta-angle of 60° , only one side of the orbital normal vector direction (+ or - y-coordinate in Fig. 1) faces most of the solar heating. The assigned heating of NPSAT1 can be found in Fig. 18.

The variation over time of the orbit portion spent in eclipse and sunlight as a function of the beta-angle obtained from I-DEAS is shown in Tab. 2.

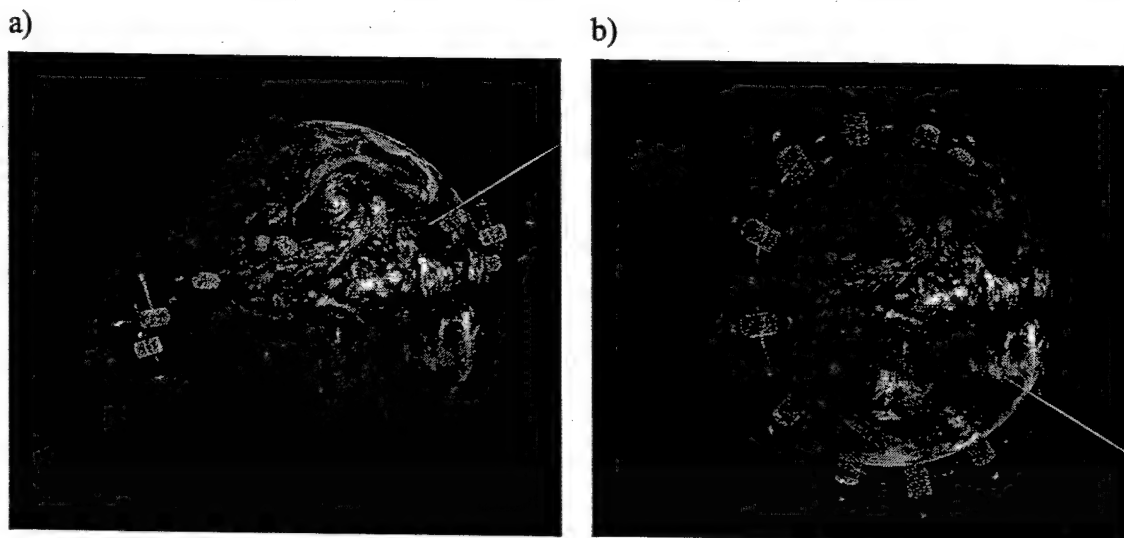


Figure 8. NPSAT1 orbits: a) beta angle 0 °, b) beta angle + 60 °.

<i>Parameter</i>	<i>Cold case</i>	<i>Hot case</i>
β -angle	0 °	± 60 °
Orbit duration	1.5975 hr	
Sunlight per orbit	1.0042 hr	1.2595 hr
Eclipse per orbit	0.5933 hr	0.338 hr

Table 2. Orbital time parameters.

The requirement to use three-axis stabilization is based on the need of the experiments VISIM, Langmuir probe, and CERTO. NPSAT1 is stabilized such that the bottom of the cylinder, which contains the camera, is always nadir facing and the Langmuir boom and CERTO antennas point in the orbit normal opposing direction (Fig. 1). This effects the energy exchange with space (solar heating) and therefore influences the thermal design. Because one side is always nadir facing, this side collects much more Earth IR than the other sides. Solar heating is much more intense on the sides in velocity vector direction than on the sides normal to the vector direction. This was already shown in the preliminary analysis (App. A).

"Controlling temperatures is only one facet in the building of a satellite and, as such, it cannot have a consuming impact on overall design, cost, or schedule. As it

happens, much of thermal engineering involves negotiating acceptable interactions with other satellite subsystems.” (Ref. 9, p. 7) The thermal interface considerations include:

- Temperatures
- Power budget
- Weight budget
- Material requirements
- Limited sizes

<i>Component</i>	<i>NPSAT1 (operating)</i>			<i>Operating temp. from references</i>		<i>Survival temp. from references</i>	
	<i>lowest T. (°C)</i>	<i>highest T. (°C)</i>	<i>average power (W)</i>	<i>lowest T. (°C)</i>	<i>highest T. (°C)</i>	<i>lowest T. (°C)</i>	<i>highest T. (°C)</i>
EPS	-25	60	1.313	0	40	-20	70
ACS	-25	60	0.75	0	40	-20	70
C&DH/CPE	-25	60	1.846	0	50	-20	70
Magnetometer	-25	60	0.7	-40	85	-55	125
SMS	-25	60	0.13	0	50	-20	70
MEMS	-25	60	0.12	0	40	-20	70
Battery	15	30	0.042	10	20	0	35
Torque Rods	-25	60	0.015	0	50	-20	70
VISIM Contr.	-25	60	0.317	0	50	-20	70
VISIM Cam.	0	60	0.009	-35	65	-40	100
Langmuir	-25	60	0.424	0	35	n/a	n/a
CERTO	-25	60	2.298	0	35	n/a	n/a
RF-Switch	-25	60	0.04	0	50	-20	70
Solar Cells	-25	60	n/a	-100	85	-100	125

Table 3. Orbital temperatures and power requirements.

The specifications for orbital temperature ranges are provided in Tab. 3. The temperature ranges from references are a combination of the narrowest temperature

ranges obtained from references 5, 9, 11, and 14. NPSAT1 temperature range is the range used for development of NPSAT1 [Ref. 18].

The power budget is defined so far by the effectiveness of the solar cells (chapter II.C.1) and the battery, as well as the duty cycles and power consumption of the components. These duty cycles are explained in further detail in chapter V.D.2. The power budget can be obtained from App. D. Also Tab. 3 provides the average power requirements of the components. Differences to the values in the power budget occur because Tab. 3 is calculated based on the duty cycles in Tab. 7. The limitations in power demand the use of passive components, where possible. If active components are necessary, their operation must not exceed the power budget.

Material requirements deal mostly with their application in the space environment. This means having a minimum of degradation (chapter III.D) over the mission life and meeting low-outgassing requirements to prevent contamination. Flight-proven material is a good choice, because no additional testing is required. Also, with these materials, changes between beginning-of-life (BOL) and end-of-life (EOL) have to be considered. Property changes over the lifetime could lead to the use of compensational hardware, for instance heaters. Also, stable coating properties allow for better temperature predictions over the mission life.

The weight budget is not a very critical value in the NPSAT1 design. But since not all of the components are entirely designed by now, additional weight by adding components to the design should be avoided. Concerning size, every component has to fit into the overall dimensions of NPSAT1 (Ref. 17). Additional thermal hardware could lead to redesign and should be avoided. Heat pipes, for example, are not considered because of the potential changes in the overall configuration and design that would be incurred.

The Aerospace Corporation suggested an analysis showing that the power inputs, boundary conditions, and model assumptions are conservative. [Ref. 22] The use of gold anodized coatings for external facing sides was questioned as appropriate for thermal control since the optical properties vary widely, subject to processing and also degrade on orbit. Aerospace Corporation also suggested specific environmental heating

specifications and hot and cold case scenarios [Ref. 22 and 23]. Results can be found in chapter VII.C. A concern was raised with the thermal control of the batteries, because of their special operating temperatures requirements (Tab. 3).

Besides the flight and operational regime in space, there are other thermal regimes, like the transportation of the payload to the launch vehicle integration site as well as launch and separation from the launch vehicle on orbit. An analysis of these regimes is not part of this thesis; however, the issues posed by these other regimes are being addressed as appropriate.

B. SOFTWARE AND ANALYTICAL BASICS

A finite element (FE) calculation consists of three steps according to Ref. 10:

- Preprocessor: building a sufficiently detailed model of the physical and technical problem.
- Solver: solving the mathematical model of the structure.
- Postprocessor: output of the calculated stresses, temperatures, heat flows, etc.

1. The CAE-Software

A CAE-system is used to develop a software model, and performing the thermal analysis. For this work a geometric model was given, which was a little bit adjusted. Then all the thermal properties were applied. All three FE-steps were done with EDS I-DEAS. This is an integrated CAD/CAM/FEM solution for construction of machines, plants, and vehicles. It supports concurrent engineering through built-in team-data-management. The geometry of the product is provided as a volume model for all tasks. I-DEAS contains six applications for design, drafting, simulation (FEM), test, manufacturing (NC), and management. Each application consists of a variety of tools. Also, third-party tools are included just as Thermal Model Generation (TMG) and Thermal Model Validation (TMV) from Maya. Exchanging data between the different

I-DEAS applications and tools is very simple, because all tools use the same formats. The whole work was done in the I-DEAS Simulation application. The given model was enhanced in the model manager task. The meshing task was used to mesh the geometry and for adding physical and material properties. The setup of the simulation runs and the simulation itself was done using TMG. Which data is written to files by I-DEAS during solve can be chosen. For post-processing the data of interest was extracted from these files. Therefore, scripts were written in the script-programming language Python. The advantage of a script language is the simple code. With these scripts, input files for a spreadsheet program were written, allowing visualization of the data.

2. The Analytical Method

The finite element method is a procedure, which describes complex structures numerically. This is done by dividing the structure into a grid of small (finite) elements. The elements are of a simple shape, like a square or a triangle, and consist of edges and nodes. This information is written in matrix form. By synthesizing all elements, the behavior of the complete structure can be predicted. The program assembles all matrices into a global matrix. Boundary conditions and modeling operations are performed on the nodes of each element. TMG uses the finite difference method (FDM), which means that difference quotients are introduced with regard to the elements. The differential equations are solved. Therefore boundary conditions and modeling operations are performed on elements. The nodes only describe the geometry, but do not become part of the numerical thermal model. Besides the following description, further detailed explanations on how FDM works for thermal analysis can be obtained from Ref. 13.

There are two solution methods available in I-DEAS TMG for solving the conductance matrix. The *Conjugate Gradient* solver uses a biconjugate Gradient method with a Newton Raphson scheme for non-linear terms. This solver can be controlled by some parameters. The iteration steps are limited by a maximum number of iterations per time step. If this limit is exceeded, the solution passes on to the next time step. The Convergence Criterion defines when convergence is achieved. The size of the preconditioning matrix can be controlled by the Preconditioning Matrix Fill Value. If the

solution does not converge within the limited number of steps, TMG increases the Fill Value automatically and tries to solve the step again. This may lead to a large and therefore slow system. In this case the Convergence Criterion can be increased. The *Jacobi* method is an iterative solver that uses successive substitution. It computes successive element temperatures by balancing heat flows. Two parameters control this solver. The Convergence Accelerator tries to extrapolate the solution from the change of temperatures over successive iterations. The Quartic Solver directly solves radiation conductances at each iteration instead of a linear solve with an update at every iteration.

Conduction can be modeled with two different methods in TMG. In the *Element Center of Gravity* method the elements are represented by their center of gravity along with a calculation point in the middle of every boundary (face or edge). Conductances are established from each boundary calculation point to both the centroidal node and the remaining boundary calculation points, Fig. 9. [Ref. 21] The algorithm for this constrains a piecewise-linear element temperature function to satisfy the governing partial differential equation for conduction. Heat flow between this element and other elements only takes place via the centroidal node. The centroidal node is used to compute distributed heat transfer. The heat flow into the centroidal node is distributed to the boundary calculation points. TMG interpolates the temperature results from the calculation points to the element nodes for post processing and the center of gravity temperature is kept as the element temperature. The *Element Center* Method uses only one calculation point. It is established at the intersection of an element edge (or face) normals.

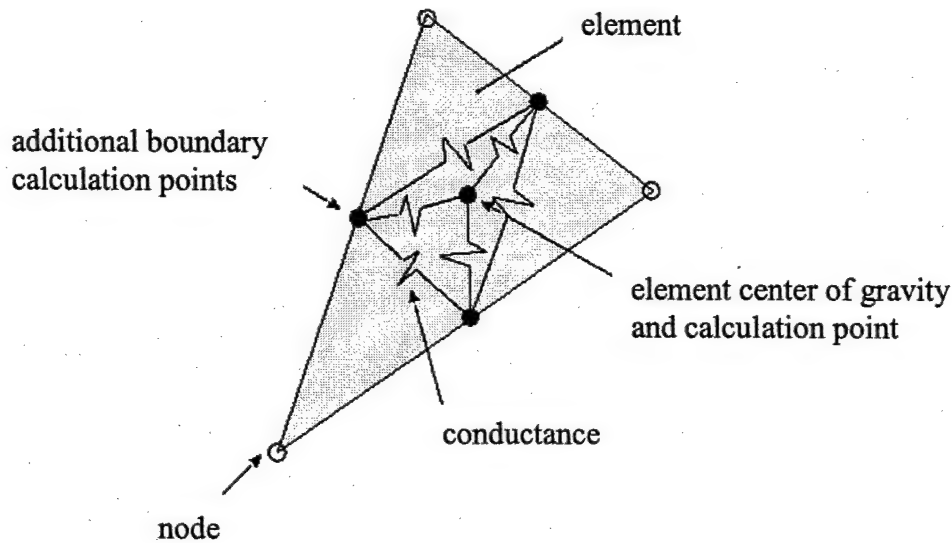


Figure 9. Calculation points in the Element Center of Gravity method.

Transient FEM and FDM problems can generally be solved implicitly and explicitly. With an implicit solver all element temperatures must be solved iteratively at every time step. Such a solver is implemented in TMG as the backward solution method. It is a differencing scheme, where the element heat balance equations are evaluated at the end of the integration time step. This solver is default and recommended by Ref. 21, because it is more reliable than the explicit solver.

C. ANALYSIS PROCEDURE

This chapter provides an overview of the methodology of the simulation. A detailed description of every single simulation, including all parameters and results can be found in chapter VII.

The thermal design process is a combination of design selection and supporting analysis. As described in chapter II, thermal design was widely chosen. Its efficiency is now subject to analysis. Based on the results, either the chosen design is verified or a redesign becomes necessary. The procedure for a typical thermal analysis is shown in the flowchart in Fig. 10 [Ref. 21]:

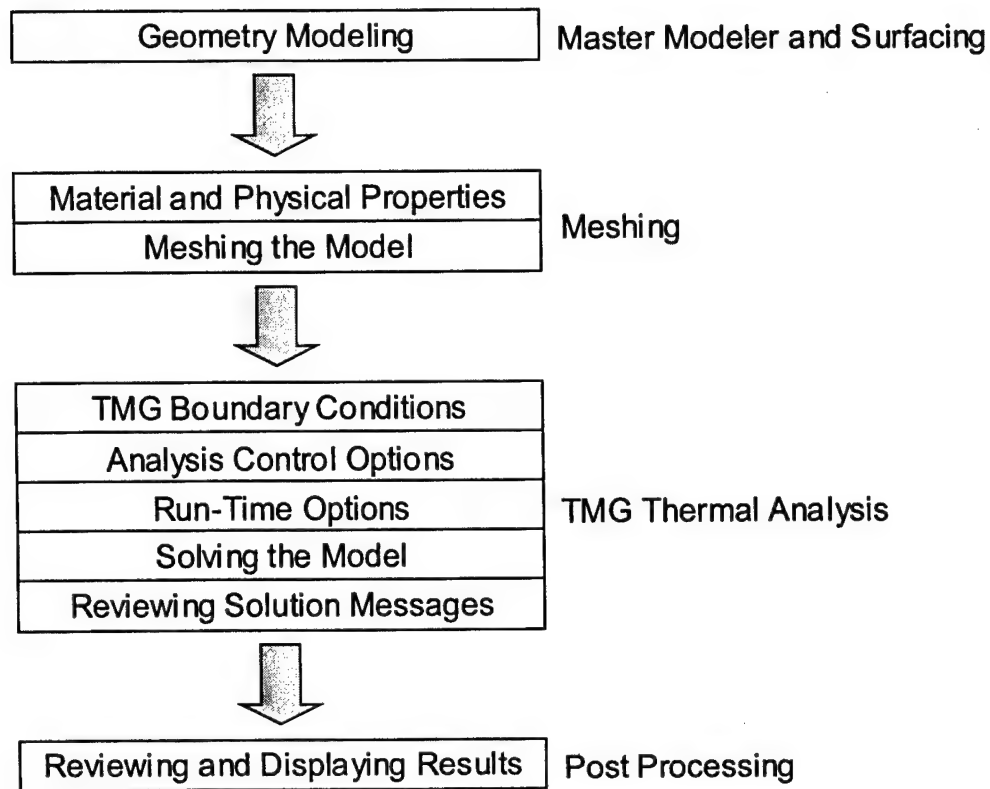


Figure 10. Thermal modeling and analyzing process.

The overall process of discovering an appropriate design approach and its verification is an iterative process, which repeats most of the steps presented in Fig. 10 a number of times. "In general, many parametric analysis cases with a small model are of greater value to a concept study than are detailed analyses with large models. Scaling existing designs from other programs can also be an efficient way of answering study needs ..." [Ref. 5, p. 525] From considerations presented in chapter IV.A, worst cases for hot and cold scenarios were derived and to keep the model to a manageable size, simplifications had to be made (chapter V). Oppenheim was used as calculation method for radiation coupling, for it is proven to be more efficient than Gebhardt, because the matrices are smaller. (Chapter III.A) As solution method the default Conjugate Gradient solver was used, because it is much faster than Jacobi, especially for ill-conditioned problems. The chosen conduction method is Element Center of Gravity, because it is

more accurate than the simple Element Center method. It is also the I-DEAS default setting.

The overall process is to use a normal orbit for iterations until a satisfying design is reached. Hot and cold cases will then be evaluated under all necessary viewpoints. Effects on the power budget are calculated.

Before a transient simulation was started a steady-state run was performed. This means, the model is solved only for a specific point in time. In this run all heat loads and all environmental heating were not chosen from a specific time. Instead the software calculated time averages. If there are thermostats in the model, they are not considered in this type of simulation run. The output temperatures, stored in a file, can then be used as initial conditions for the transient run. Alternatively it can be started with a specific temperature, that can be defined, or without any initial conditions. Then 0 (in the units of the model) is the overall starting temperature. Using the steady-state results as initial temperatures shortens the transient phenomenon, which falsifies the results at the beginning of the transient run. After every change in the model a new file with initial conditions is needed.

Setting up a transient run includes setting the integration control (Chapter IV.B.2), the time period for the simulation, the time for results output and the initial conditions. For integration control the recommended backward solver is used. The decision was made to run a simulation usually over 24 hours, since orbital influences change over a day. The time for results output was decided to be initially 120 seconds, later changed to 240 seconds (chapter VII.B.2). As initial conditions the already mentioned results file from a steady-state analysis is chosen. For a subsequent simulation, parts of the solution can be reused, depending on the changes that are made to the model. For example, the view factors do not have to be calculated again, if the optical properties were not changed. This is specified in the "Restart Options".

The materials considered for the analysis are primarily surface finishes. But with surface finishes it has also to be considered, that only well tested, or even flight-proven materials should be used, ideally some that are also easy to handle and cheap. Insulation is taken into account, since they could be attached to the design easily. As can be seen

from the preliminary analysis, NPSAT1 tends to get too cold instead of too hot during an orbit. Therefore all radiating devices are of no use. Also, temperature-stabilizing devices might not be of great use either. To raise temperatures, heaters are appropriate devices. This analysis will provide a design evaluation and power requirements.

V. NPSAT1 THERMAL MODEL

A. STRUCTURAL MODEL

A structural model was provided as mentioned in chapter II.B. This model was slightly adjusted to function as a basis for the thermal modeling. A FEM for structural analysis is more accurate the more it looks like the real item. Concerning thermal modeling this is true for radiation. The calculation of radiation depends mostly on the way elements view and shadow each other (Chapter III.A) and, therefore, a realistically looking model represents the real situation best. For other thermal features this is not that much important. Many thermal features, like conductances, cannot even be seen in the model.

Two small changes were made to the structural model to achieve greater accuracy for radiation modeling. The patch antennas and the hole in the nadir facing antenna ground plate were added. On one hand the antennas shadow a little part of the antenna ground plates and therefore might influence their temperatures. On the other hand the patch antennas have to be part of the model, because their temperature itself is of interest. This is because they are not covered with paint, like the space-facing structural elements of NPSAT1, and they are heavily insulated from the rest of the spacecraft. A picture of the configuration in a design model can be seen in Fig. 11. The VISIM camera, located on the first deck, is looking through the hole in the nadir facing antenna ground plate.

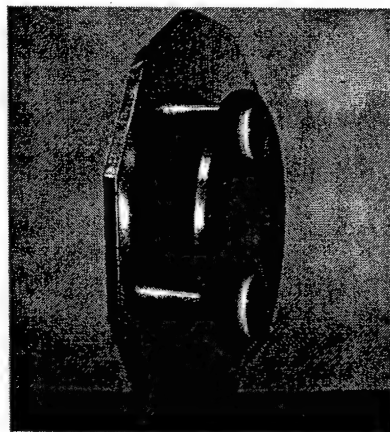


Figure 11. Patch antennas and ground plate configuration.

The dimensions of the large patch antennas can be obtained from App E [Ref. 17]. Their location and alignment can be estimated in Fig. 1 and Fig. 11. This is not yet finally defined. They were placed in line with the velocity vector, the small antenna in +x direction. Using the “sketch in place” option two “ellipses by center” with arbitrary dimensions were created on each antenna ground plate. Then the dimensions were adjusted, using the “modify entity” option. Finally, this ellipse was extruded in the zenith-facing direction about the thickness of the patch antenna and dielectric ellipse using the “add” option not to combine the patch antenna and ground plate to one entity.

A “Center Edge” circle was created on the nadir-facing antenna ground plate, using the “sketch in place” option, for the hole. After adjusting the dimension, the circle was extruded through the plate using the “cut” option.

B. MESHING

I-DEAS offers automatic meshing. This means that it uses geometry entities from the structural model for mesh creation. Three different families of meshes are available:

- 1 D: beam elements for part edges
- 2 D: thin-shell elements for part surfaces
- 3 D: Axisymmetric solid elements for part volumes

For the thermal model of NPSAT1 no solid meshes were used, although all structures are volumes. Except for the three longerons, all entities were meshed using thin-shell elements. Thin-shell elements have fewer nodes than solid elements and, therefore, shorten computation time. Also solid elements are only necessary, if the temperature distribution within a meshed material is of interest. This is not the case for NPSAT1. The thin-shell elements are assigned a material and a physical property, making their thermal behavior more accurate. The longerons are modeled using beam elements and need the definition of a cross section.

Every mesh can be generated by two different methods: mapped and free meshing. Mapped meshes require the same number of elements on opposite sides and an area that is bounded by three or four edges. Free meshing allows more flexibility in defining mesh areas. An algorithm tries to minimize element distortion, which means the deviation from the perfect shape, which is chosen for the mesh. Also holes in the mesh area are no problem for a free mesh.

For thin-shell elements, four different element types are available: Triangles and quadrilaterals, each linear (two nodes along each side) or parabolic (three nodes along each side). Since the nodes are not important for thermal analysis (Chapter IV.B.2) only the linear elements were considered. For the deck, antenna ground plate, and patch antenna meshes, triangular elements were chosen, because they are more uniformly distributed in a round boundary than quadrilateral elements. This uniform distribution was especially important at the perimeter of the plates to connect them with the structural panels. All other surfaces were meshed using quadrilateral elements, because they fit rectangular boundaries best.

Because the satellite decks are not of a simple shape, the free mesh option was chosen for the meshes. A free mesh needs two parameters that control the mesh generation. The element length is the size for an element the program attempts to achieve. The absolute deviation controls the mesh refinement on curves, which means the deviation between straight element sides and curved boundaries. The element length for the decks was chosen depending on the distance between the mounting bolts of the component envelopes. The intention was to avoid two mounting bolts on one element. Since a mounting bolt equals a thermal coupling (contact conductance) this could lead to inaccuracies [Ref. 21]. Therefore the component with the smallest distance between its mounting bolts on each deck had to be identified. (App. F). Another requirement was, that each of the twelve sides should have three elements, because they are necessary to model the thermal couplings via bolts later on. This was automatically achieved with the element sizes used. Since the elements are ideally equilateral triangles and the calculation point is the center of gravity, the element lengths had to be calculated to achieve the desired distance between two neighboring centers of gravity. For the equilateral triangle in Fig 12

$$x = a \cdot \frac{\sqrt{3}}{6}. \quad (V.1)$$

Therefore, the distance between two neighboring centers of gravity is double this value. In conclusion, the element length can be calculated from

$$a = d \cdot \frac{3}{\sqrt{3}} \quad (V.2)$$

where d is the desired distance. [Ref. 20]

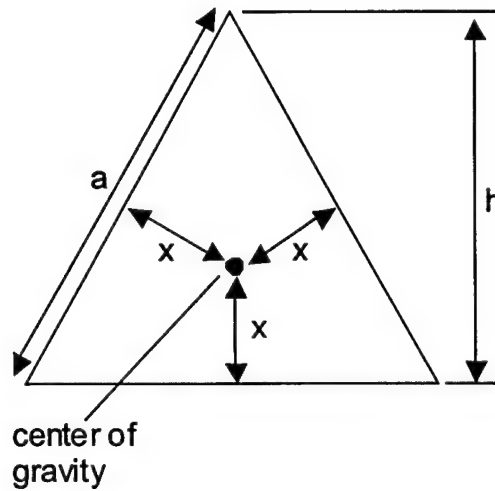


Figure 12. Relations in an equilateral triangle.

The antenna ground plates were meshed using free mesh, because round entities cannot be meshed with mapped meshing. The antenna ground plates have connections to first and fourth deck respectively and, the patch antennas are attached to them. There are eight washers between each antenna ground plate and the deck. These are not structurally modeled, but only a contact conductance was defined (Chapter V.E). Each patch antenna has one connection, which is considered for the thermal model. The other connection that can be seen in the drawing (App. E) is an electrical connection that is thermally highly insulated. The mesh of the antenna ground plate was rather unrestricted, because the distance between all connections is large compared to the mesh size of the decks. To generate a mesh in the same order of magnitude as the decks, 5 cm was chosen as element length.

The patch antenna mesh was also generated using free meshing, for the same reasons as the deck meshes. The patch antenna mesh generation was also not restricted by any connections, since there is only one as mentioned earlier. To generate more than only one element per antenna, the element length was chosen to be 3 cm. Table 4 summarizes all generated meshes with its parameters.

<u>Entity</u>	<u>Element length</u>
First deck	4 cm
Second deck	4.5 cm
Third deck	5 cm
Fourth deck	5 cm
Antenna ground plates	5 cm
Patch antennas	3 cm

Table 4. Deck mesh parameters for free meshing.

The mesh of the structural panel was also done in accordance with the bolt pattern. Each of the twelve sides of the lower deck is connected to each deck with three bolts. Also, each panel (consisting of four sides, see Fig 1) is bolted to the longerons using six bolts. Hence, the height of a solar panel approximately equals three elements. Therefore, each side of the lower structural panels should consist of 3 x 6 elements. The upper structural panel carries solar cells with the same dimensions as the lowest solar cell band. For the mesh, the little band on top of the upper panel without solar cells was neglected. The large band without solar cells on the bottom of the upper panel without solar cells was represented by one element as far as height is concerned, because it is almost a third of the solar panel. Therefore, each side of the upper structural panel should consist of 3 x 4 elements. The meshes were generated using mapped meshing, because it is possible to key in a number of elements per side of a mesh directly.

The Lightband in the given geometry model is just a big ring. This represents more the overall dimensions, than the real geometry. The satellite carries only one part of the Lightband when on orbit, because after separation from the launch vehicle, the other

part stays on the launch vehicle. To simplify the model, the Lightband was meshed with one band of elements around its outside perimeter. The height of these elements equals half of the complete Lightband height. This was done using mapped meshing. The number of elements was chosen by considering the mounting of the Lightband [Ref. 17].

The longerons are typical entities for beam meshes. The distribution of heat in the longerons is not of interest. They also do not play a significant role concerning radiation because of their small surface compared to all other parts. Therefore, a more detailed mesh is not necessary. At first a beam cross section had to be drawn. This is shown in Fig. 13. The dimensions were measured in the I-DEAS model. Then a beam mesh, using this cross section, was generated around one of the edges of each longeron in the geometry model. As a result, the beam mesh is not exactly located where the longeron is, but this is not important, since all connections with the longeron are thermal couplings, for which the position of the entities is not important (Chapter V.A).

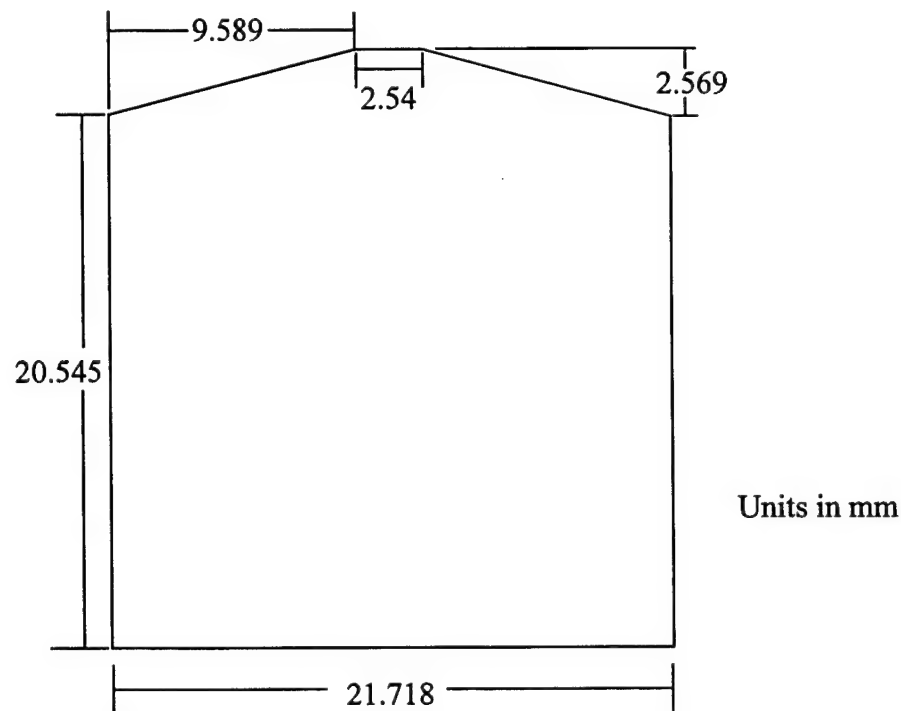


Figure 13. Beam cross section for longeron mesh.

The Solar cells could have been modeled by changing the optical properties of the regions on the structural panel, where solar cells are mounted. But since the solar cells are part of a solar array, which is bolted to the structural panel, the model was made more accurate. Ref. 11 provides a useful process for this modeling. The elements of the structural panel, where solar arrays are mounted, are copied and projected 0.05 mm into space. This number was chosen arbitrarily. Then the material and physical properties were adjusted. Fig. 19 shows the solar cell mesh.

Finally elements that belong to the mesh of one entity were grouped. This is a great advantage for later use and for displaying them. The whole mesh of NPSAT1 can be seen in Fig. 14.

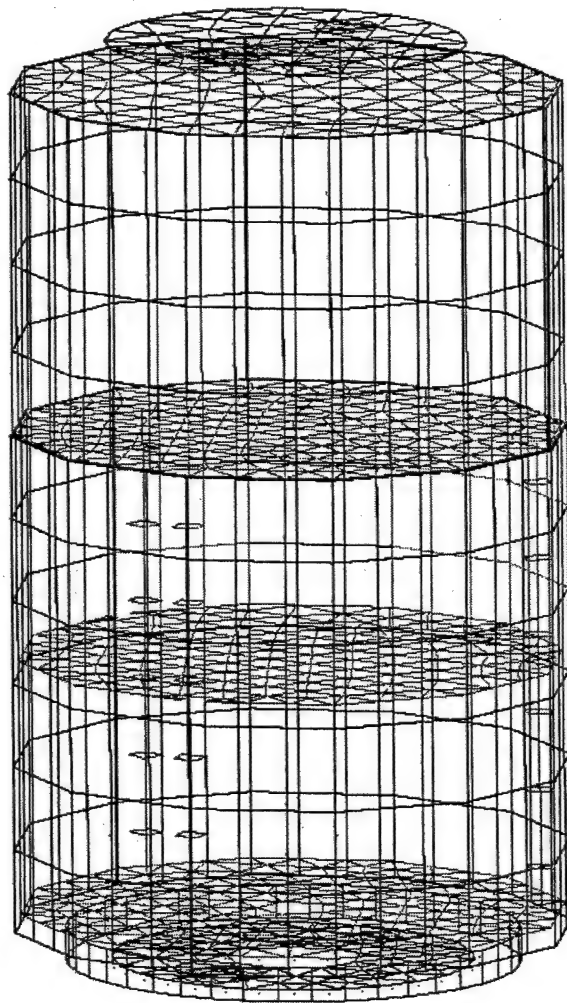


Figure 14. NPSAT1 mesh.

C. MATERIALS AND PHYSICAL PROPERTIES

Material and physical properties have to be assigned to every mesh. This is necessary for TMG to calculate heat flow and temperature distributions, as well as absorbed and emitted radiation. As mentioned in chapter II.B, the construction material for NPSAT1 is aluminum 6061-T6. The patch antennas consist of copper. Both are contained in the TMG solid material database and were imported. Additionally the optical properties for the surface finish had to be defined. The values for gold and black anodized aluminum and copper were obtained from Ref. 5. All values are valid for beginning-of-life. The values for the solar cells were calculated to account for electrical energy generation by the cells. [Ref. 8] The manufacturer provided $\alpha = 0.92$ and $\varepsilon = 0.85$ as optical properties. The effective solar absorptance ($\alpha_{sol,eff}$) depends on the efficiency (η) of the cells. The commercial solar cells have an efficiency of 26.5 % at BOL and 22.3 % at EOL. The experimental cells have an efficiency of 24 %. Equation V.3 is used for the calculation of the effective solar absorptance [Ref. 8]:

$$\overline{\alpha_{sol,eff}} = \overline{\alpha_{sol}} - F_{pg} \cdot \eta \quad (V.3)$$

In this equation F_{pg} is the packing factor, which is the ratio of the total active solar cell area to the total substrate area for which $\overline{\alpha_{sol,eff}}$ is to be determined. Calculations can be obtained from App. G. Results are shown in Tab. 5. The table containing the physical thicknesses can be obtained from App. H.

<i>Material</i>	Gold-anodized AL	Black-anodized AL	Solar Cells, commercial	Solar Cells, experimental	Copper
<i>Absorptivity</i> (α)	0.48	0.65	0.724	0.754	0.3
<i>Emmissivity</i> (ε)	0.82	0.85	0.85	0.85	0.03
<i>Usage</i>	Decks, antenna ground plates, Lightband, longerons	Structural panels	Solar cell arrays	Solar cell arrays	Patch antennas

Table 5. Optical properties of initially used materials for BOL.

D. COMPONENTS

1. Structure

The components and their envelopes were not modeled in detail. This is due to simplification and the design status. Since the components are not entirely designed, too many assumptions would be necessary to build a detailed model. For this work, the components together with envelopes are represented by non-geometric elements. This is simply an element that consists of a thermal capacitance, and can be integrated into the structural model. Since only this one value represents a whole subsystem, its influence was analyzed.

Two approaches were to be tested with a simulation. A very simple and conservative method is to calculate the capacitance based on weight and a representative heat capacity. Since the components are not entirely designed until now, the maximum allowed weight was chosen. The heat capacity was taken from aluminum, because most of the box consists of aluminum.

A second approach was much more detailed. The boxes were assumed to consist of an aluminum envelope, several fiberglass boards, and screws. From envelope dimension and wall thickness, the volume was calculated. For calculation of the volume of the printed circuit boards (PCB), the dimensions of the largest envelope side were taken and multiplied by the thickness of 3 mm. Multiplied by density and specific heat for aluminum and fiberglass, respectively, the capacitance of these components was obtained. From the number of screws per board, their weight, and the specific heat of stainless steel, the capacitance of the screws was calculated. The individual capacitances were summed-up and a margin of 10 % was added. This was done, because the calculation omits all components on the circuit boards, and their specific heat is unknown. The capacitance calculation of the torque rods and the camera was slightly different, because their weight was known. These weights were simply multiplied by the specific heat of aluminum. The calculations for all components and results can be found in App. I.

2. Heat Generation

The waste heat generated by the components is modeled as boundary conditions. These boundary conditions are connected to the non-geometric elements representing the components. The energy lost as heat is assumed to equal the energy a component uses to operate, except for the battery. Therefore the heat loss can be derived from the power budget, which includes the duty-cycles. Two parameters play an important role in the decision how to model the heat generation of a component: the frequency of operation versus simulation time step (Chapter IV.C) and the dependency of the duty cycle on sunlight and eclipse. Components with a shorter period than the simulation time step were considered as high frequency and the boundary condition value was assumed to be constant. This was done, because the comparatively slow measurement of the simulation could not catch all “on” and “off” states. Components with a longer period than the simulation time step were given table driven boundary conditions. Since many duty cycles depend on sunlight and eclipse, the adjustment of orbit and boundary condition values is necessary. All tables were built, assuming an orbit is starting when NPSAT1 entered the sunlight period. This assumption is justified by the fact, that the duty-cycle will not be the same every day based on the position of the satellite with respect to the ground-stations. The adjustment was made in the orbit setting (chapter V.F). Also specific tables for each orbit setup had to be developed, because sunlight and eclipse periods change (Chapter IV.A). The battery is charged during sunlight and discharged during eclipse, when the solar cells collect less energy. The assumption is that the battery only generates waste heat during discharge. This heat generation depends on the efficiency of the battery and the amount of energy, which is required by other components.

For the high-frequency devices the average power requirements were derived from the power budget in App. D. Tab. 6 presents these values used for the simulation. Since none of these components depend on sunlight and eclipse periods, values are applicable for hot and cold cases.

<u>Component</u>	<u>Average waste heat</u>
EPS	1.31 W
ACS	0.75 W
C&DH/CPE	1.85 W
MEMS	0.12 W
Torque Rod (each)	0.015 W
Magnetometer	0.7 W

Table 6. Heat dissipation of high frequency devices.

For the low frequency devices the power requirements were also derived from the power budget in App. D. The duty cycles are determined by the experiments. All devices depending on sunlight for their duty cycles need different tables for every orbit setup. Tab. 7 provides an overview of the used values in general.

<u>Component</u>	<u>Waste Heat</u>	<u>Duty Cycle</u>
SMS	1.63 W	4.82 min @ beginning and end of sunlight
VISIM camera	0.4 W	5.42 min @ beginning of sunlight
VISIM controller	5.6 W	5.42 min @ beginning of sunlight
Langmuir probe	1.6 W	Ground station coverage
CERTO	16.39 W	Ground station coverage
RF (Tx/Rx in C&DH box)	15 W	10 min @ mid of sunlight during orbit 11 – 14
RF-Switch	2 W	10 min @ mid of sunlight during orbit 11 – 14

Table 7. Heat dissipation of low frequency devices.

Possible ground station coverage was obtained from orbit simulations with the Satellite Tool Kit (STK). This coverage can be found in App. J. The accumulated ground station coverage was exported to a text file, which could be imported into I-DEAS. All other duty cycle tables are presented in App. K. These smaller tables were keyed in directly. For both VISIM components the same table was used only with different

multipliers. The non-geometric element representing the C&DH/CPE was connected to two boundary conditions, because a part of the heat is constant, and a part is time varying.

The CERTO and Langmuir probe duty cycles (App. J and App. K) are different from the data in the given power budget. But the impact is small: integrating the ground station coverage over time gives 0.2728 h/orbit as an average value. This equals 17.08 %. The value in the given power budget is 20 % for the biggest part of CERTO. This proves that the power budget is a close assumption. It is valid for a scenario with all components in use.

The battery is assumed to generate heat only during discharge, which takes place during eclipse. The heat generation has dependencies on its efficiency and on energy supplied by the battery for the components. This value is taken from the power budget. Also the battery heat generation depends inverse proportionally on eclipse period. An equation for battery waste heat was developed:

$$P = \frac{(1 - \eta) \cdot W_{ecl}}{\eta \cdot \Delta t_{ecl}} \quad (V.4)$$

App. L provides calculations for battery heat generation. The results are 0.843 W for a cold case and 0.682 W for a hot case scenario. The provided power budget is used for all power scenarios, to simplify the model. This means that the battery waste heat is not adjusted for every power scenario but for the different orbit scenarios. This might be justified by the fact that the power budget is only an assumption.

The heat generation of all components is 13.99 Wh/orbit for a cold case and 14.11 Wh/orbit for a hot case, if all components are turned on.

E. CONTACT CONDUCTANCES

I-DEAS calculates heat transfer only between elements that share nodes. This means that conductances for other physical connections have to be established using “thermal couplings”. For the thermal model of NPSAT1, thermal couplings were used to

represent different kinds of connections. The non-geometric elements representing the components had to be coupled with the mesh of the decks using a specific number of bolts. Different thin-shell element meshes had to be coupled between structural panels and decks, structural panels and solar cells, and the Lightband and a deck. Thin-shell element meshes needed to be coupled with a beam mesh at the bolting joints of the longerons to structural panels and decks. Other couplings had to take washers and spacers into account, outer plates to antenna ground plates, and antenna ground plates to patch antennas.

Establishing these thermal couplings is done by choosing primary and secondary elements and entering a value, that specifies the conductance. Each conductance resulting from a bolted joint was modeled as a thermal coupling between two elements. For this reason the number of bolts determined the number of elements and by this the element size. (Chapter V.B) Concerning the component – deck connection, the element choice for thermal coupling was made according to the drawings in App. E. Since the deck layouts are not yet entirely designed, dimensions for component location are not available. The twelve corners of the decks and the three beams were used for orientation. A lot of different conduction types are available in I-DEAS. "Absolute" was chosen because it does not take the surface area for the primary element into account during solve. This parameter is considered in the calculation of the conductance value in a much more precise way. The element size was chosen depending on other parameters (Chapter V.B) and does not influence the mounting connection. The "Absolute" conductance type creates a conductance between the primary element and the nearest secondary element with the value entered. Non-geometric elements can only be used as primary elements, because otherwise they would exchange heat with only one element on the mounting deck. This restriction has no influence on the conductance, because it is always a two-way conductance. A list of the connected elements for subsystem mounting can be found in Ref. 25.

The conductances were calculated using the equations presented in chapter III.E. As mentioned in that chapter the equations are derived from test results and are more or less approximations rather than exact. All contact conductances were calculated with all three equations. Therefore, different parameters used in these equations had to be

defined. All parameters and results can be found in App. M. The coefficient of expansion, the thermal conductivity and the yield stress depend on temperature. They were derived from Ref. 2.

Comparing the calculation results against each other and with other experimental results (App. M) it was decided to use the dimensional equation from Gluck (Equation III.16). This has also the advantage of depending basically only on the screw size. This is useful, because we need conductance values not only for the classical case of two plates mounted to each other surface to surface. But where the structural panel is bolted to the decks, the plates are at a rectangular angle. Therefore no thickness of one of the decks can be obtained. The used value is just an assumption to make the equation from Bratkovich applicable.

The calculation of the spacer and washer connection could not be done with the given formulas, since there is no direct connection from surface to surface. The dielectric ellipse between patch antennas and antenna ground plate is assumed to be a perfect thermal insulator. Therefore only the bolt conducts heat. The connection between antenna ground plate and the outer decks consists of a screw and an aluminum spacer. Hence the total heat conductance is the sum of both. Using equation III.1 in equation III.11 leads to equation V.5, which was used for these conductance calculations:

$$C_j = -k \cdot \frac{A}{l} \quad (V.5)$$

Here, A is the cross-sectional area of the joint. A table with all calculated values can be found in App. M.

F. ENVIRONMENT

Radiation within the spacecraft is not modeled to simplify the model. This is appropriate, because "for the relevant temperature range, -50 to 110 ° C, the amount of heat transferred via radiation is generally very small compared to the amount transferred by conduction" [Ref. 5, p. 249]. But for heat exchange with space, this is the only mode of heat transfer available. To use radiation in the I-DEAS model a "Radiation Request"

was turned on and simply "all radiation" was chosen. So far, all thin-shell elements have optical properties only on their front side. To control the front side, the display option "Element Triad" was turned on. The triad indicates the front side of an element. The "Element Reverse Connectivity" was used on element groups that were inside-facing. This turns the triad orientation around. After this, only the two decks in NPSAT1 that have no space-facing surfaces, would take part in radiation. To turn them off an "Element Radiation Switches" was created and "Ignore Elements for all View Factor Calculations" was chosen.

For accurate radiation modeling reverse sides had to be created. This means, that a thin-shell element has defined optical properties on its backside. This was necessary for the solar cell arrays and the antenna ground plates. The solar cell reverse sides were considered for radiation because they are very close to the structure (0.05 mm) and a significant heat exchange via radiation could be possible. Therefore, "Reverse Sides" for each group of solar cell array meshes and for the two antenna ground plate meshes were created. This was considered useful, instead of creating reverse properties in the material definition, which is also possible, because it might be necessary to change the properties of a material used at different locations as a result of the analysis. This reverse side can be modeled as different elements or not. In this model, the reverse side switch without creating new elements was used. The creation of new elements for the reverse side allows different temperatures within a thin shell element. This is only necessary, if the single temperatures are post-processed. But creating more elements increases the computation effort and needs to model contact conductance between the front and reverse side elements.

Another environmental parameter is the space itself. Therefore the "Space Enclosure" in the "Radiation Control" was turned on. It is an entity, which during the analysis constructs a huge geometry around the model. It consists of large temporary surface elements. View factors can then be calculated for these surface elements. They are automatically merged into a single calculation point prior to solving. The temperature for this enclosure is constant at absolute zero, which is default.

Finally the orbit has to be set up. This set up is described here, so that in the next chapter just the parameters are presented. An “Orbit / Attitude Modeling” was created. The setup consists of four steps after defining the planet and the orbit method (an orbit can be defined in different ways). The first step is to define the “Planet and Sun Characteristics”. Earth geometrical parameters are just taken from default values. Earth IR, albedo and solar flux are keyed in as described in chapter VII.C. The “Orbit Parameters” require values for altitude and, according to the orbit method, a beta-angle or other defining parameters. The “Orbit Attitude” requires only a nadir and a velocity vector. These are taken from Fig. 1 and are defined by clicking on points in the model. The “Calculation Positions” needs a value that defines the start point on orbit (see Chapter V.D.2) and a number of intermediate calculation positions. This adjustment of the start point was done depending on the start angle from a reference. As reference “Local noon” was chosen. In other words the orbit starting point was defined as an angle from the middle of sunlight position. This angle was calculated from the known sunlight duration (Tab. 2). The whole orbit (360°) equals 1.5975 h. For a cold case half a sunlight period (0.5021 h) therefore equals 113.15° . Because of the way this angle is measured, the angle from reference that had to be entered is the difference to 360° : 246.85° . For a hot case this angle is 218.0873° . For the number of intermediate calculation positions the default value “twelve” was taken. This means that the planet and sun characteristics are recalculated at twelve equidistant positions during an orbit. After all settings are made, the result can be viewed in the “Orbit Display” (Fig. 8 is taken from this).

VI. DATA-TRANSFER SCRIPT

The post-processing of this work was done in a spreadsheet program instead of in I-DEAS itself. The reason is that this offers more possibilities in comparing data and is more convenient to handle, i. e. for creating charts. I-DEAS output files are ASCII files. For every simulation run a temperature file is created ("TEMPF"). This file contains all element temperatures for all time steps. Although it is just a text-file, the transient runs with the NPSAT1 thermal model resulted in file sizes about 127 MB. The structure of this file is very simple, for it consists only of two columns: the element number in ascending order and the associated temperature. This repeats for every time step. Another file created during a simulation run is the report file ("REPF"). This file contains much information about the run (like orbital parameters) and also maximum, minimum, and average temperatures, as well as heat flow for the defined element groups. Also the information defined in the "Printout Options" is written to this file. Its structure is much more complex than that of the temperature file. Not every line looks like the other, and it contains also text. The format of blocks of information is the same for every time step.

The purpose was to extract the data of interest from the I-DEAS output files. To minimize the programming effort, a script language was used, in this case Python. The data was then written into a comma separated value file (*.csv). If the scripts are located in the I-DEAS run directory, the file handling is very simple, too.

This chapter describes the basic functionality and structure of a Python script for handling TEMPF and REPF files. The source code can be found in App. N. Different versions of the files, to extract different data, are available from Ref. 25.

The temperatures of interest were obtained from the TEMPF file. Therefore, the non-geometric elements, which represent the components, were given a specific label. Labels from any other element were taken from the model file, by simply turning on the labeling in the I-DEAS graphics window. The script for extracting and converting reads the first column (containing the labels) and if the value equals a demanded value, the temperature was written to the csv-file. Also, the actual simulation time for every time

step was added. The fact that the properties of the source file were known (i. e. being sorted) simplified the script. Fig. 15 provides a flow-chart of the script.

From the report file the heat flow through the mounting bolts and the heat input of the battery was extracted. Through the heat input it is possible to see when a heater is turned on, which is necessary to recalculate the power budget. “Convection” in combination with the element label was used to extract the desired heat flow. Convection does not necessarily mean convection, but every heat exchange between elements without physical connection. “Heatsum” in combination with the element label was used to recognize the end of the data for each time step. It was not possible to use the appropriate data types for the values. Some lines contain, for example, characters or spaces at these positions and Python cannot handle this. Therefore “string” was used. But in the result this is not important, because the written comma separated file is a text file anyway. Fig. 16 shows a flow-chart of the REPF script.

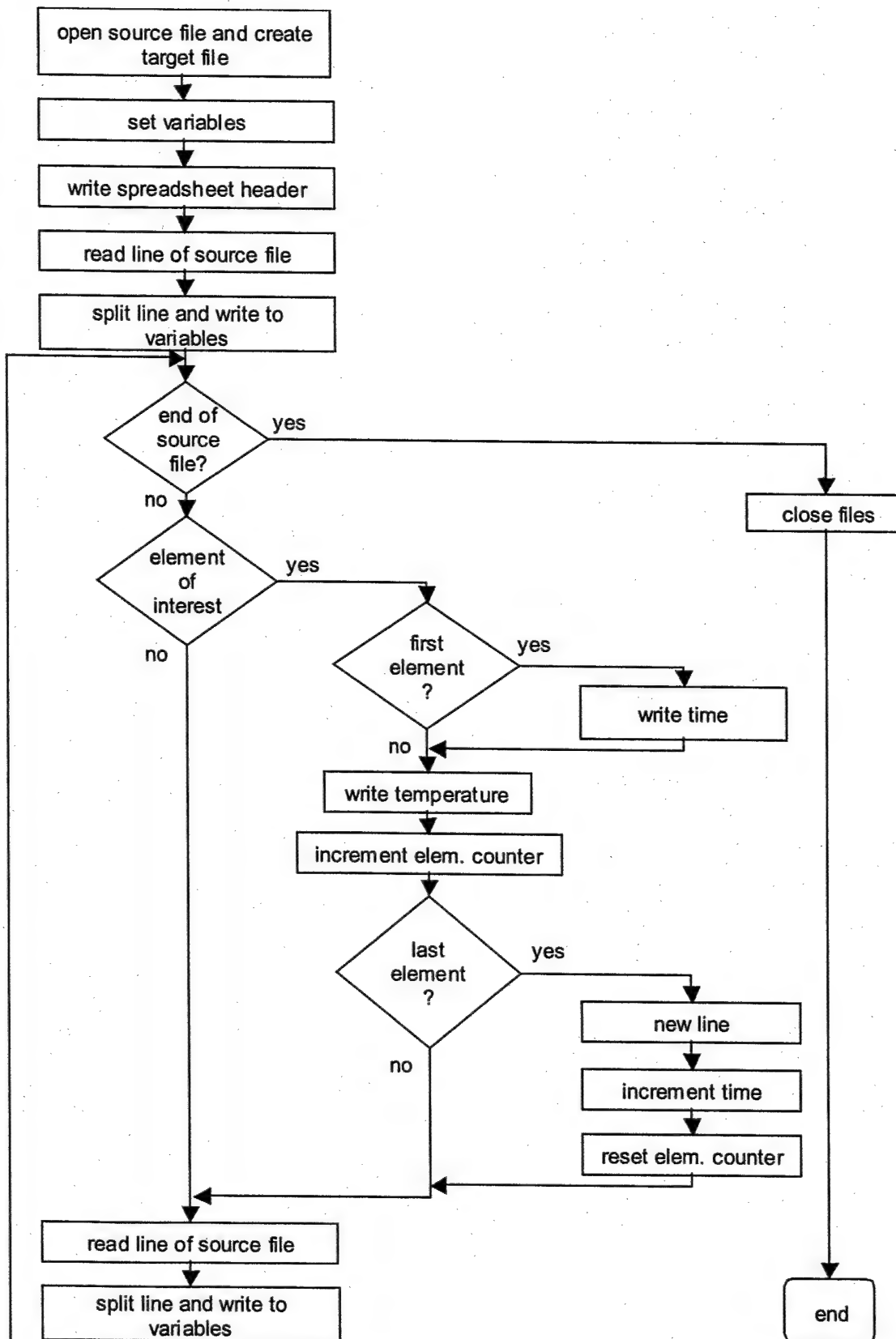


Figure 15. Flowchart of Python script for TEMPF extraction.

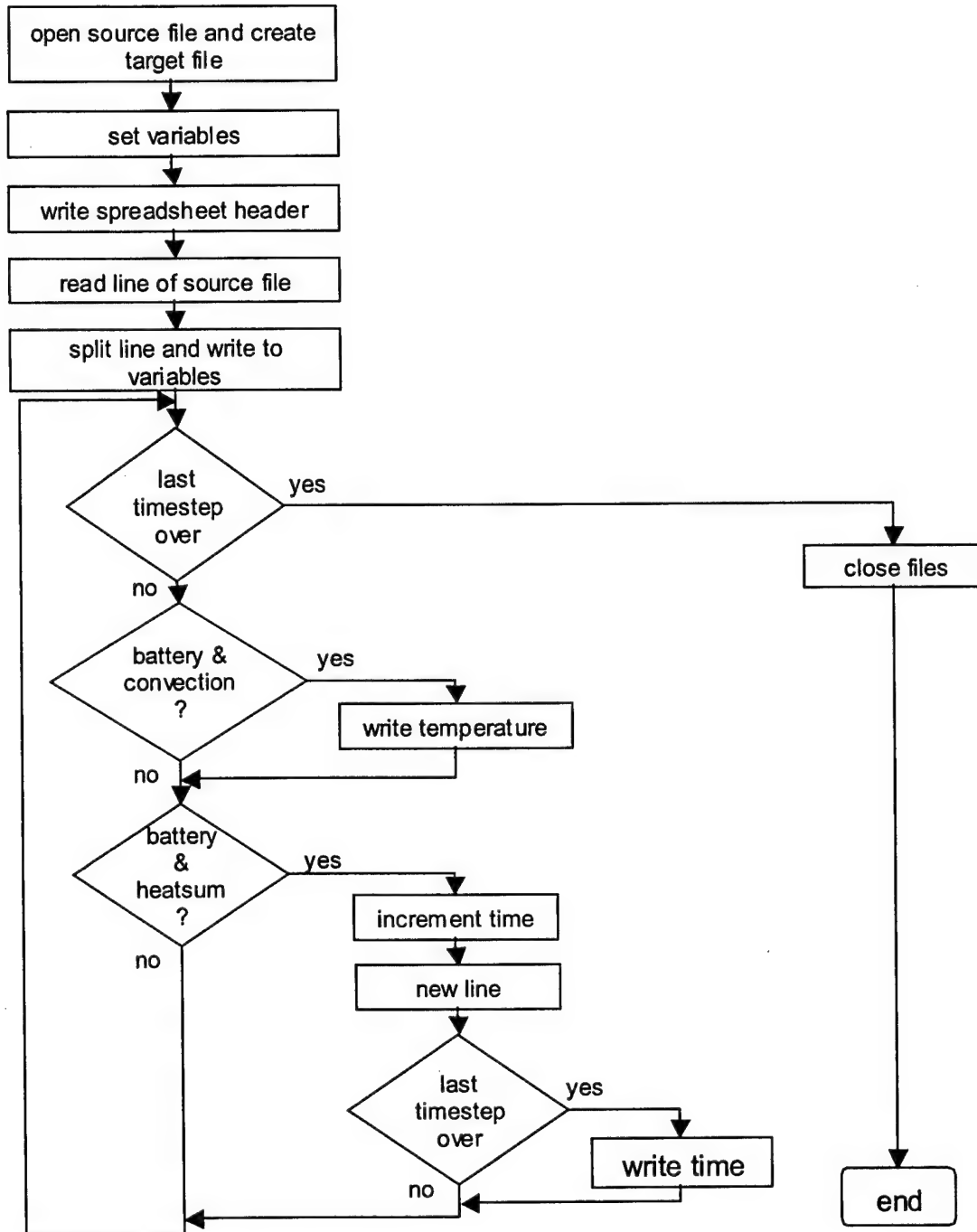


Figure 16. Flowchart of Python script for REPF extraction.

VII. NPSAT1 THERMAL ANALYSIS AND RESULTS

A. MODEL VERIFICATION

The initial design of NPSAT1 was simulated with both calculated component capacitances (chapter V.D.1). A higher thermal capacitance causes a solid to respond more slowly to changes in its thermal environment. Therefore, the lower thermal capacitance reaches a higher peak temperature and the average temperature is not influenced. This can be seen in the comparison in Fig. 17. CERTO is shown since its temperatures vary most during on orbit operations. The low capacitance is 407.36 J/K and the high capacitance is 1224.72 J/K. The difference in the temperature range is very small. Results from all other components show the same effect. In further simulations the higher capacitances will be used. Most of the following discussions are based on average temperatures. For that the capacitance difference is not of any interest.

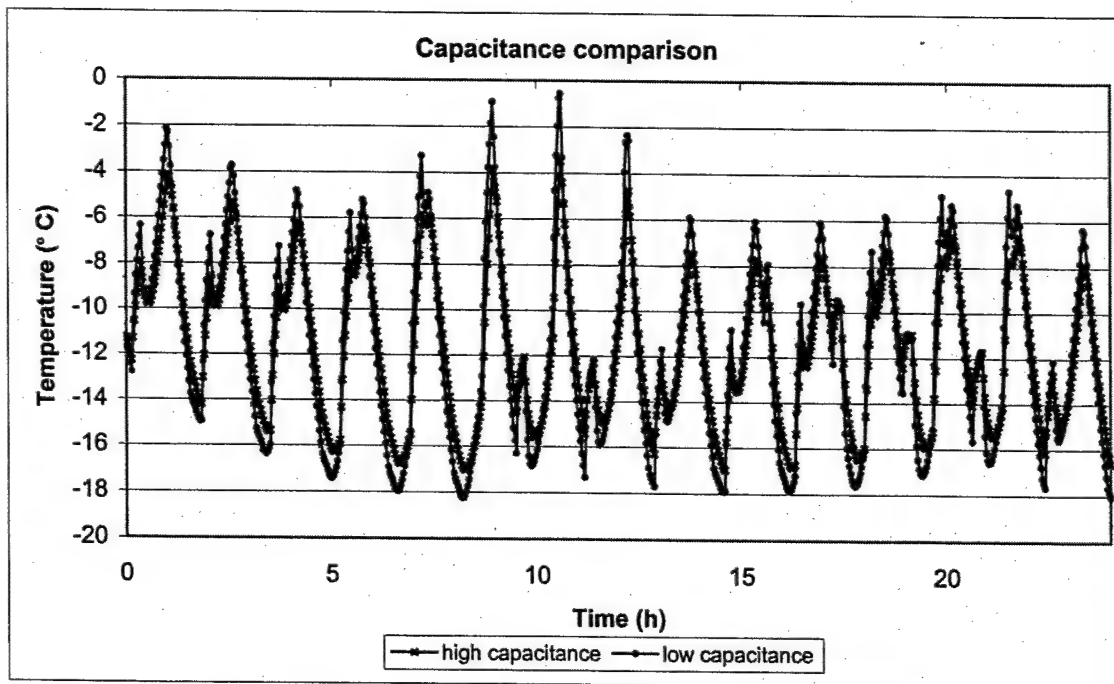


Figure 17. Capacitance comparison for CERTO.

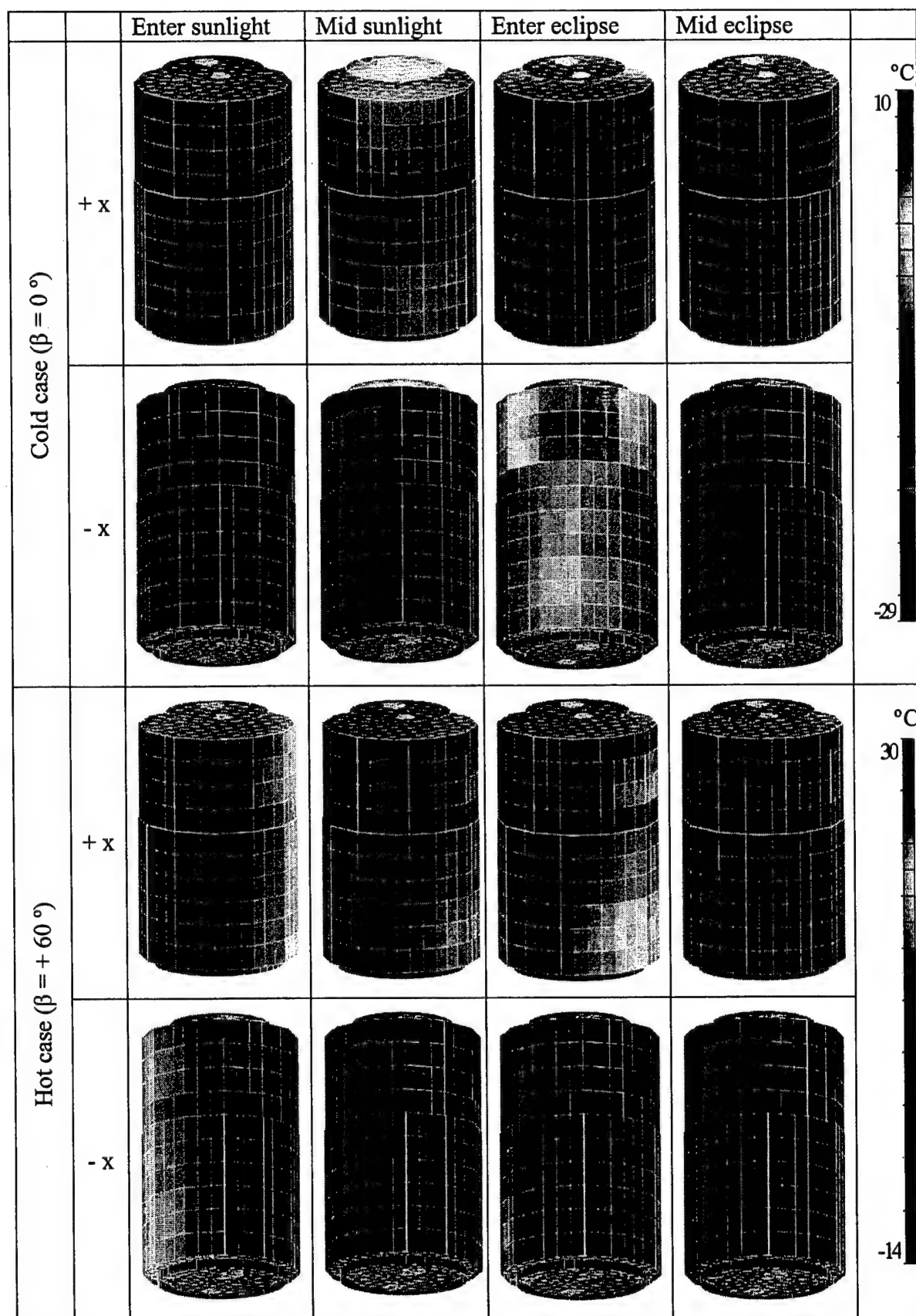


Figure 18. Spacecraft temperatures during orbit.

The next decision that had to be made was which elements to post process. Fig 18 shows the spacecraft during hot and cold case beta angles in four specific orbit positions. The correlation between orbit type and temperature spreading was already discussed in chapter IV.A. All pictures are taken from the I-DEAS Visualizer. They were taken at orbit 12 to avoid influences from transient effects at the beginning of the simulation.

For the cold case on the outside of the spacecraft the zenith facing side experiences the largest temperature changes during orbit, since it directly sees the sun or looks into cold space, whereas the nadir facing side always sees the Earth. It can be seen that the spacecraft faces the most extreme temperatures on its $+x$ and $-x$ vector orientations during the cold case. Therefore the biggest interest in the solar cell temperatures is on the cells next to the fourth deck on the front and rear side. Since the nadir-facing side has fairly stable temperatures, only the patch antennas on the zenith facing side are of special interest. Fig 19 shows the processed elements for the solar cells.

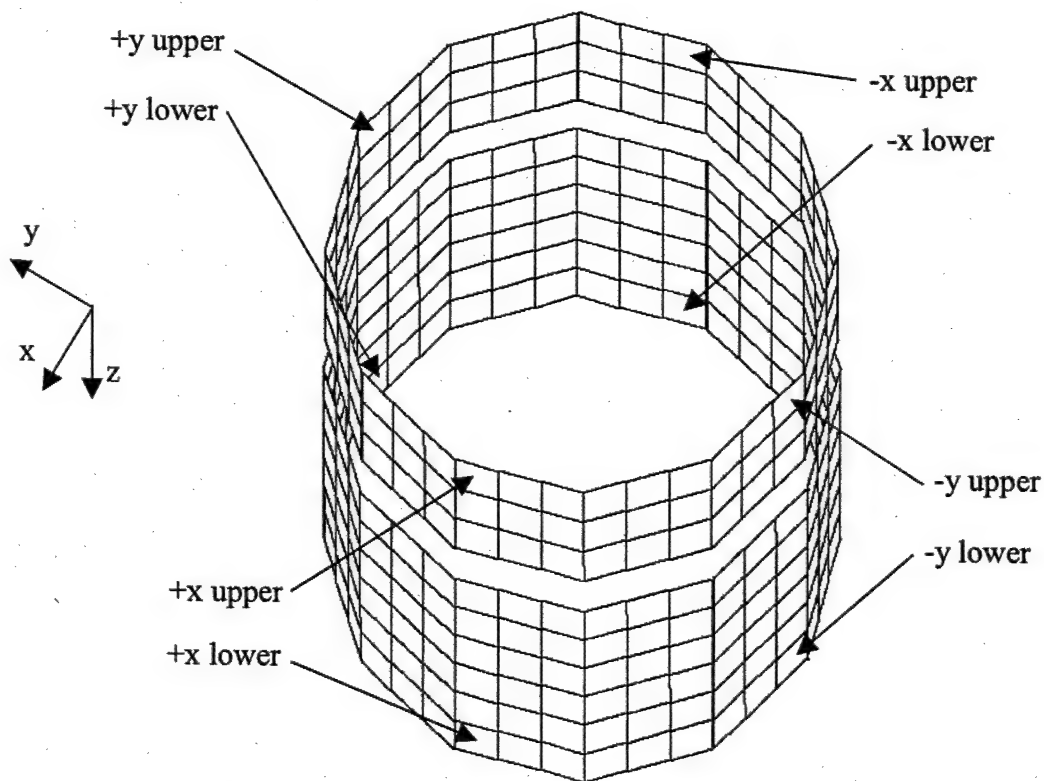


Figure 19. Post-processed elements of solar cell mesh.

For the hot case, also the nadir facing side has fairly stable temperatures. The most extreme temperatures occur on the orbital normal. The +y side faces the coldest temperatures and the -y side gets hottest for the positive beta angle. Therefore the solar cells are post processed on these positions next to the nadir and next to the zenith facing side since the solar cell panel in the middle has less temperature variations (Fig. 19).

Since the patch antenna mesh is a circular arrangement of elements, just one arbitrary element was chosen. For the deck temperatures one element from the center of each deck was taken for presentation in this work.

A close look has to be taken at the subsystem temperatures because they have special limits. RF-Switch and the torque rods are removed from the result sets for this presentation of the results since they are of less interest. The post-processed elements are directly the non-geometric elements that represent the subsystems. All extracted data from the I-DEAS TMG results files can be found in Ref. 25. It contains also the data, where all presented charts are derived from, as well as the I-DEAS TMG model file.

To shorten descriptions of the different simulations in the following chapters some basic scenarios are defined. Tab. 8 shows power scenarios, with subsystem from highest to lowest priority. Tab. 9 provides surface properties for BOL and EOL for the materials that are used after the design change for all case studies. Optical properties for BOL of the initial design can be obtained from Tab. 5.

ACS			
Battery			
C&DH	Minimum		
EPS			
RF		Low	
CERTO			Maximum
Langmuir Probe			
SMS			
CPE			
MEMS			
VISIM			

Table 8. Power scenarios.

	<i>Material</i>	RM-550IB	Solar Cells, commercial	Solar Cells, experimental	Copper
<i>BOL</i>	<i>Absorptivity (α)</i>	0.97	0.724	0.754	0.3
	<i>Emmissivity (ϵ)</i>	0.91	0.85	0.85	0.03
<i>EOL</i>	<i>Absorptivity (α)</i>	0.97	0.755	0.754	n/a
	<i>Emmissivity (ϵ)</i>	0.88	0.85	0.85	n/a

Table 9. Optical BOL and EOL properties for worst-case scenarios.

B. DESIGN EVALUATION AND DEVELOPMENT

1. Initial design

The first run should represent an orbital situation, which NPSAT1 can realistically face. As seen in Fig. 7 a beta angle of 0 ° happens to the spacecraft during operation. To analyze this in a first run makes sense, since preliminary analysis as well as the performed hand calculation raised the concern of NPSAT1 getting too cold, also the already calculated duty cycles for the low frequency devices could be used in this run.

The components were all turned on, which represents a normal situation of NPSAT1 on orbit. The optical material properties were chosen to represent BOL and the planet and sun characteristics were simply used as default in I-DEAS TMG. The analyzed period was chosen to be one day.

Finally the spacecrafts orbit had to be adjusted with the sun and planet parameters by defining the start angle from local noon (chapter V.F). All parameters for this run are summarized in Tab. 10. Results can be seen in Fig. 20 – Fig. 24.

Power dissipation	Maximum, with cold case tables (chapter V.D.2, App. K)
Surface properties	BOL
Beta angle	0 °
Start angle from local noon	246.85 °
Solar flux	$1377.2 \frac{W}{m^2}$
Earth IR	$236 \frac{W}{m^2}$
Albedo	30 %

Table 10. Normal orbit parameters.

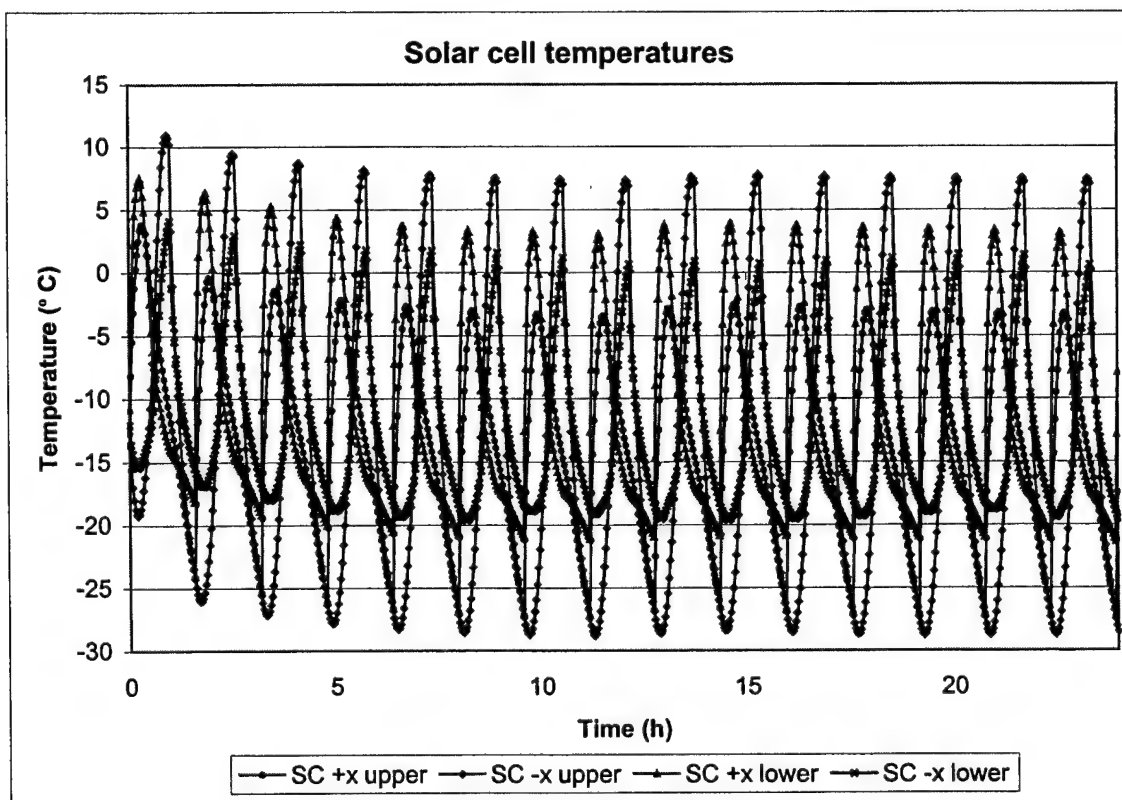


Figure 20. Solar cell temperatures on normal orbit.

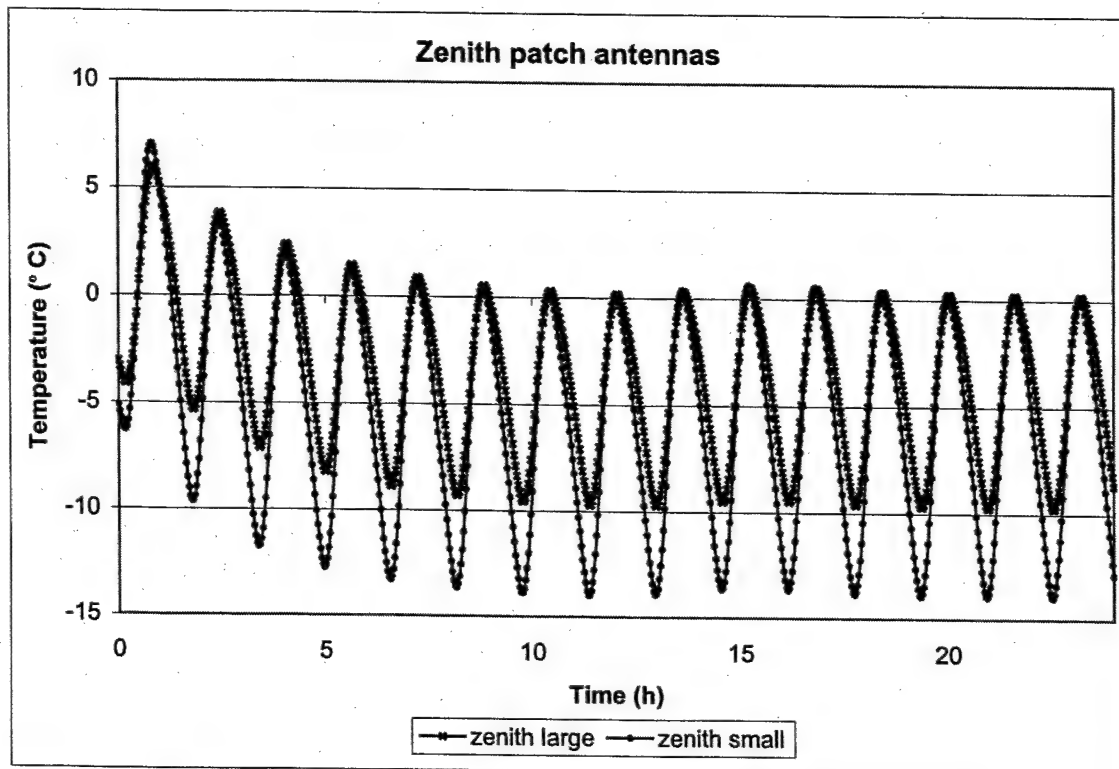


Figure 21. Third deck components and patch antenna temperatures on normal orbit.

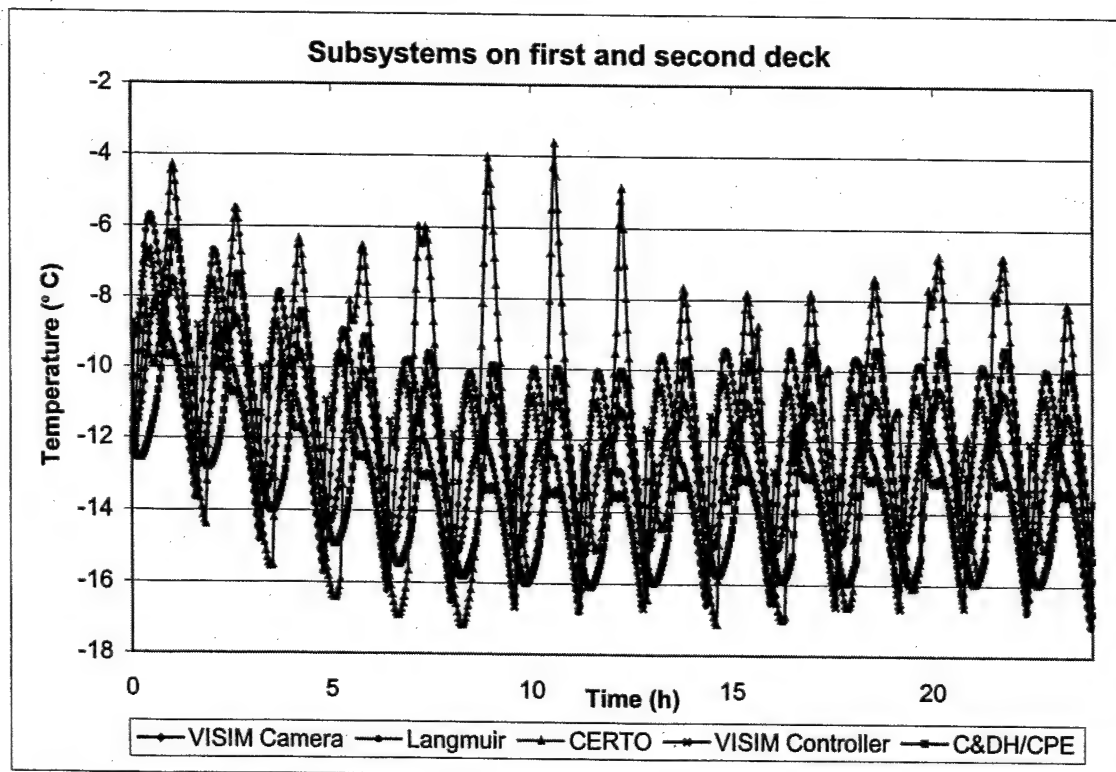


Figure 22. Subsystem temperatures on first and second deck of normal orbit.

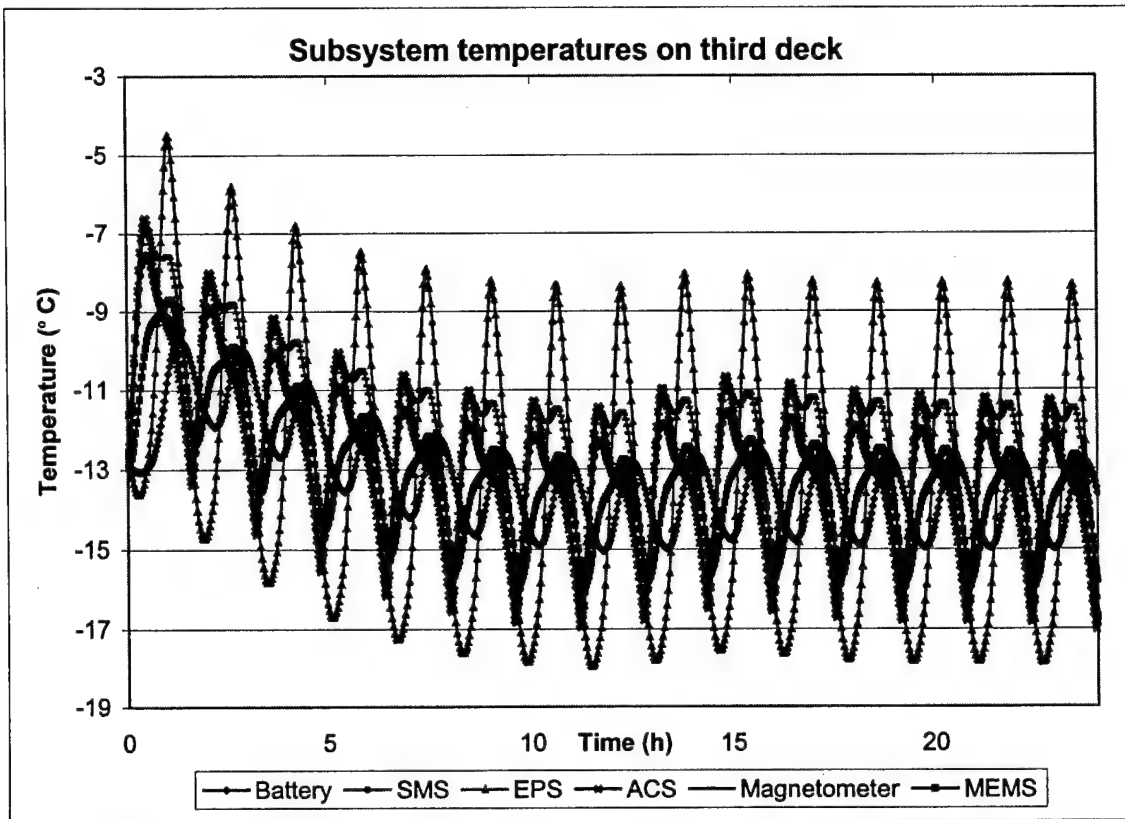


Figure 23. Subsystem temperatures on third deck of normal orbit.

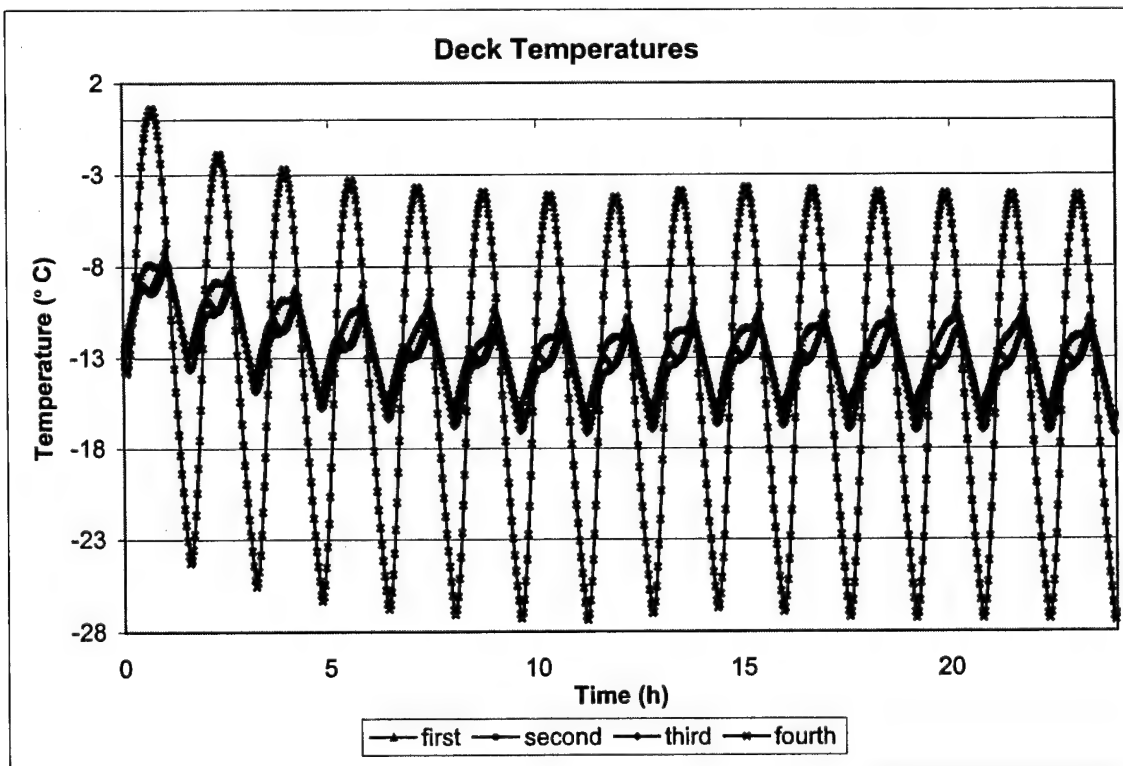


Figure 24. Deck temperatures on normal orbit

In the following discussion, transient effects at the beginning of the simulation runs will be neglected, because they are only due to the initial conditions for the simulation setup and do not reflect any real conditions. As Fig. 21 and Fig. 22 show most of the components face temperatures in the range of about -9 to about -17 ° C. CERTO gets warmer. During operation it reaches almost -3 ° C. MEMS has a smaller temperature range of about -12 to -16 ° C. EPS faces the largest temperature changes from -8 to -18 ° C. The battery temperatures vary from -12 to -15 ° C. Comparing all this to the temperatures limits presented in Tab. 3, the battery is the only component that does not reach its requirements. All other components have a margin of at least 7 K to the lower limit. But the battery temperature is between 27 K and 30 K too cold. The decks face temperatures between -10 ° C and -17 ° C, except for the fourth deck, that does not carry any components and is therefore not of great interest. The aluminum structure of the satellite does not have any significant temperature limits.

For the patch antennas the concern was, that they might get too hot, because the α/ϵ coefficient of copper is 10 (Ref. 5), which is very high. Therefore the zenith facing side was analyzed, since it faces the most extreme temperatures (Fig 18). As Fig. 21 shows, the patch antenna temperatures do not exceed any temperature limits for electronic devices.

The solar cells also operate in appropriate temperature regimes during on orbit operations. Fig. 20 shows the solar cells facing the most extreme temperatures. It can be seen, that the cells located next to the zenith facing side have a higher temperature range than the cells next to nadir facing side.

To learn more about the behavior of the battery, the heatflow through the mounting bolts was analyzed. The heatflow of the battery can be seen in Fig. 25. Because of the transient effects at the beginning and the incomplete orbit at the end, the heatflow of nine orbits from the middle (orbit 6 – 14) was taken and integrated over time. The result is, that the battery loses an average of 0.6178 Wh/orbit or 9.2187 Wh/day. This means that although the battery is too cold, it dissipates more heat to the satellite structure than it gains from there to reach the heat balance.

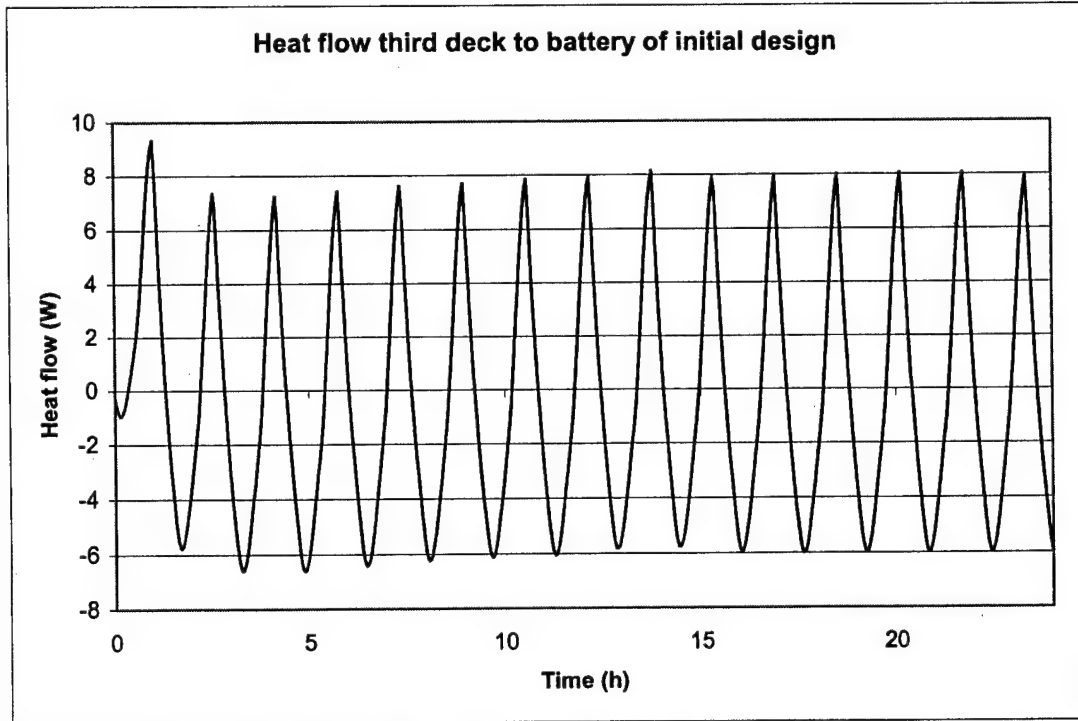


Figure 25. Heat exchange of battery during normal orbit.

2. Insulation changes

A way to make a design change with impact on the thermal control is to change the conductance between the battery and the deck to which it is mounted. This means to insulate it more or less against the environment since this conduction is the only heat path between the battery and anything else, because radiation within the satellite is minimal. It would also be easy to make this design change, because this connection is not yet designed. Theory shows, that stronger insulation slows down heat exchange, because it decreases thermal conductivity. Therefore the temperature range should be smaller with a stronger insulation and if the heat generation of the battery is high enough, stronger insulation should increase the average temperature.

Besides this qualitative view, different simulation runs with possible design changes of the interface were performed to quantify this effect for NPSAT1's battery. At first the spacers were taken out, which increases the conductance. Then, again with spacers, the number of bolts was reduced from six to four to decrease the conductance. Finally four Teflon spacers were used, which also insulate the bolts, to reach a very high

insulation between battery and deck. For this simulation an end of the transient phenomenon could not be recognized within the usual 24 h run. This can be seen in Fig. 26. Therefore this design was simulated over 2.5 days on orbit. To keep the data in a manageable size, the time step was increased. But the frequency of the low frequency devices (Tab. 7) had to be taken into account to avoid loss of a duty cycle between the measurements. With respect to the SMS, four minutes, instead of two, was chosen as a new time step.

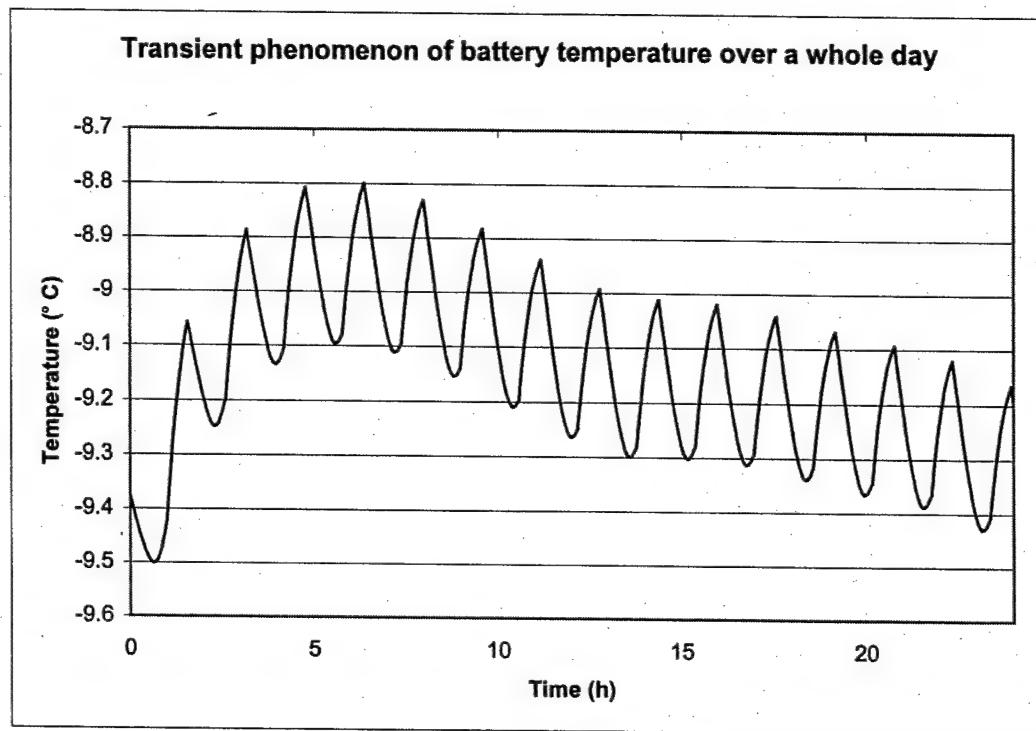


Figure 26. Transient phenomenon over a whole day.

All conductance values and results are presented in Tab. 11 and compared to the original design approach. To avoid failures because of the transient effects at the beginning of the runs and the incomplete orbit at the end, all data was calculated based on orbits 6 – 14, except for the simulation with the Teflon insulation. Here also nine average orbits were taken (28 – 36 from a little more than 37 orbits).

Design	Less insulation	Original	More insulation	Highest insulation
No. of bolts	6	6	4	0
Spacer	-	al	al	teflon
Conduct. / contact (W/K)	0.71	0.245	0.245	0.0209
Average temp (° C)	-13.938	-13.768	-12.871	-9.38
Heat loss per orbit (Wh)	0.64	0.62	0.6	0.48
Heat loss per day (Wh)	9.58	9.22	9.08	7.21

Table 11. Insulation changes and results.

It can be seen that the insulation increases the average temperature and decreases the heat loss. But the effect that can be reached with possible configurations and materials is too small compared to the desired change. These changes should be made anyway, since they do have a positive effect. The comparison of the results also shows, that the insulating effect has an impact on the simulation since it extends the transient phenomenon at the beginning of the simulation. To see how insulation variation also changes the temperature range, Fig. 27 provides a comparison of the initial design and the highest insulation scenario for the normal orbit. Therefore an additional run over 2.5 days with the initial conditions was performed.

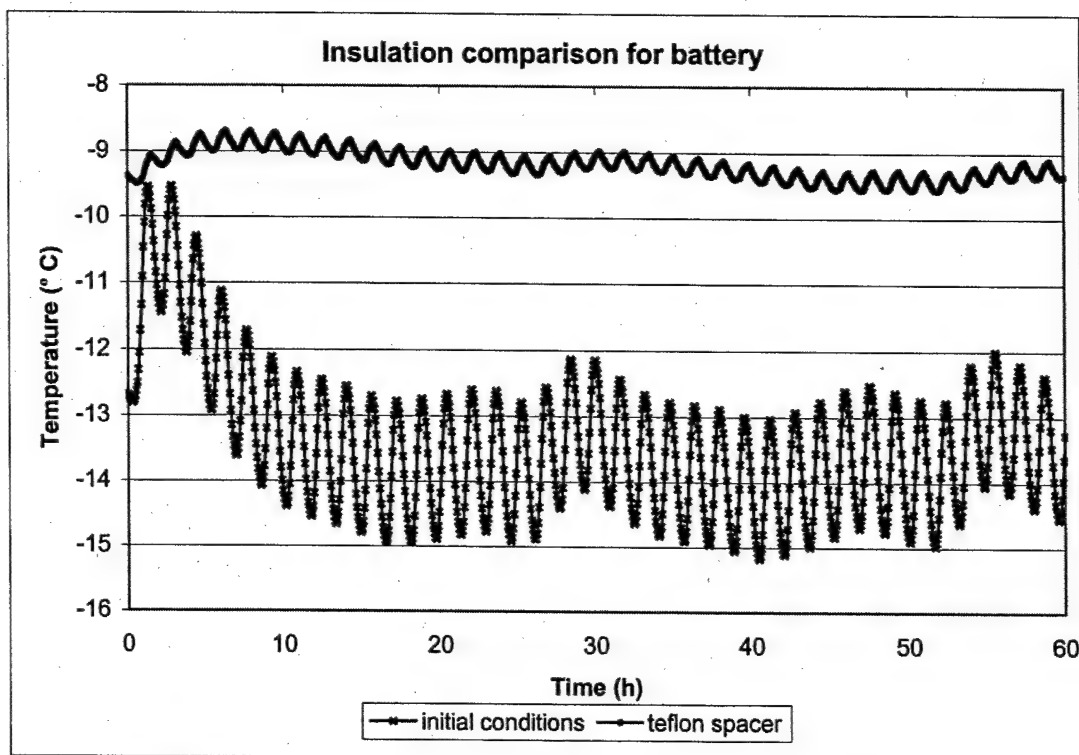


Figure 27. Insulation comparison for battery temperature.

3. Changes in surface finishes

Since modifications to conductance values were insufficient to meet requirements, the next approach was to add energy. Raising the overall temperature would result in a temperature balance between battery and structure at a higher level. The step to achieve this was a change in thermal finishes on the outside of NPSAT1. The properties of the solar cells, which cover most of this surface, cannot be changed, but the other surfaces could be covered with a black finish, that has high absorptivity and low emissivity values. As mentioned in chapter III.B a high α/ϵ ratio helps to collect energy. So, the gold and the black anodized surfaces were to be given new optical properties. Also Aerospace Corporation proposed to use another surface finish than gold anodized aluminum (chapter IV.A). Ebanol C black, a metal conversion coating, was chosen from Ref. 5, to analyze a material with very useful optical properties. This was recognized to be a better proceeding than just using arbitrary values. To make a statement concerning the amount of the effect another material would have on the temperature, the simulation was needed

again. Properties can be obtained from Tab. 12. Also results and a comparison to the design chosen in the last design change (insulation) are shown.

	Initial design ¹	Ebanol C black	Z 306 black paint	RM-550IB
Absorptivity	0.48/0.65 ²	0.97	0.95	0.97
Emissivity	0.82/0.82 ²	0.73	0.87	0.91
Ratio α/ϵ	0.59/0.79 ²	1.33	1.09	1.07
Average T. ($^{\circ}$ C)	-9.38	0.99	-2.1	-2.4
Heat loss per orbit (Wh)	0.48	0.49	0.49	0.49
Heat loss per day (Wh)	7.21	7.36	7.36	7.36

Table 12. Finish changes and results.

Since it was recognized, that the change in the optical properties has such a large impact on the overall temperature, other suitable finishes that could realistically be used in the design of NPSAT1 were simulated: Z306 polyurethane paint (also EOL values are available) and RM-550IB (flight-proven and low degradation). Results can also be seen in Tab. 12. The decision was made to choose RM-550IB, since this is flight proven and offers low degradation in a low Earth orbit. This decision was needed at this point to have a basis for further design steps.

Comparing the α/ϵ ratios of the black paints to the used gold and black anodized surfaces it can be concluded, that the initial design approach would not be very suitable. From the results it can also be seen, that the battery loses less of its own heat, when the heat balance is at a higher level. Between the different black coatings there is no significant change in the heat loss. A comparison between the initial design for this part of the analysis and the resulting design is presented in Fig. 28.

¹ after insulation change (chapter VII.B.2)

² gold anodized/black anodized

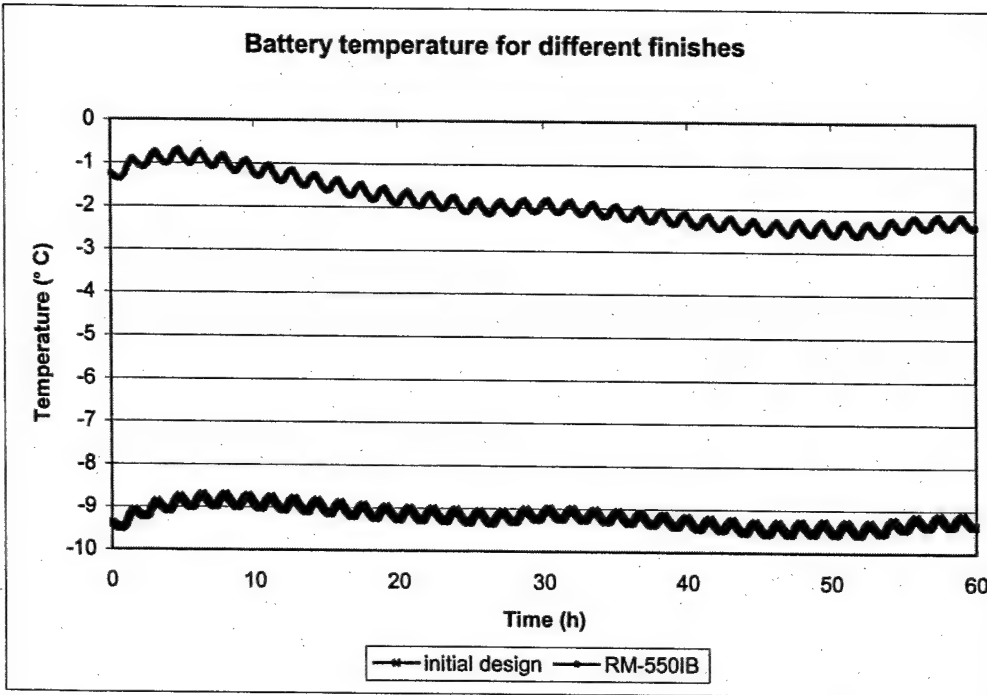


Figure 28. Finish comparison for battery temperature.

4. Heater addition

Since the temperature of the battery is still too low and all suitable passive thermal control devices (chapter IV.C) have already been examined, an active component was taken into account. A heater (Fig. 29) is required in the battery box. Until now, it was just a contingency, since it would be difficult to add after the design is frozen. The heater generates a constant power of 5 W. Next an analysis was carried out if simply turning on this heater could help to meet the thermal battery requirements. The result is shown in Fig. 30 for the last 24 h of the 2.5 days simulation run. It is obvious, that this heater use is inappropriate. The average temperature calculated from orbits 28 – 36 is 58.91 °C. Compared to the requirements in Tab. 3 the battery gets far too hot.

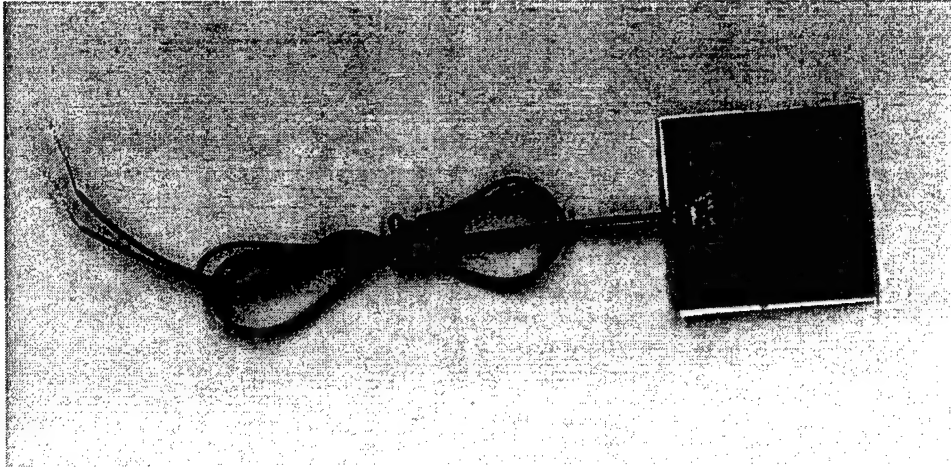


Figure 29. Micro heater 5 W.

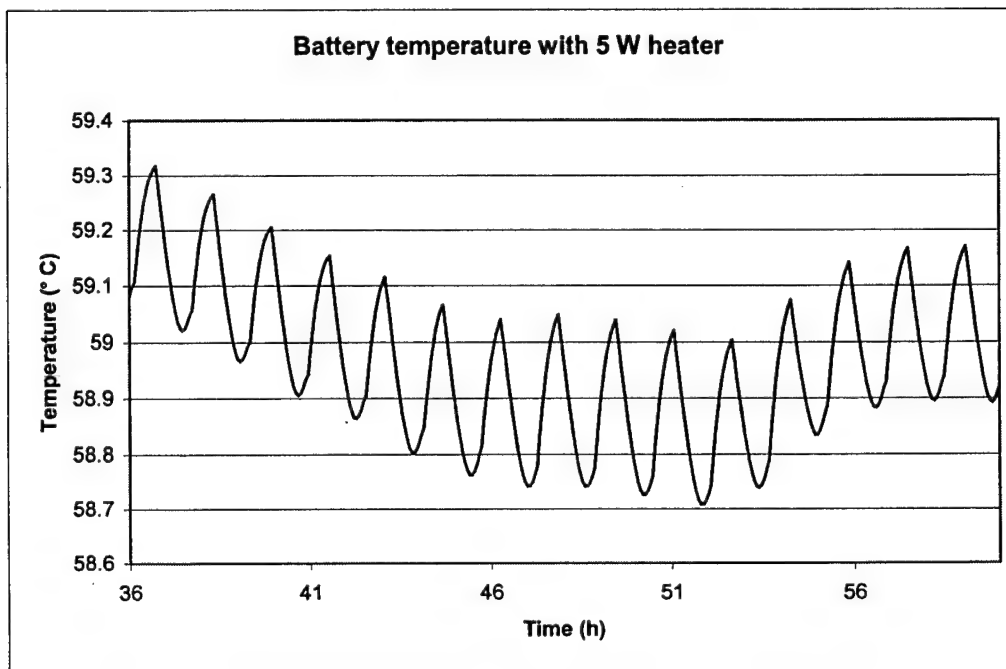


Figure 30. Battery temperature with constant 5 W heater input.

5. Thermostat addition

Turning on the heater generates far too much energy, as seen in the last chapter. To deal with this effect, the insulation could be reduced or the heater power could be controlled. To save power, it was decided to control heater power thermostatically. A sensor element measures the battery temperature and compares the value to a defined cut-in and a cut-off temperature. Three simulations were performed. For the first one, the cut-

in and cut-off temperatures met the temperature limits of the battery. For the second run, only the lower third of the allowed temperature range was used. For the third one a very narrow range was arbitrarily chosen, to obtain sensitivity information. The parameters and results are presented in Tab. 13. It is important to note that the last three rows only present average values that do not reflect reality. As the "orbits per duty period" row shows, the duty cycles, which result from the thermostat, do not correspond to orbits or orbital parameters. These values are calculated based on a complete period of duty.

	<i>Large range</i>	<i>Narrow range</i>	<i>Very narrow range</i>	<i>Narrow range, adjusted battery heat</i>
Cut-in $T (^{\circ}C)$	15	15	15	15
Cut-off $T (^{\circ}C)$	30	20	16	20
Orbits per duty cycle	10.98	4.09	0.61	3.96
Duty on / off (h)	7.07 / 10.47	2.13 / 4.4	0.25 / 0.72	2 / 4.33
Time heater is on (%)	40.3	32.99	25.86	31.58
Time heater is on / orbit (h)	0.644	0.527	0.413	0.5
Consumed energy / orbit (Wh)	3.22	2.635	2.066	2.52
Heat loss per orbit (Wh)	3.77	3	2.69	3.13

Table 13. Thermostat changes and results.

The heat flow from the spacecraft structure to the battery is shown in Fig. 31. Compared to the simulations without active thermal control hardware the heat flow is only towards the structure after transient effects of the simulation have ended. For the narrowest temperature range, the simulation data shows no repeating duty cycle. Therefore all values for this case in Tab. 13 are averages. It can be seen, if the temperature range is narrower, that the heater is turned on more often, but it consumes less power. Finding an optimum was not attempted because the idea is that in reality the battery will be heated more during sunlight with excessive solar cell power, so that the

heater will be turned on less during eclipse. This changes maximum and minimum temperatures as well as duty cycles. But exact parameters how this will be achieved are not known up to now. All in all it can be concluded that the use of a thermostat is appropriate. But as mentioned in chapter III.D also solid-state controllers could be taken into account for the final design. For the following runs the narrow range is used.

Since the waste heat of the battery depends on the load, the waste heat is increased. Since the heater power and the efficiency of the battery (chapter V.D.2) are known, the battery waste heat can be calculated. Therefore the total heat during heater operation is known. From this the duration of a heater duty cycle can be calculated, because the certain amount of energy, which is needed to heat the battery, is also known from the performed simulation. But this calculation was not applicable for the current model, because it would take the orbit parameter eclipse into account. The battery has to supply the heater with power only during eclipse. During the sunlight portions the energy for the heater is taken directly from the solar cells. Since the thermostat duty cycle does not depend on orbit parameters ('Orbits per duty cycle' in Tab. 13) the result would be a table for an average orbit. Therefore the thermostat was used to drive the heater, instead of calculating a table. But since the heater power requirement is fairly large compared to the previous battery boundary condition, it should be taken into account. Therefore a second table-driven battery boundary condition was created. Its duty cycle is based on the 'narrow temperature range' duty cycle. It is 'on' during the eclipse periods of the thermostat duty cycle. The value is calculated with the efficiency of the battery. The right column in Tab. 13 shows the results. Time parameters are very similar to the narrow range simulation. The consumed power decreases only very little, which proves that the explained approximation concerning the battery waste heat can be made. Fig. 32 shows how much heat battery and heater produce over time. On the other hand it can be seen, that the additional battery waste heat does fit the thermostat duty cycle less, if time proceeds, as explained above.

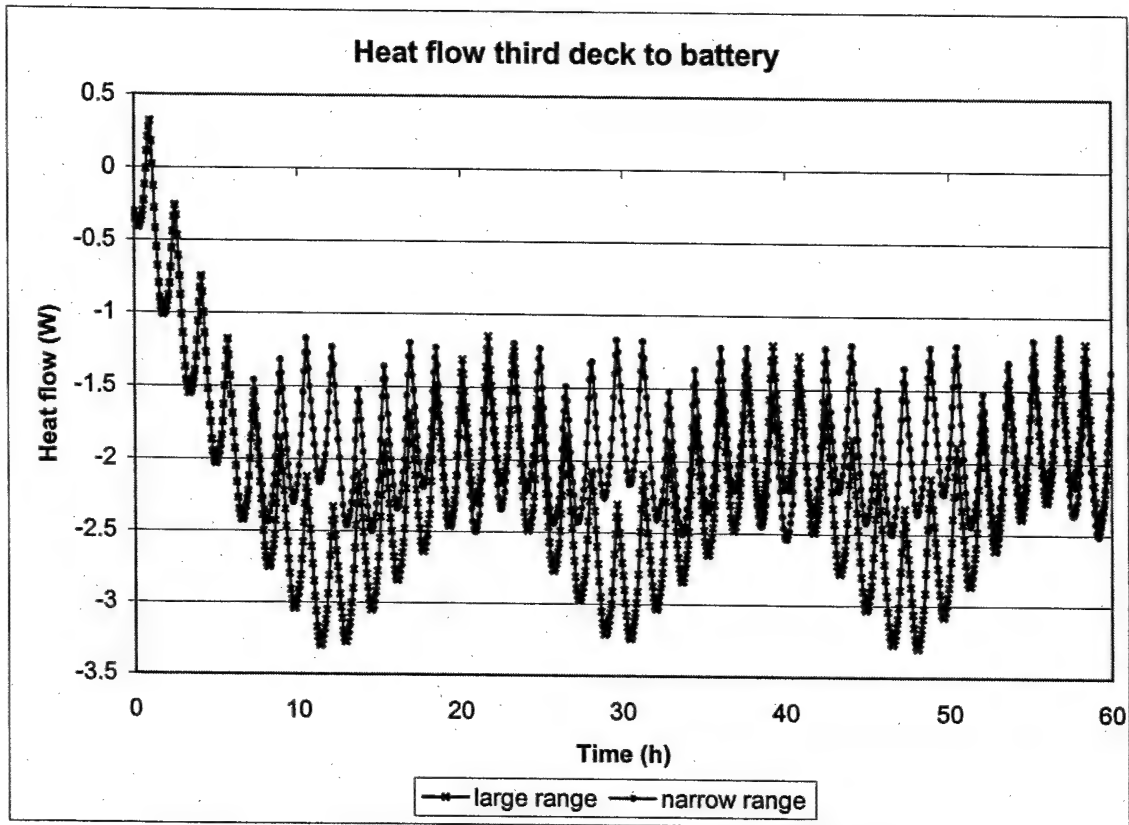


Figure 31. Heat flow structure to battery with thermostat.

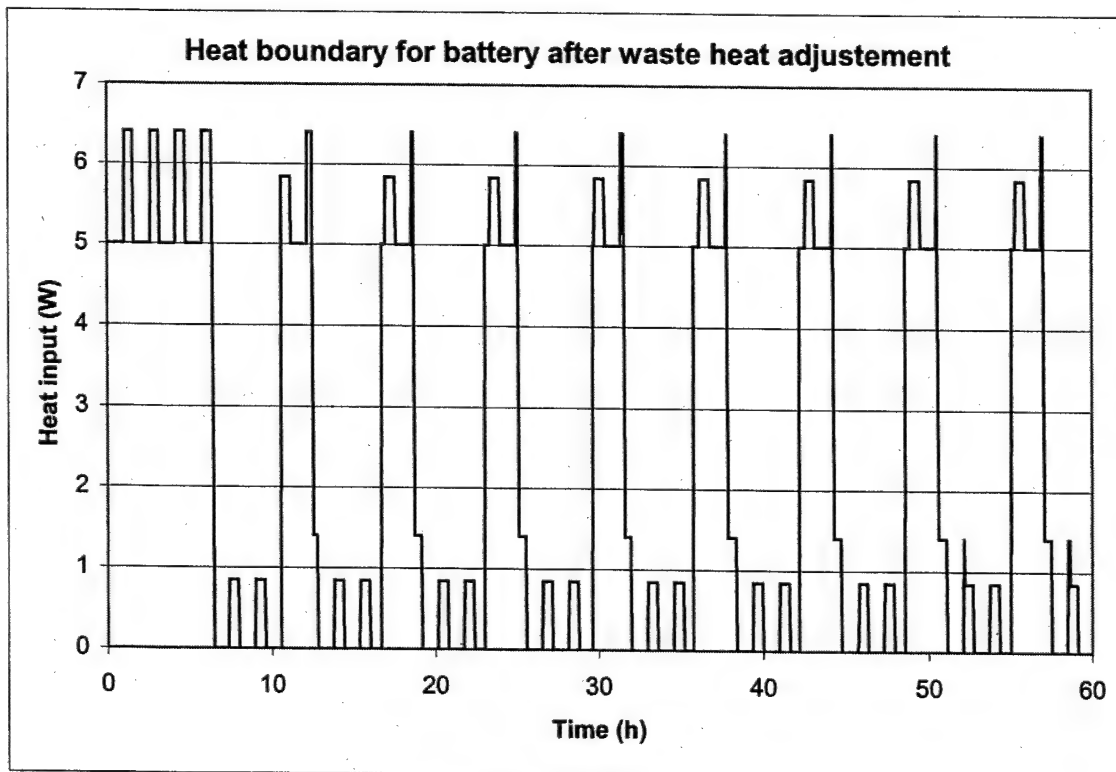


Figure 32. Duty cycle of heater and adjusted battery waste heat.

C. WORST-CASE SCENARIOS

1. Worst-case cold 1

This is the coldest case possible. It represents the checkout phase that takes place after deploy from the launch vehicle. As a worst case it can provide a closer look at safety margins, especially when compared to the next scenario. Minimum power dissipation means that just those components are turned on, that are necessary to operate the spacecraft itself. All experiments are turned off.

Power dissipation	Minimum, with cold case tables (chapter V.D.2, App K)
Surface properties	BOL
Beta angle	0 °
Start angle from local noon	246.85 °
Solar flux	$1308.2 \frac{W}{m^2}$
Earth IR	$223.2 \frac{W}{m^2}$
Albedo	25 %

Table 14. Cold case 1 parameters.

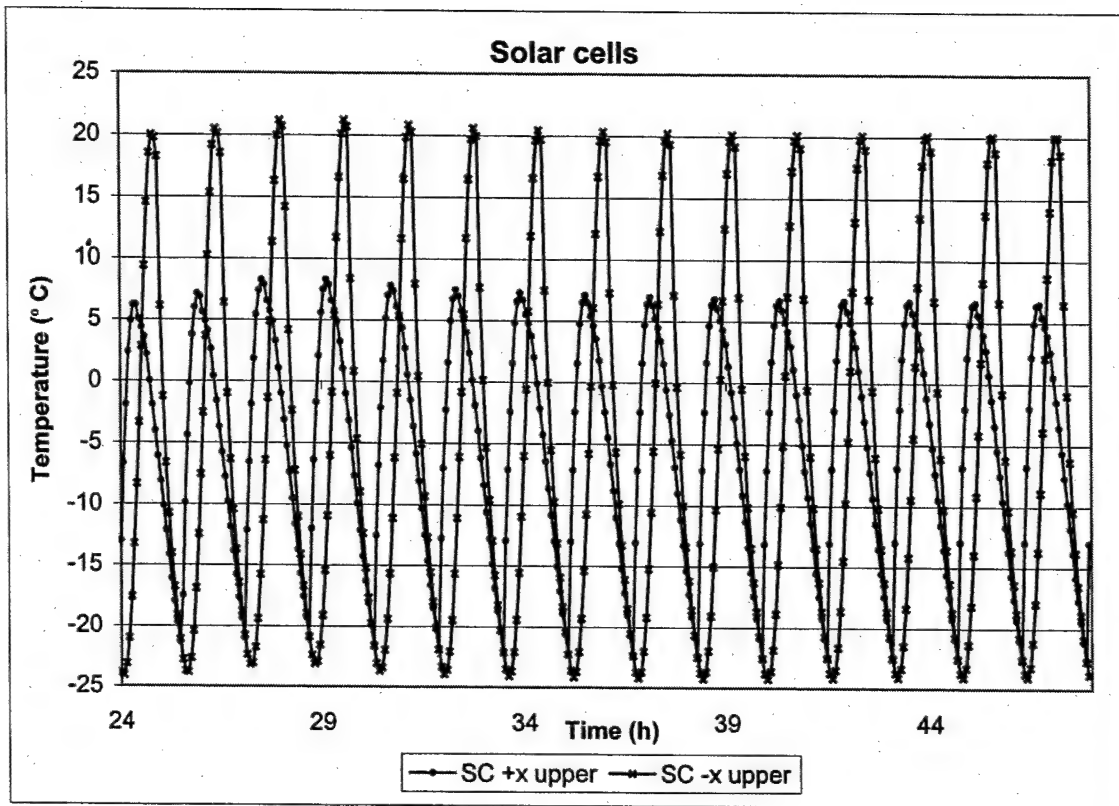


Figure 33. Solar cell temperatures of worst case 1.

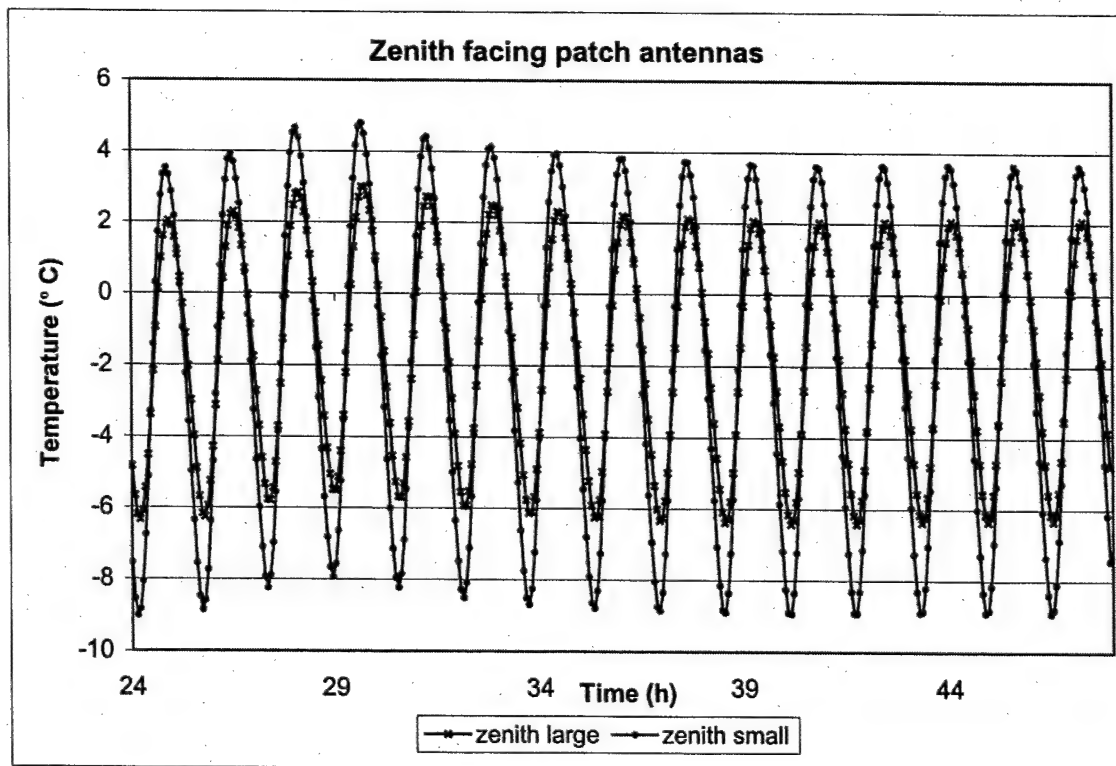


Figure 34. Patch antenna temperatures of worst case 1.

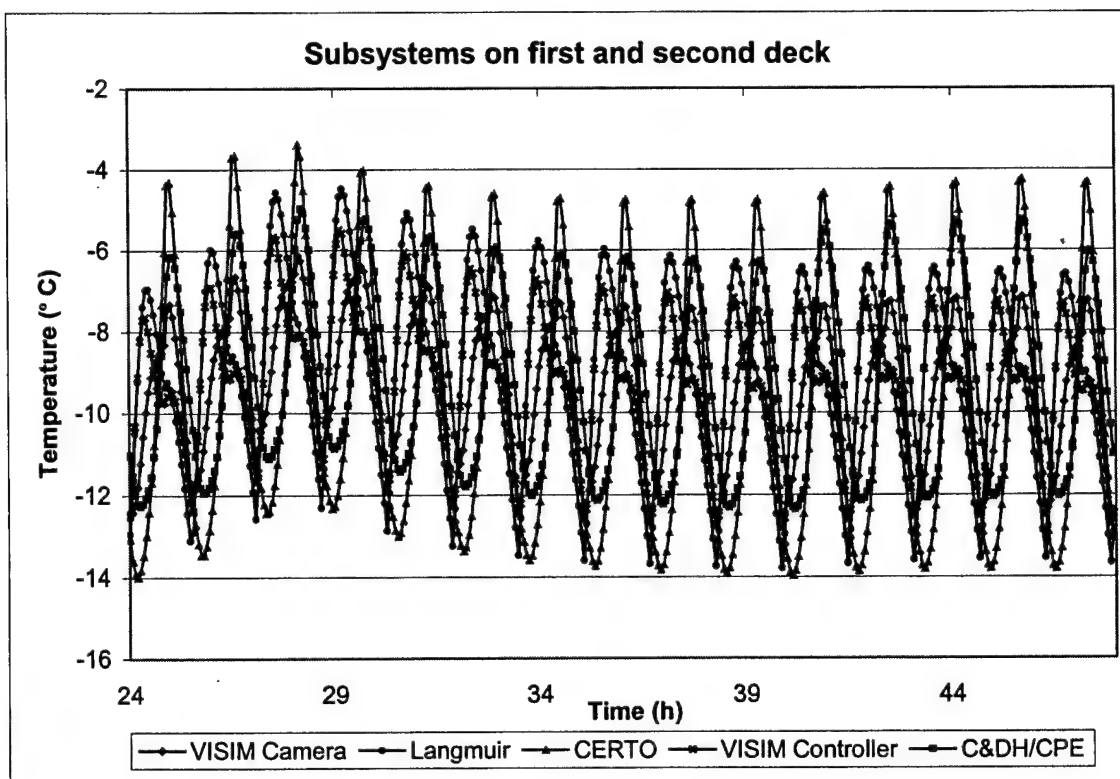


Figure 35. Subsystem temperatures on first and second deck of cold case 1.

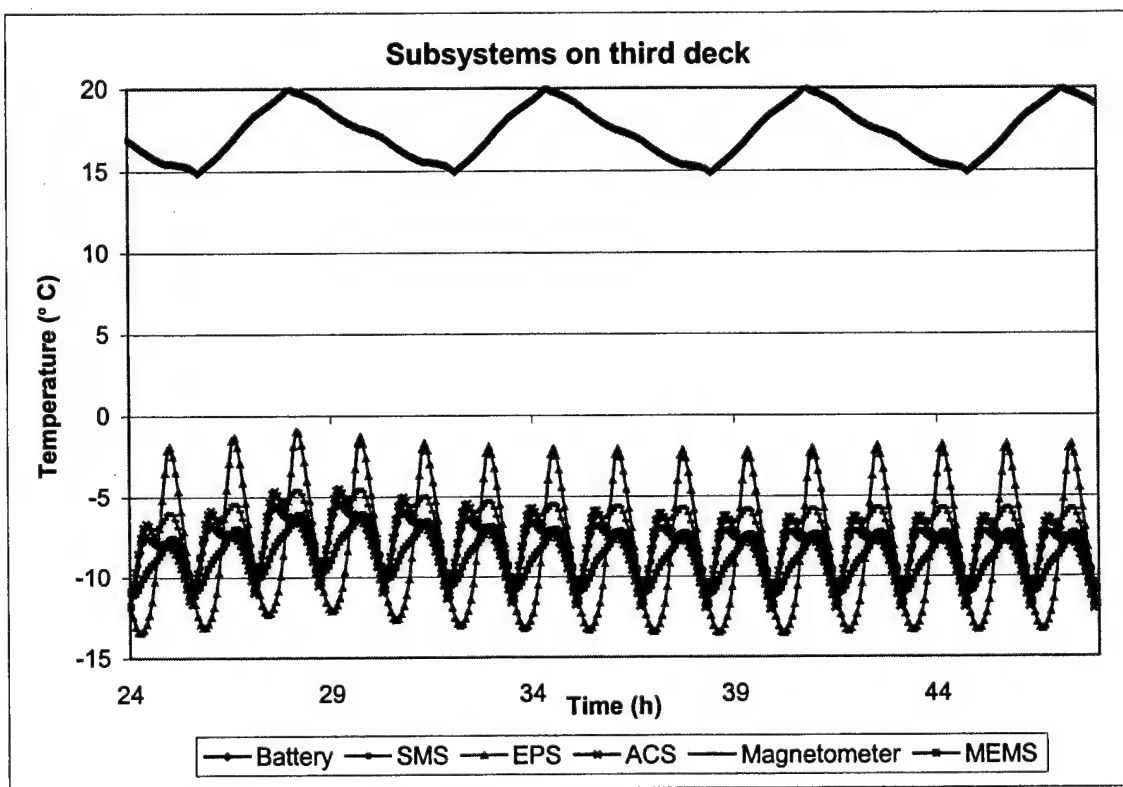


Figure 36. Subsystems on third deck of cold case 1.

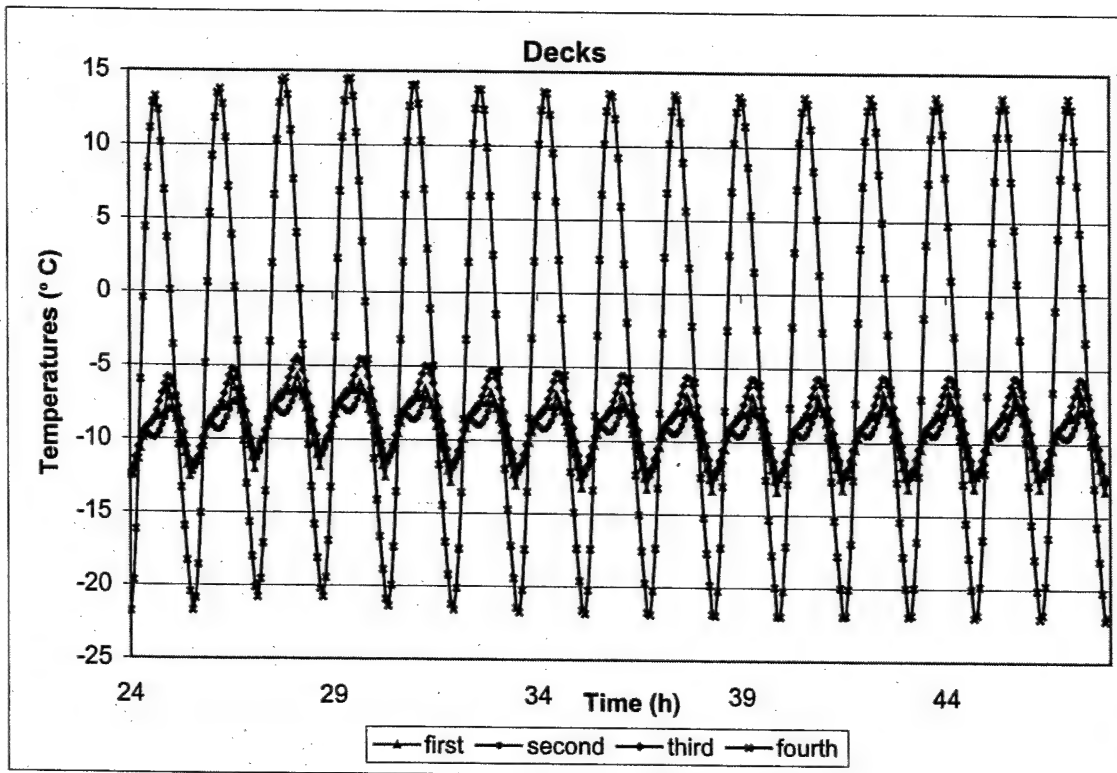


Figure 37. Deck temperatures of cold case 1.

Fig. 33 shows that the solar cells on the -x side of the spacecraft oscillate between -25°C and 22°C . This is within the limits, although there is no margin left for the lower temperatures referring to the special NPSAT1 operational limits in Tab. 3. The temperature varies about 44.9 K in 48 min. The patch antenna temperatures vary between -9°C and 5°C as it can be seen in Fig. 34. Compared to the limits for the operational state of electronic components in Tab. 3, a margin of approximately 16 K is left for the lower temperatures and a margin of 55 K for the high temperatures. But since this worst-case scenario represents a non-operational state for the experiments the margin is even higher. Compared to the solar cells, the temperature gradient is much lower: 8.5 K in 48 min. The comparatively stable temperatures of the patch antennas are due to their heavy insulation from the rest of the spacecraft.

Fig. 36 shows that at the beginning of an orbit ACS and SMS are warming up more than other devices on the third deck. This is due to their location close to the +x side of the spacecraft. SMS and ACS experience almost the same temperature changes because their thermal capacitance is very similar and their number and kind of mounting

bolts is the same. At the end of the sunlight period EPS warms up and ACS cools down. This also depends on the sun incident on the spacecraft as shown in Fig. 18. EPS faces the most extreme temperatures and has the highest temperature gradient of approximately 11.2 K in 48 min. Although EPS is modeled exactly like ACS, it gets warmer, because the other devices at the $-x$ side of the third deck are mounted with fewer and less conductive bolts. CERTO and Langmuir Probe that are not operating in this run face the coldest temperatures of approximately -14°C . But still a margin of 11 K to any limit is left. They are the devices with the most extreme temperatures although they are mounted to the comparatively thermally stable first deck. This is due to the high thermal conductivity (eight high conductive bolts). Also their thermal capacitance is only half the value of other components that are mounted in the same way. Langmuir Probe reaches its peak temperature together with the VISIM controller during the first half of the sunlight. This is due to their location close to the $+x$ side of NPSAT1, which sees the sun directly during this phase (Fig. 18). CERTO and C&DH/CPE reach their peak for the same reason during the second half of the sunlight period, because the sun is then incident on the $-x$ side, as shown in Fig. 18. The C&DH temperatures do not oscillate as much as the temperatures of EPS and ACS, although it is mounted like them, because of C&DH's high thermal capacity. The magnetometer experiences two peaks in its temperature per orbit. The first one together with ACS and the second one together with EPS, but not as high as EPS, because it is located not very close to it. MEMS is located at a similar position on the deck as the magnetometer but warms up comparatively slowly. This is due to its higher thermal capacitance. Since a thermostat controls the battery temperature, it is within the limits. Tab. 15 summarizes the results concerning the thermostat.

<i>Duty on / off (h)</i>	<i>Time heater is on (%)</i>	<i>Average consumed energy / orbit (Wh)</i>
2.33 / 4.07	36.46	2.9

Table 15. Heater power requirements of cold case 1.

The decks of the spacecraft structure have a narrower range than the components, except for the fourth deck, since this is the only deck that directly sees the sun. This deck also has the highest average temperature. Third deck has the second highest temperature,

first deck the third highest and the second deck the lowest average temperature. All temperature profiles strongly represent the influence of orbital parameters. The second deck for example shows an increasing temperature in the middle of sunlight, before it warms up again. This is due to the fact that for a beta angle of 0 ° the sun is overhead the zenith side of the spacecraft during the middle of sunlight position. That the first deck experiences almost the same stable conditions as a deck on the inside of NPSAT1 is caused by the constant Earth view of this side, that keeps the temperatures fairly stable.

2. Worst-case cold 2

This scenario represents for example a power save mode combined with the cold orbit conditions. This power safe mode might be necessary to operate if the battery energy gets less. The experiments with the lowest priority are turned off. Since the only difference to the cold case 1 scenario is that three more subsystems are operating, the subsystem temperature results are presented. Additionally, the influence of the subsystem operation on the spacecraft structure is analyzed.

<i>Power dissipation</i>	Low, with cold case tables (chapter V.D.2, App. K)
<i>Surface properties</i>	BOL
<i>Beta angle</i>	0 °
<i>Start angle from local noon</i>	246.85 °
<i>Solar flux</i>	$1308.2 \frac{W}{m^2}$
<i>Earth IR</i>	$223.2 \frac{W}{m^2}$
<i>Albedo</i>	25 %

Table 16. Cold case 2 parameters.

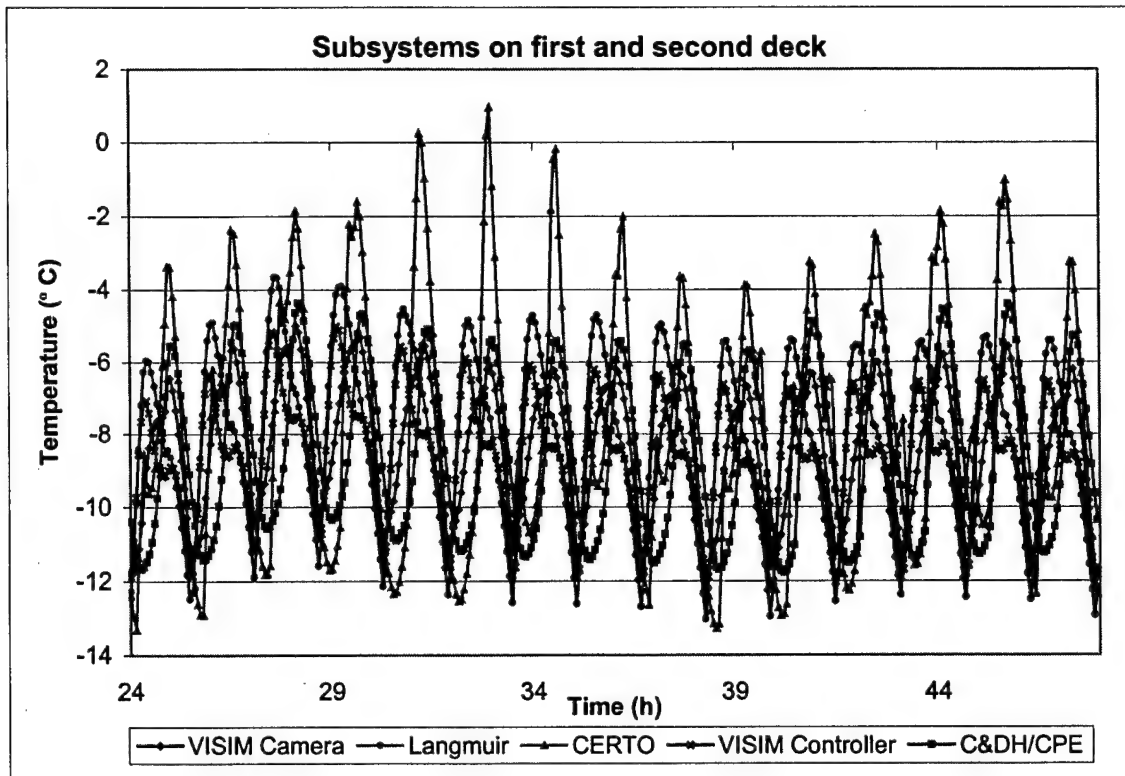


Figure 38. Subsystem temperatures on first and second deck of cold case 2.

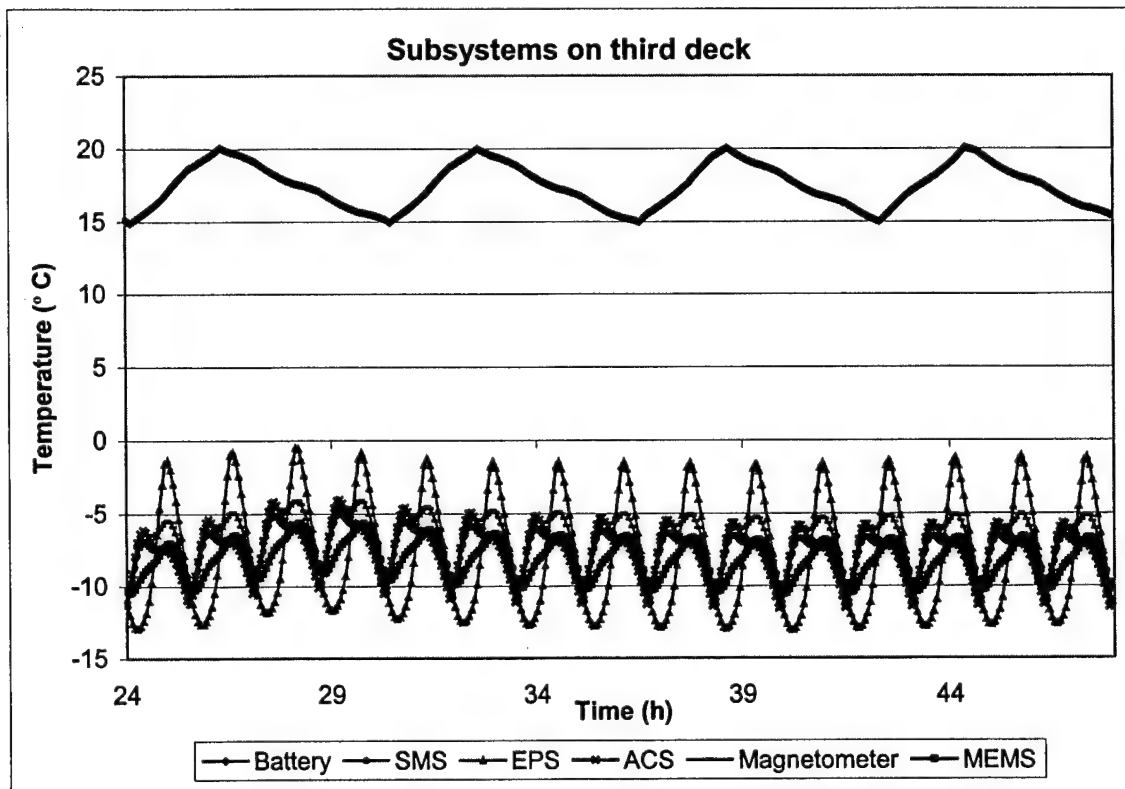


Figure 39. Subsystem temperatures on third deck of cold case 2.

As it can be seen in Fig. 38 and Fig. 39 no subsystem temperatures exceed -14°C to 2°C . Hence, they are within allowed limits. Compared to the cold case 1, it can be recognized that the shape of the CERTO temperature chart is now mainly influenced by the duty cycle. Its lowest temperature is almost the same as it was when not operating, but the maximum temperature is about 5 K higher. The change in other components, as for example the VISIM controller, is very little. This is due to the fact, that the dissipated waste heat of CERTO is about 40 times the value of the VISIM controller waste heat and the VISIM controller is turned on comparatively seldom. The SMS operation, that is turned on in this scenario has almost no influence on its temperature, since it is only on twice per orbit for a few minutes with little power.

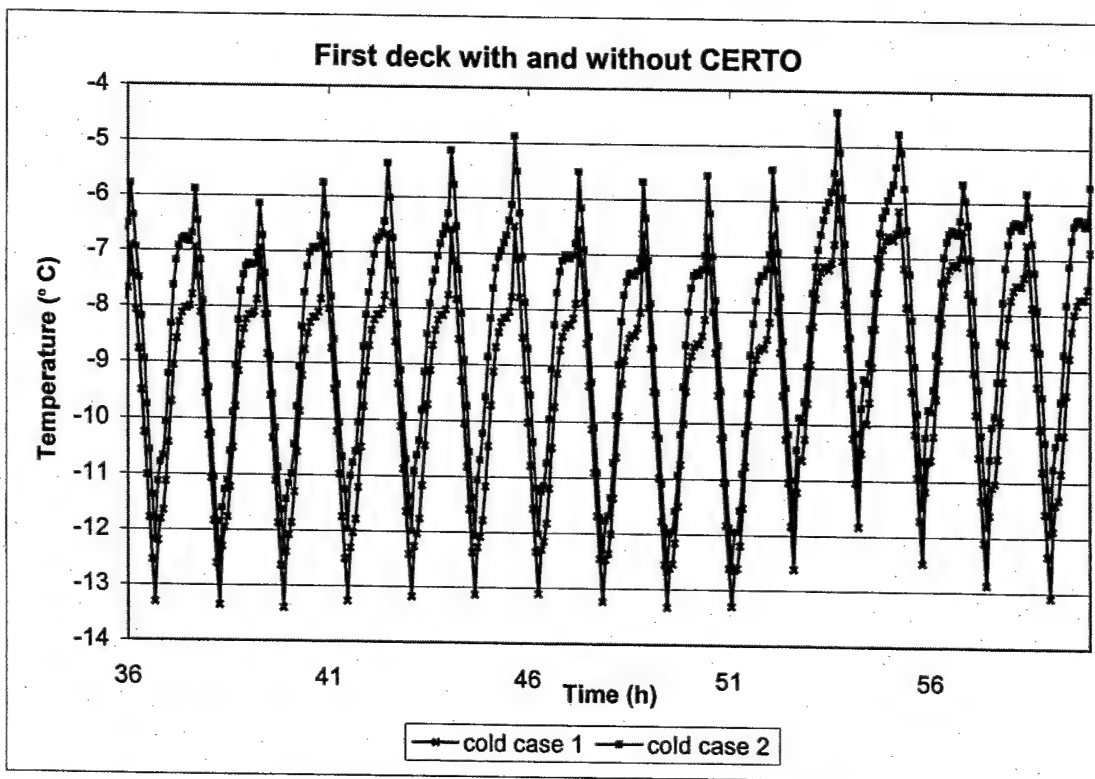


Figure 40. First deck temperatures with and without CERTO operation.

Since the only change to the last simulation run was the subsystem heat load, their influence on the rest of the spacecraft is now analyzed. Even EPS, which is still running

in the same operational state as before, is influenced: The shape of the curve is almost the same, but the average temperature is about 0.5 K higher. CERTO is the subsystem with the highest power dissipation (App. D) and without insulation between the box and the mounting deck. Therefore Fig. 40 shows the difference in the temperature of the first deck temperatures, to which CERTO is mounted, over 24 hours. The first deck temperatures are affected by the CERTO duty cycle, which can be seen from the shape of the curve in Fig. 40. But the maximum deck temperature is only 1 – 1.5 K higher than without CERTO operation. The patch antenna temperatures on the zenith side are 0.32 K higher on the average compared to the minimum operational state. The patch antennas on the nadir side are 0.7 K warmer on average. This can be obtained from the data in Ref. 25. It can be concluded that the influence of component operations on any part of the satellite is very small.

The battery power consumption is very similar to the one for the cold case 1. Parts of the difference might be due to the simulation time step. Tab. 17 shows the results.

<i>Duty on / off (h)</i>	<i>Time heater is on (%)</i>	<i>Average consumed energy / orbit (Wh)</i>
2.13 / 4.13	34.7	2.77

Table 17. Heater power requirement of cold case 2.

3. Worst-case hot 1

This scenario contains the hottest environment conditions and the lowest operational state. It can be directly compared to the worst-case cold 1 to see how the orbit conditions influence the spacecraft temperatures. Since the major change compared to the other runs is the orbit environment, but not the optical properties, the influence on the solar cells is discussed. Also the subsystem temperatures are shown, to ensure their temperatures are in the limits. A more detailed discussion of their time-phase lag is done in hot case 2.

Power dissipation	Minimum, with hot case tables (chapter V.D.2, App. K)
Surface properties	BOL
Beta angle	+ 60 °
Start angle from local noon	218.0873 °
Solar flux	$1401.2 \frac{W}{m^2}$
Earth IR	$248 \frac{W}{m^2}$
Albedo	33 %

Table 18. Hot case 1 parameters.

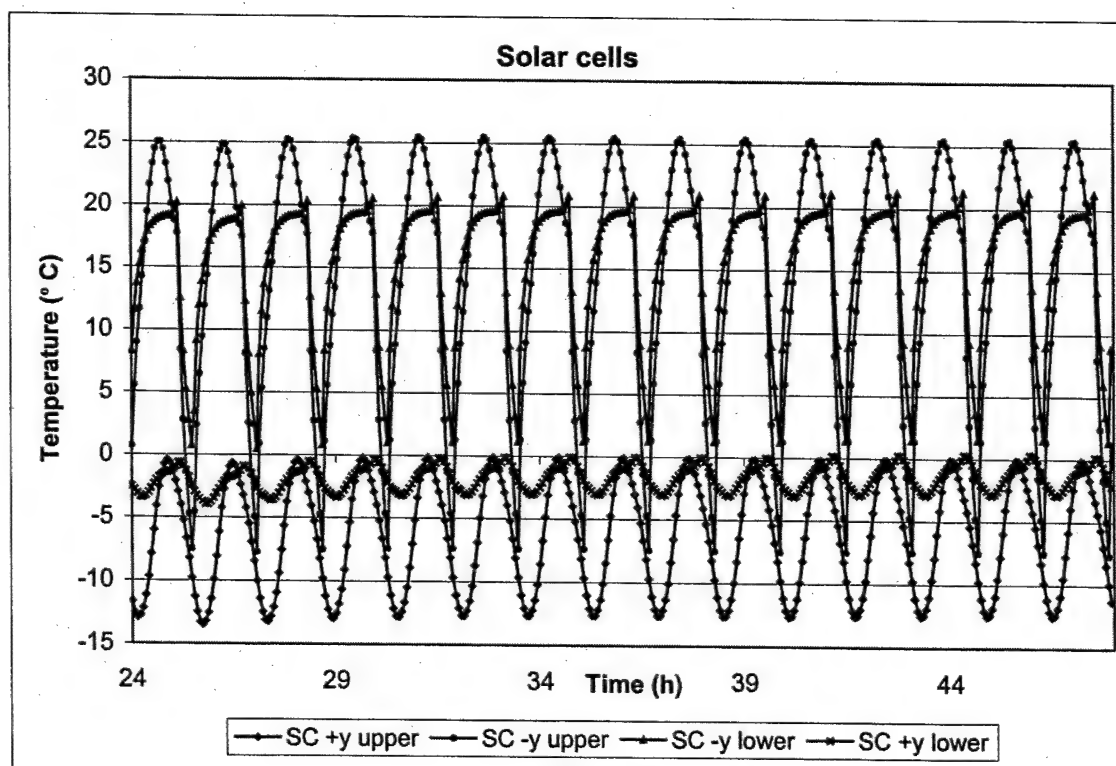


Figure 41. Solar cell temperatures of hot case 1.

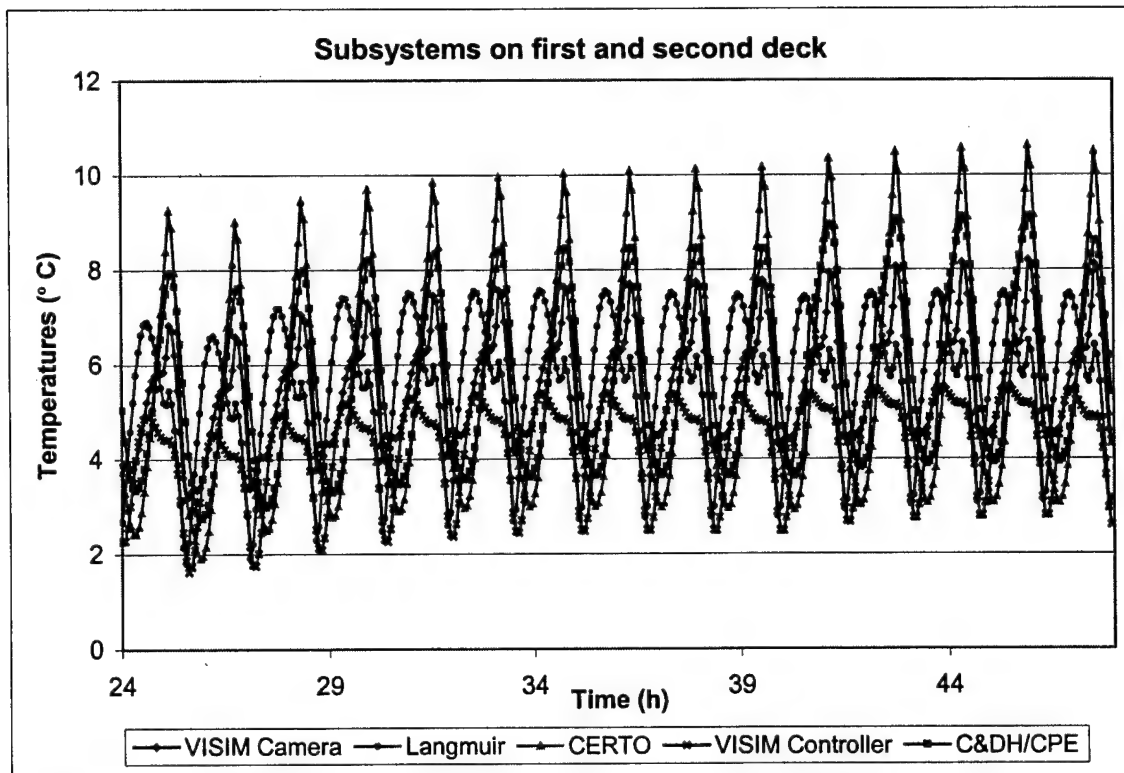


Figure 42. Subsystem temperatures on first and second deck of hot case 1.

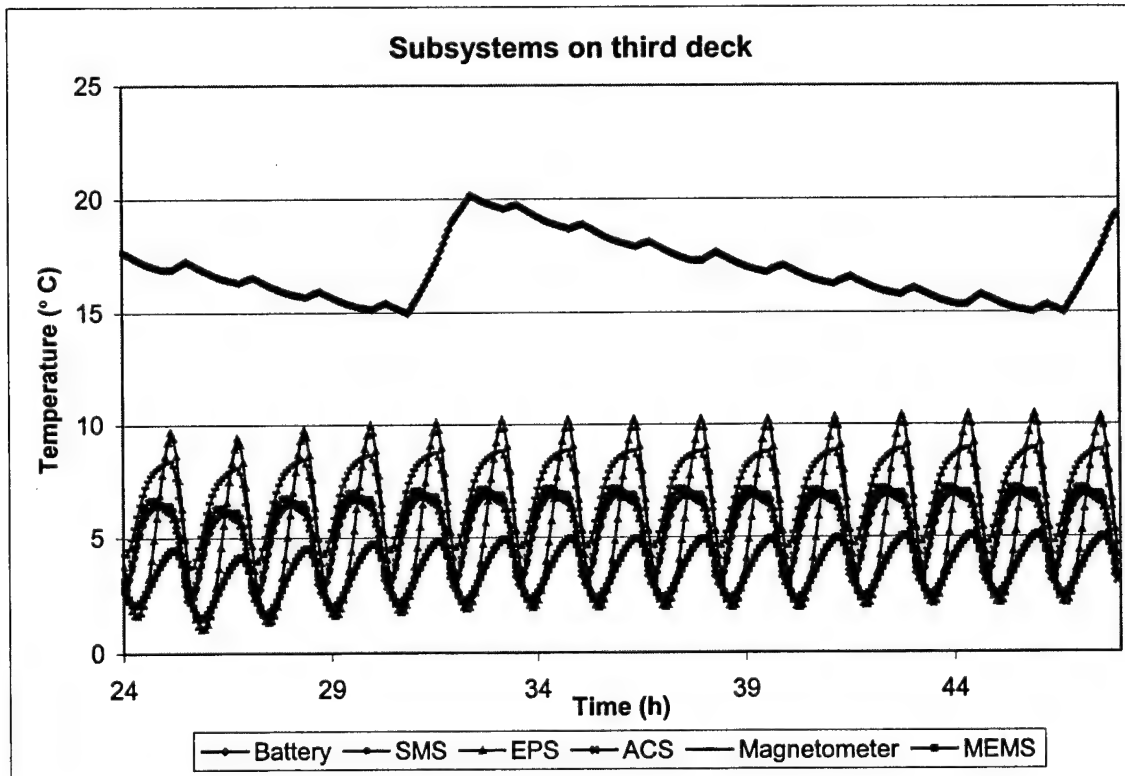


Figure 43. Subsystem temperatures on third deck of hot case 1.

The solar cells on the +y side oscillate between -14°C and 0°C , the solar cells on the -y side between -8 and 26°C as it can be seen in Fig. 41. This difference is due to the direction NPSAT1 orbits around the Earth and the three-axis stabilization. The cells next to the nadir facing side are more stable than the cells next to the zenith facing side. Therefore the cells located on the -y side next to the fourth deck experience the highest temperature gradient, which is 32.9 K during 48 min. This is approximately 12 K less than in the cold case over the same time period. Margin of at least 10 K to any limit is provided. Compared to the cold case 1 the maximum temperatures are not higher, but not that low temperatures are reached.

Comparison with the same operational state in a cold environment shows all subsystem temperatures are at a higher level than in the cold case. All temperatures are about 13 K higher than in the cold case. The maximum temperature range subsystems experience is with 8 K slightly lower than before. That thermal conditions are more stable in this orbit was already shown with the smaller temperature gradient of the solar cells. None of the components get colder than 0°C . Except for the battery, the components have a margin of 25 K to the lower temperature limit and of about 45 K to the upper limit. Heating the battery to 20°C keeps it in the desired range for a longer time. This has impact on the power that the thermostat and heater consume. The resulting values are shown in Tab. 19. It was proven that the orbital environment has a major impact on all parts of the spacecraft.

<i>Duty on / off (h)</i>	<i>Time heater is on (%)</i>	<i>Average consumed energy / orbit (Wh)</i>
1.53 / 14.27	9.7	0.775

Table 19. Heater power requirements of hot case 1.

4. Worst-case hot 2

This scenario represents the hottest conditions NPSAT1 can face. It takes degradation of the surfaces into account and therefore represents conditions after a few years on orbit. It also uses full operational mode. It is the contrary to worst-case cold 1. Therefore the same component results are examined. Compared to the hot case 1 a

statement concerning the effect of degradation over lifetime can be made. Either for the solar cells or for the black surface paint the α/ϵ ratio is higher (Tab. 9).

Power dissipation	Maximum, with hot case tables (chapter V.D.2, App. K)
Surface properties	EOL
Beta angle	+ 60 °
Start angle from local noon	218.0873 °
Solar flux	$1401.2 \frac{W}{m^2}$
Earth IR	$248 \frac{W}{m^2}$
Albedo	33 %

Table 20. Hot case 2 parameters.

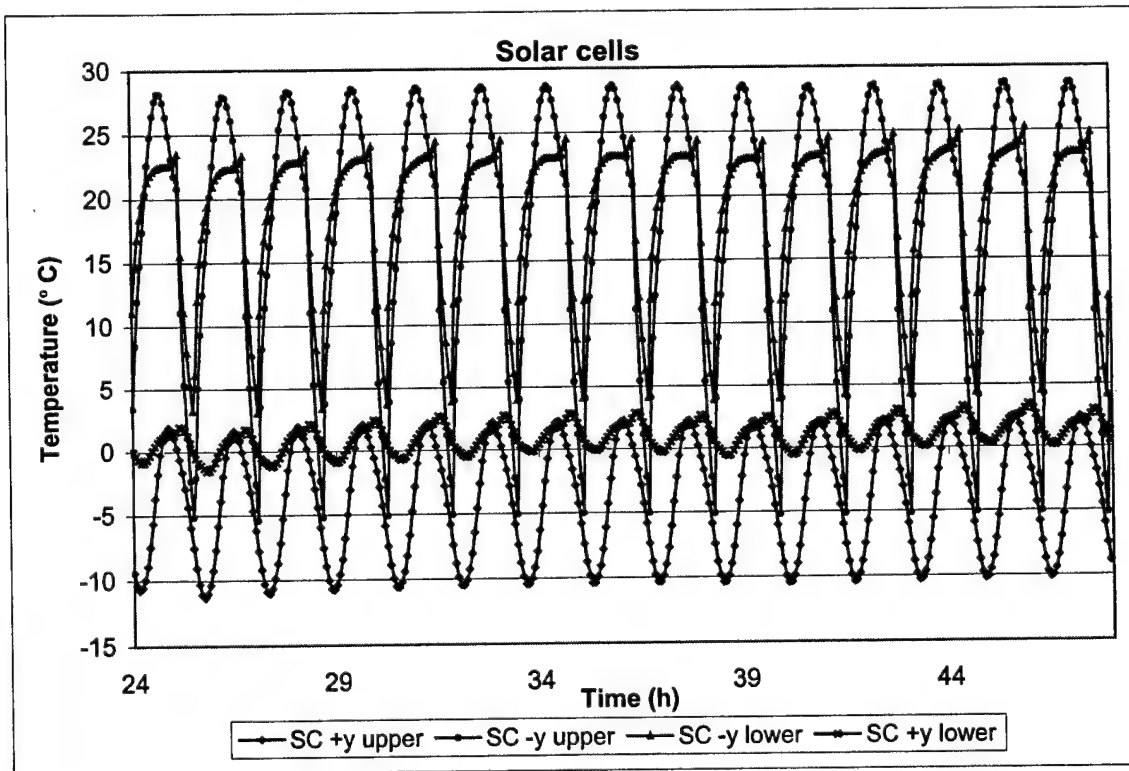


Figure 44. Solar cell temperatures of hot case 2.

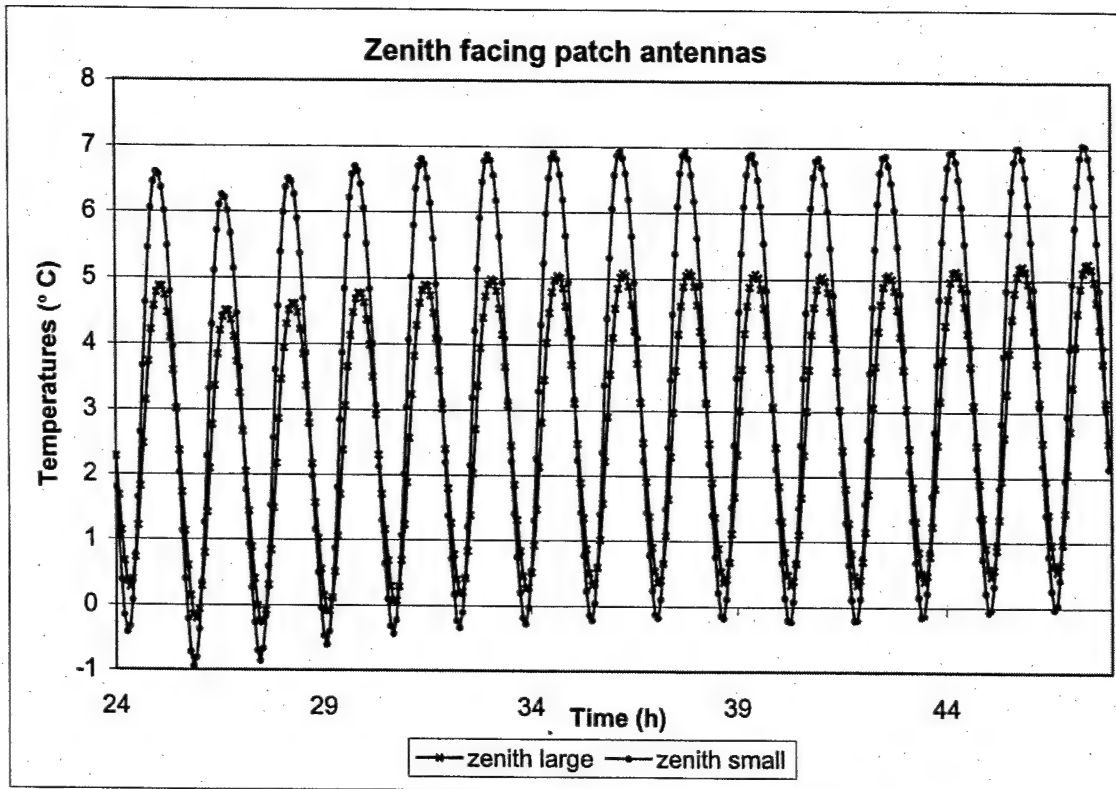


Figure 45. Patch antenna temperatures of hot case 2.

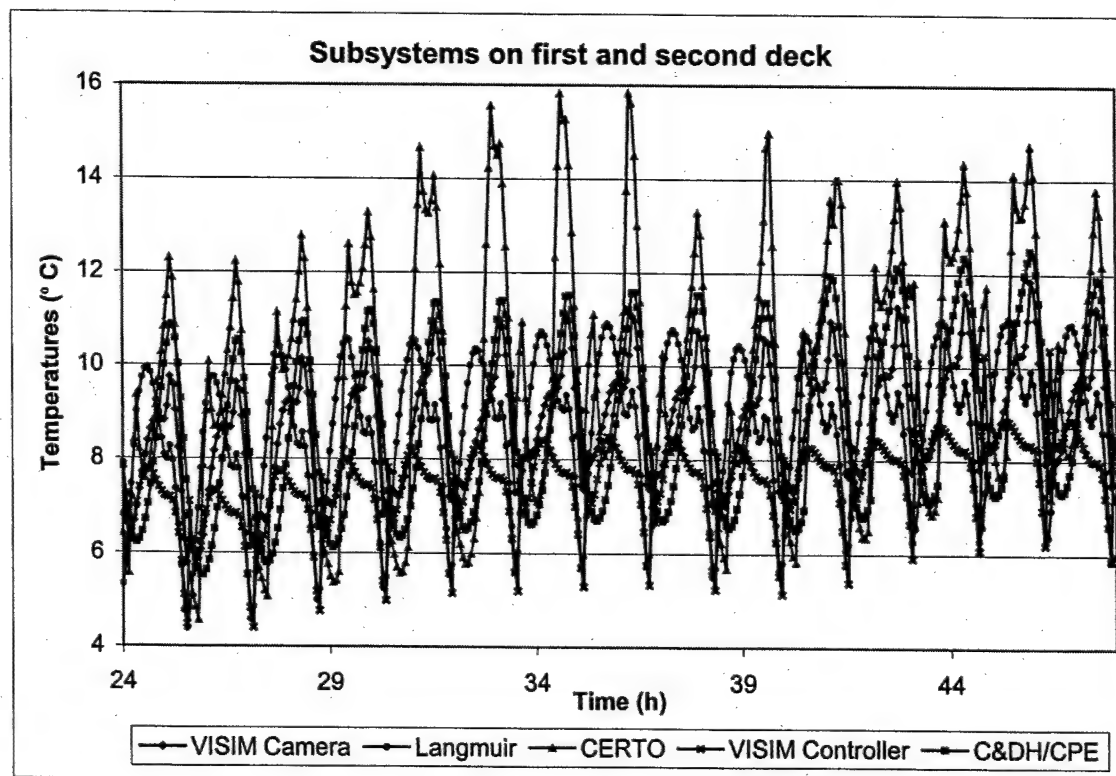


Figure 46. Subsystem temperatures on first and second deck of hot case 2.

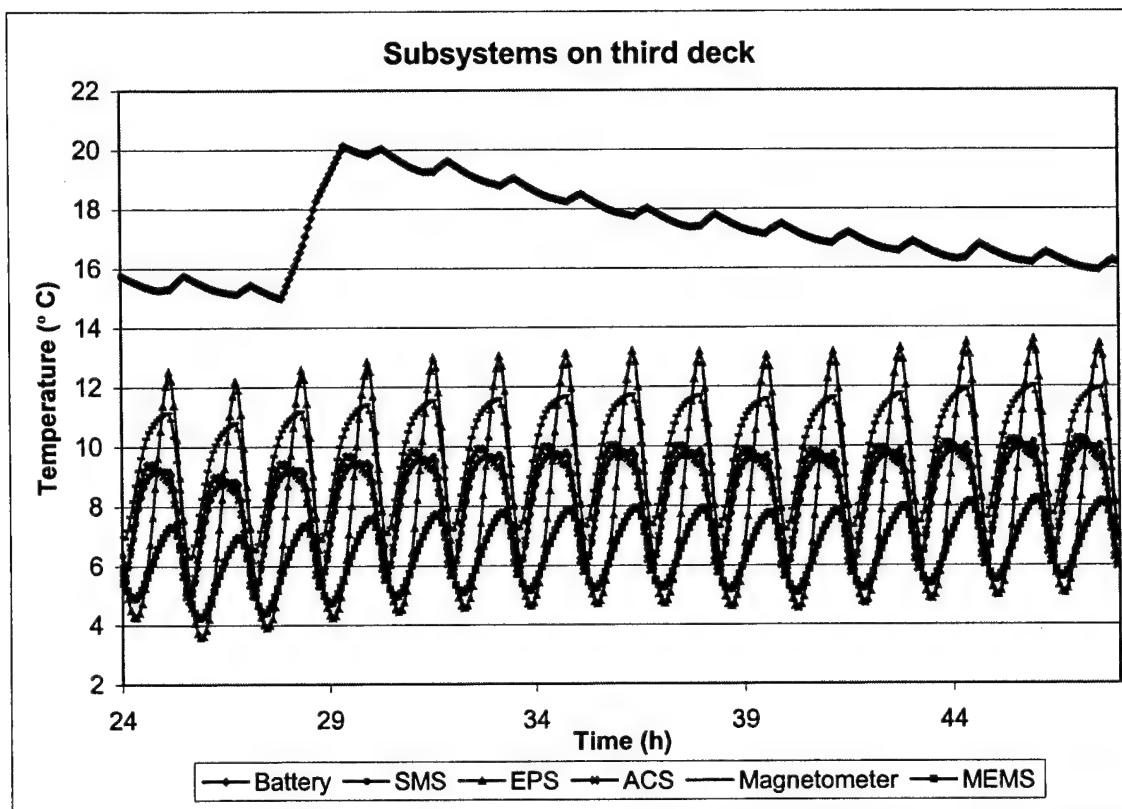


Figure 47. Subsystem temperatures on third deck of hot case 2.

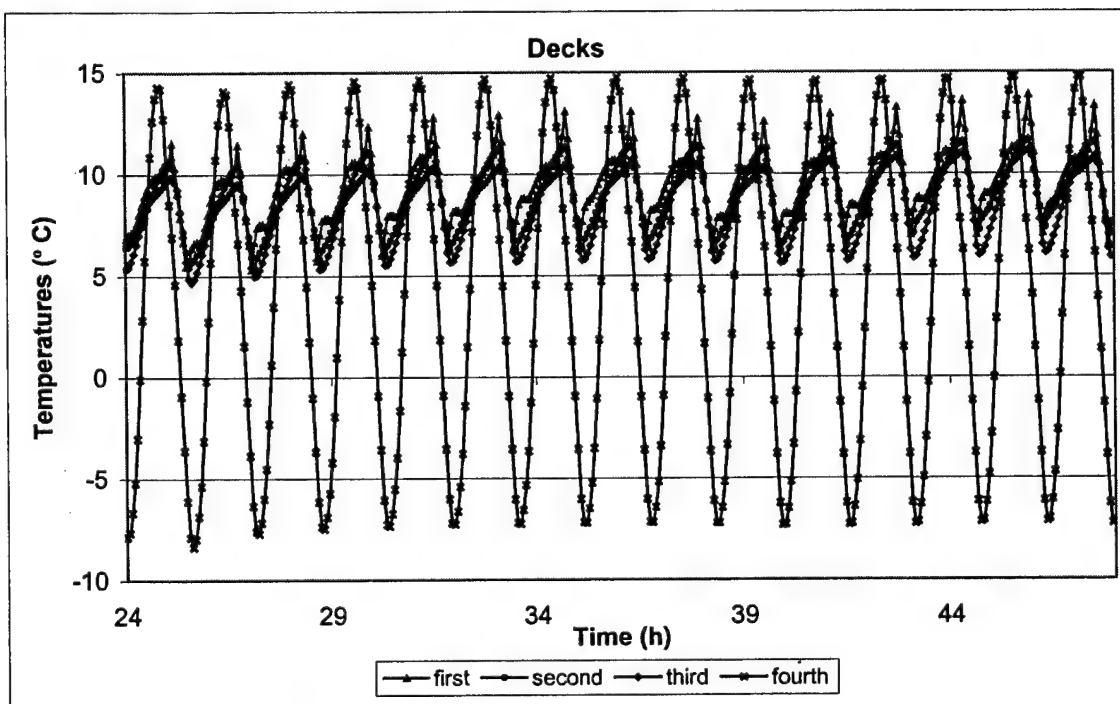


Figure 48. Deck temperatures of hot case 2.

Fig. 44 shows that the solar cells on the $-y$ side oscillate between -5°C and 29°C . This is approximately 4 K higher than in the hot case 1 with BOL conditions. The cells on the $+y$ side experience a temperature change between approximately -12°C and 3°C . This is approximately 3 K higher than in the hot case 1. As shown in cold case 2 the additionally operating components have only very little influence on the rest of the spacecraft. Therefore the largest part of the temperature change is due to the EOL optical properties of the surfaces. A more detailed analysis of the solar cell to structure connection can be obtained from chapter VII.D. The cells next to the nadir-facing side experience narrower temperature ranges than the cells next to the zenith-facing side. This can also be seen in Fig. 18. Due to the fact that in this orbital environment the $-y$ side is always sun looking and in the cold case environment $+x$ and $-x$ change between sun and space looking (Fig. 8) the temperature gradient is much lower for a hot case: 34 K in 48 min, which is approximately half the temperature difference the cells experience during the cold case simulation. The solar cells do not exceed any temperature limits and have a margin of more than 10 K to any limit.

The patch antennas in Fig. 45 oscillate from -1°C to 7°C . This is on the average 5 K higher than in the cold case. Since they are not directly looking towards the sun or dark space any more, their gradient is a little lower: 8 K in 48 min. Margin of more than 20 K is provided to any electronic component temperature limits.

Overall temperatures of the subsystems in Fig. 46 and Fig. 47 are between 4°C and 16°C . Therefore the components are overall approximately 17 K warmer than in the cold case 2. The temperatures of the VISIM controller are less increased than all other temperatures on the second and third deck compared to the cold case. This is due to the fact that all other components are located in the middle between $+y$ and $-y$ side, but the VISIM controller is more located to the $+y$ side, which is colder. The same is true for MEMS on the third deck. But it has to be taken into account, that this would be contrary in the -60° beta angle case. The highest temperature gradient is for CERTO: approximately 9.5 K during 48 min. Temperature limits are not exceeded. A margin of more than 25 K is provided in any direction.

Compared to hot case 1 it can be seen that the battery takes longer to cool down in this run, because the overall temperature of NPSAT 1 is higher in this simulation. Results for the battery duty cycle and power consumption is provided in Tab. 21. The change is significant compared to the hot case 1.

<i>Duty on / off (h)</i>	<i>Time heater is on (%)</i>	<i>Average consumed energy / orbit (Wh)</i>
1.53 / 25.47	5.7	0.46

Table 21. Heater power requirements of hot case 2.

The temperatures of the fourth deck oscillate between -8°C and 15°C . This is approximately the same highest temperature as in the cold case 1, but a 15 K higher minimum temperature. The first deck faces a temperature range of about 8 K, the other decks of approximately 6.5 K. In the cold case the first deck had the lowest minimum temperature, now it experiences the highest maximum temperature. In the cold case the first to third deck had their highest temperature under the average temperature of the fourth deck. In the hot case even the lowest temperatures are above the average of the fourth deck. This is because all deck temperatures have increased approximately 11 K, but the range of the fourth deck has decreased much more, compared to the range of the other decks.

In conclusion it was shown that NPSAT1's average temperature is higher than in the cold case. The decrease of the temperature range is less for components inside the spacecraft. The narrower temperature range is due to greater increased minima than maxima temperatures.

D. SOLAR CELL – STRUCTURE CONNECTION

From the cold case it was learned that the space environment has by far the strongest influence on the spacecraft temperatures. Since the solar cells are a subsystem and also the direct interface between NPSAT1 and space, they are analyzed in further detail in this chapter. The main question was how the solar cells behave compared to the structure to which they are mounted. This provides information about the conductivity

between them. This is not trivial, since it consists of two different heat transfer modes. Per panel side all nine elements exchange radiation between the solar cells and the structural panel over a very short distance (0.05 mm) and eight bolted joints are used for mounting. To get comparable results only the beta angle was changed between the hot and the cold case. Other conditions were BOL optical properties, full operational subsystem mode and default orbital parameters (Tab. 10).

For the cold case analysis the post processed elements are taken from the column of panel sides next to the $-x$ edge (trailing-edge) in $+y$ direction. For the hot case they are taken from the column of panel sides next to the $-y$ edge in $-x$ direction. Per panel side the center element was chosen, since it has no physical connection to the other part of the spacecraft. Thus, the temperature difference can be obtained more precise, because the other elements per side panel model a contact conductance which takes only place at a very small part of the area that is modeled by a FE. Fig 49 shows these elements. On the structural panel an equivalent for each element on the solar cell panel exists.

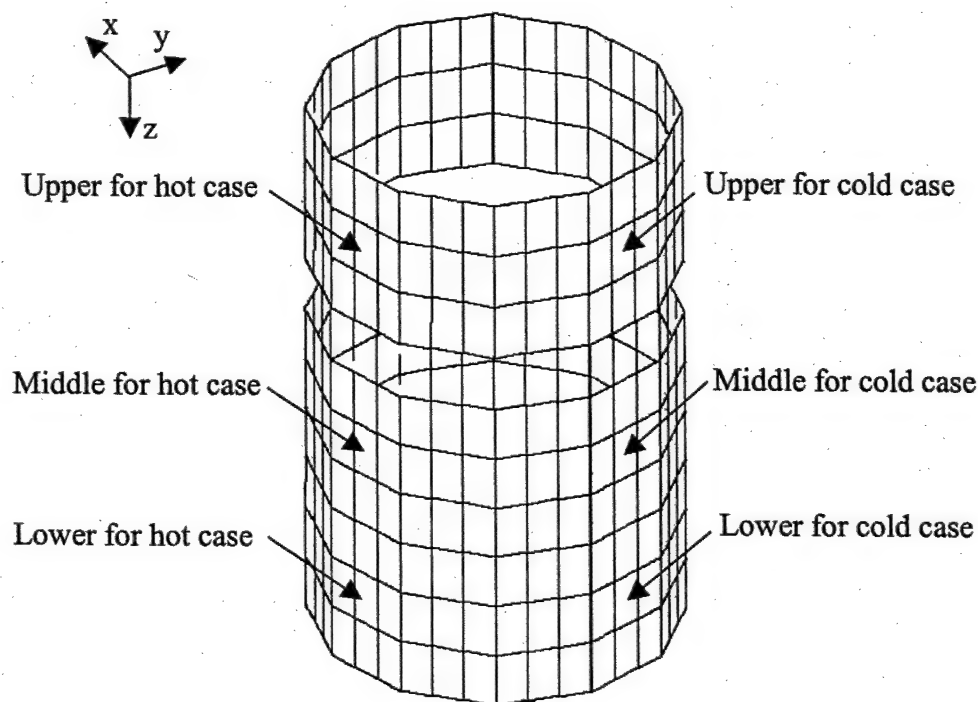


Figure 49. Post-processed elements in solar cell – structure analysis.

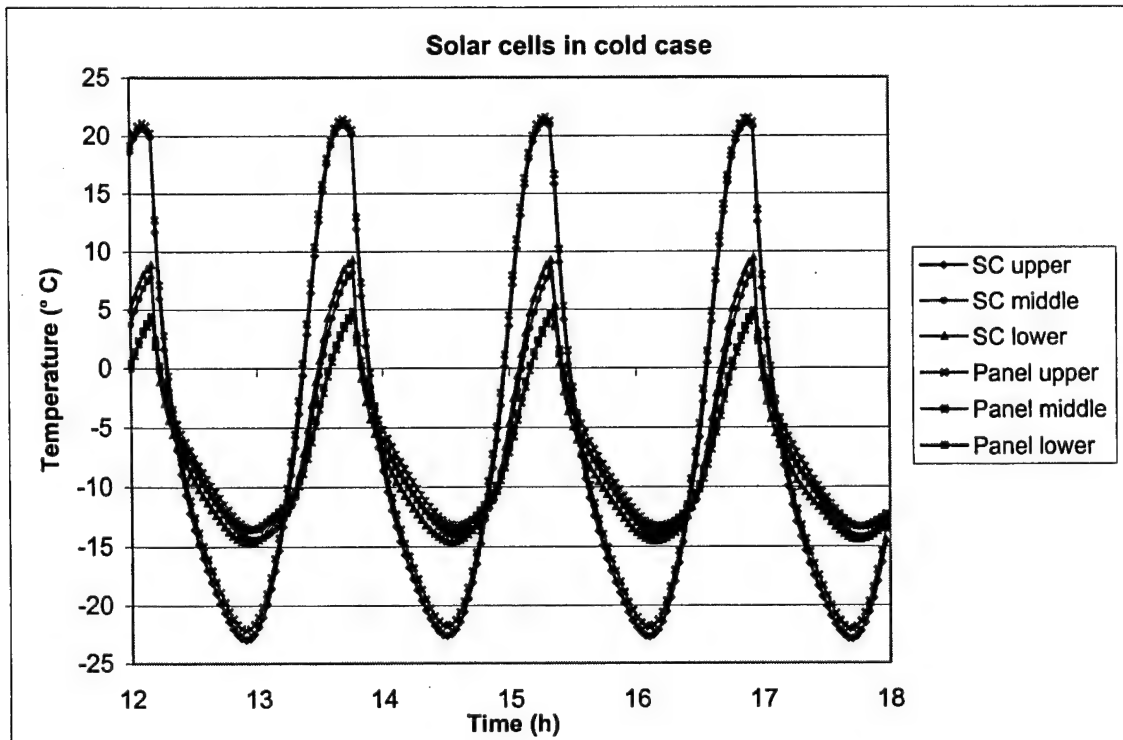


Figure 50. Solar cells and structural panels in cold case.

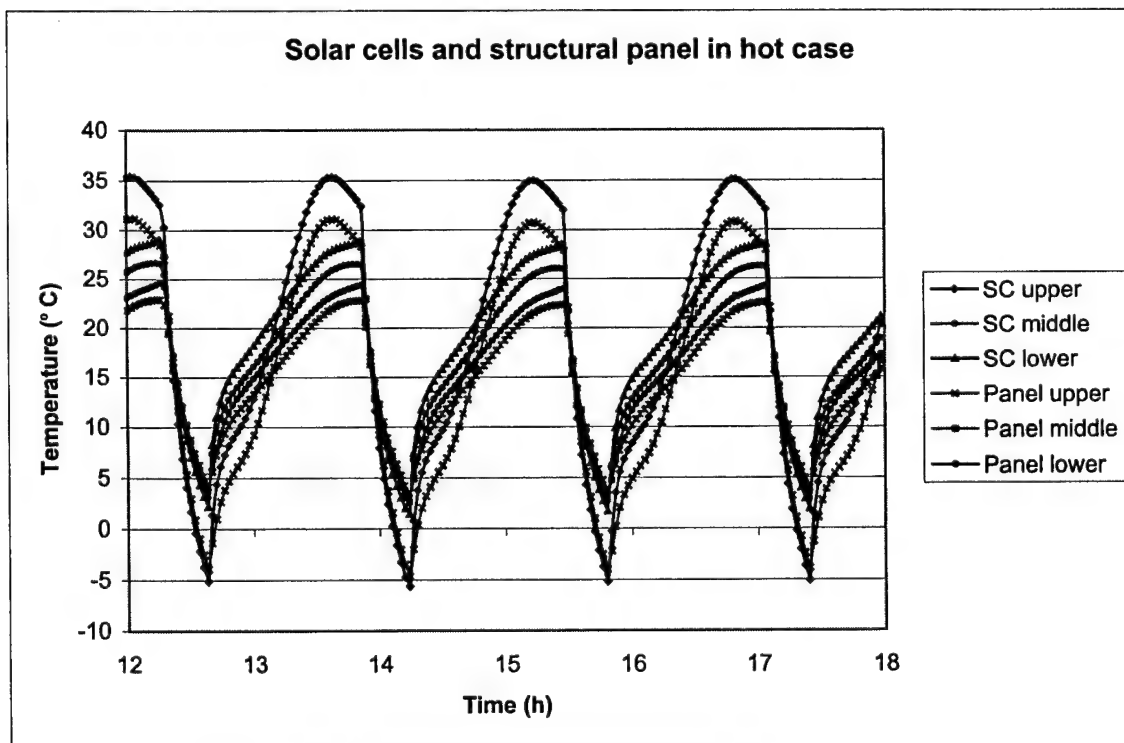


Figure 51. Solar cells and structural panel in hot case.

As mentioned previously the cells on the upper panel face the highest temperature changes. The temperatures of the middle (experimental cells) and the lower panel (commercial cells) are very similar, although they are not directly connected to each other. The panels have all temperatures very similar to the solar cells. The time delay between the heating of a solar cell and the heating of the panel to which it is mounted is very small in the cold case. Due to the simulation time step (120 s) often no delay is visible. For the hot case this time delay increases more with higher temperatures. The temperature difference between the lower and the middle panel is also larger for higher temperatures in the hot case. The temperature difference between solar cells and the associated structural panel is less than 1 K for the cold case, and between 0 K and almost 5 K for the hot case.

A material to improve heat flow from the cells to the structure would only be effective for the high temperatures of the hot cases.

THIS PAGE INTENTIONALLY LEFT BLANK

VIII. CONCLUSION AND RECOMMENDATIONS

A thermal model of NPSAT1 was successfully developed. The results fit the orbital parameters in all scenarios, down to the component behavior, indicating agreement with expected results. Temperature-time histories for all major parts of NPSAT1 are provided. Design changes were made to the interface of the battery, to the mounting deck, and to the optical surface properties. Furthermore a thermostat-controlled heater was added and its operation parameters determined. Sensitivity information can be obtained, because every design change was approached with different designs. Hot and cold case scenarios were performed with the changed design. Since the changes were made with specific materials instead of arbitrary values, the results can be taken as direct recommendations to changes to the real design of NPSAT1.

It was shown, that the hot case orbital parameters provide the best environment for NPSAT1. Taking the design changes into account the cold case is also not critical, but close to some limits. It was proven that the design changes are sufficient to maintain all subsystems within their temperature requirements.

The usefulness of an additional material to increase the heat flow between the solar cells and the structural panel might be very small, since temperatures of solar cells and panels are almost equal during most time on orbit.

If for certain reasons design changes will not be made as recommended, the developed model offers the possibility of alterations to analyze changes. The provided sensitivity information can help to choose materials.

Information about the influence of the location of components can also be obtained from this simulation. The location of the battery was proven to be useful. Mounting it more to the +y or -y side would increase the temperature for the positive or negative beta angle, but decrease it for the contrary case.

Since the battery is of special concern, it is strongly recommended to develop and analyze a detailed thermal model of NPSAT1's battery. This thesis provides input information for a simulation of a detailed battery model. Since the meshing was done

with respect to the mounting bolts a battery model can also be attached to the thermal model of the spacecraft and simulated as one part.

Assumptions were made for some parameters that are not defined yet (number of mounting bolts, thermal capacitances). Once these are defined the changes should be implemented into the model and simulations should be performed again. Therefore this thesis can provide direction for setting up the simulation runs.

Tests are recommended to be able to replace assumptions in the model. Especially the temperature-sensitive electronic components should be tested. In particular the battery is of interest, since its design is totally different from any other electronic subsystem.

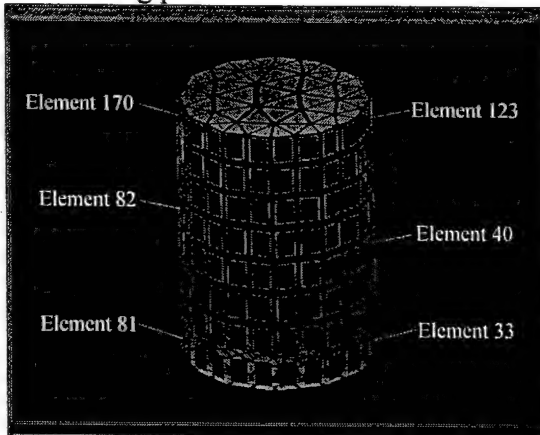
APPENDIX A. PRELIMINARY THERMAL ANALYSIS RESULTS

This appendix presents selected results of a preliminary thermal analysis, performed by the Space Systems Academic Group. Shown are a summary of the constraints and the most extreme results for the x and y sides.

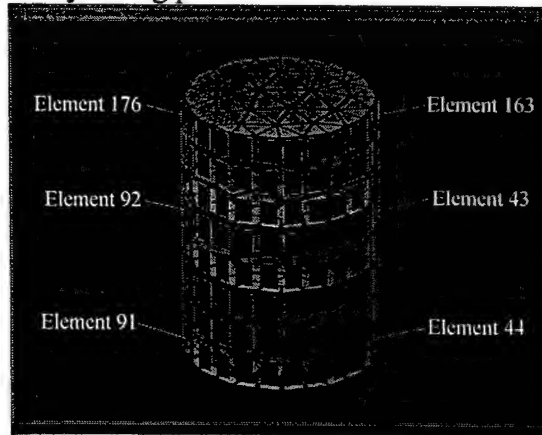
- Finite Element Model:
 - Only structure modeled (no housings)
 - All material: AL-6061-T6: Density: $2.7658 \times 10^3 \text{ kg/m}^3$
Thermal Conductivity: $1.6788 \times 10^2 \text{ J/m/K/s}$
Specific Heat: $9.6296 \times 10^2 \text{ J/kg/K}$
 - Four equipment plates (gold anodized): Emissivity: 0.82
Absorptivity: 0.48
 - Solar panels on cylinder sides: emissivity: 0.85
absorptivity: 0.79
- Orbital parameters: 550 km, circular orbit, beat angle 0°
- Heat input: constant heat input of 31.5 W, distributed over three lower equipment plates, 8 W on upper-mid, 10 W on lower-mid, 13.5 W on base-plate
- Transient analysis: duration 0.5 days, results output: 120 s

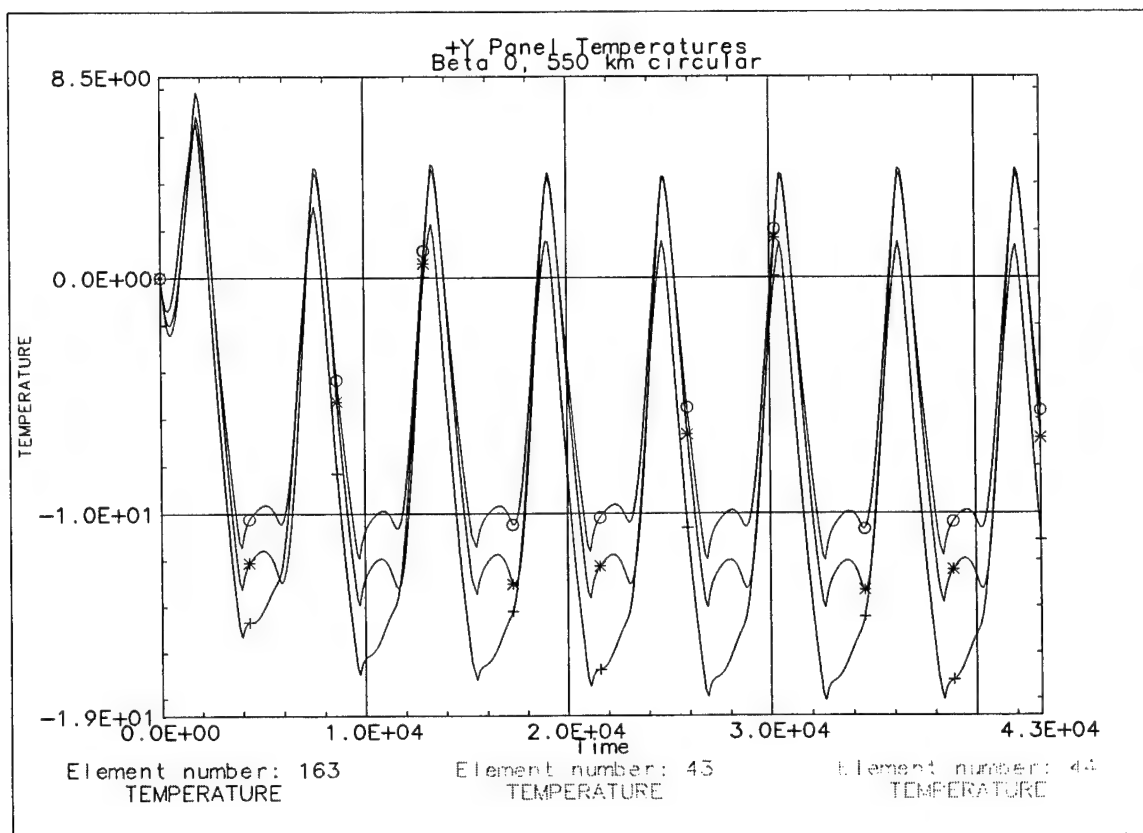
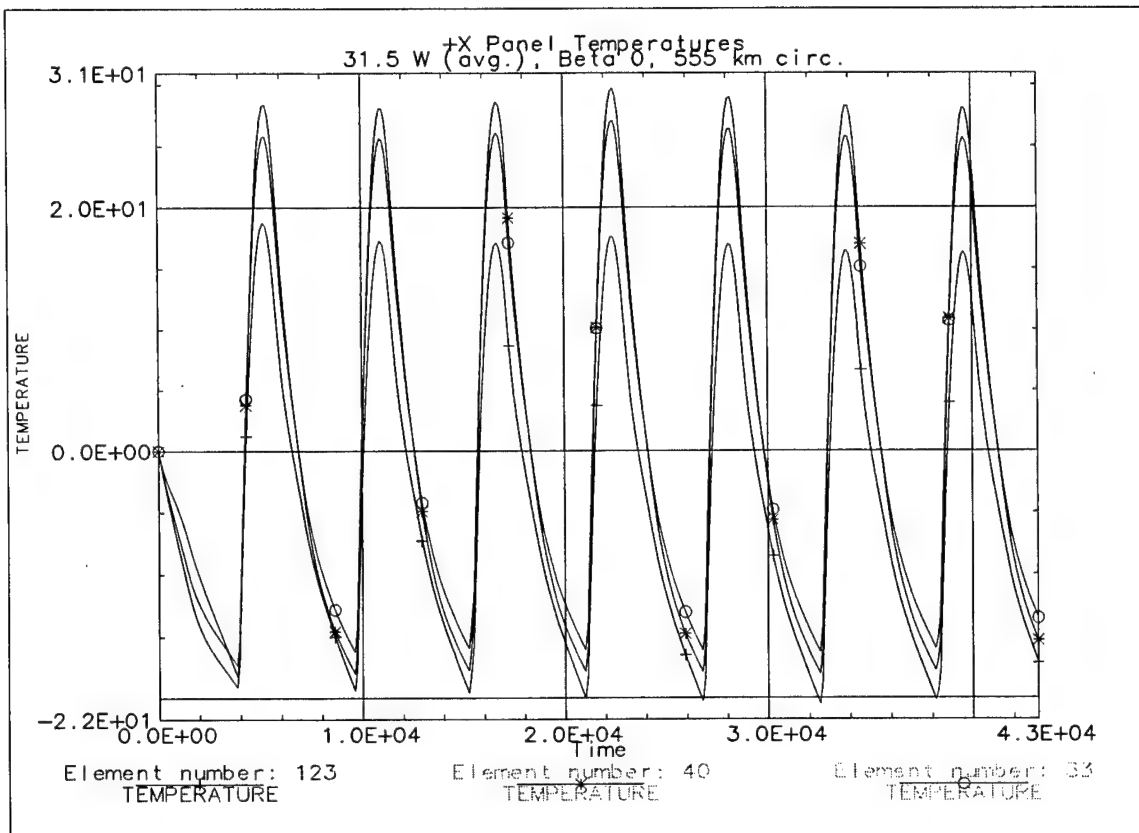
Post-processed elements:

+/- x facing panels



+/- y facing panels

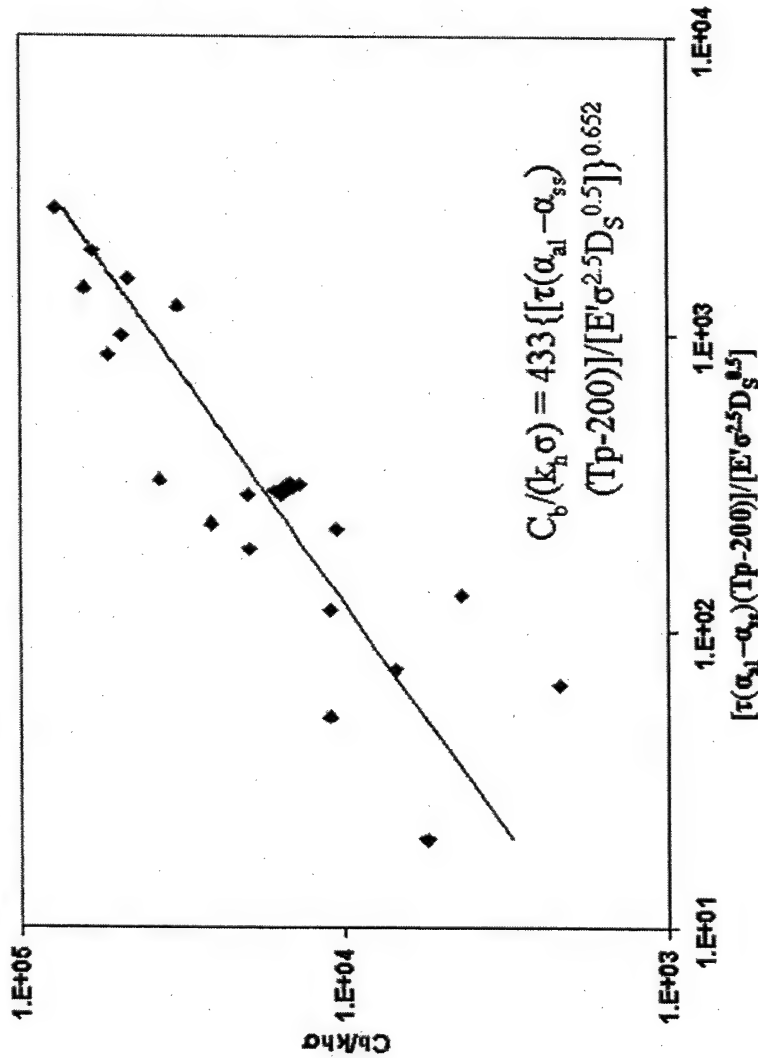




APPENDIX B. EQUATION CORRECTION FROM GLUCK

This appendix provides the corrected equation 8.20 on p. 267 in Ref. 5. It is here reprinted by permission from Ref. 6. This equation is equation III.17 in this thesis.

Bolted Joint Conductance: New Correlation



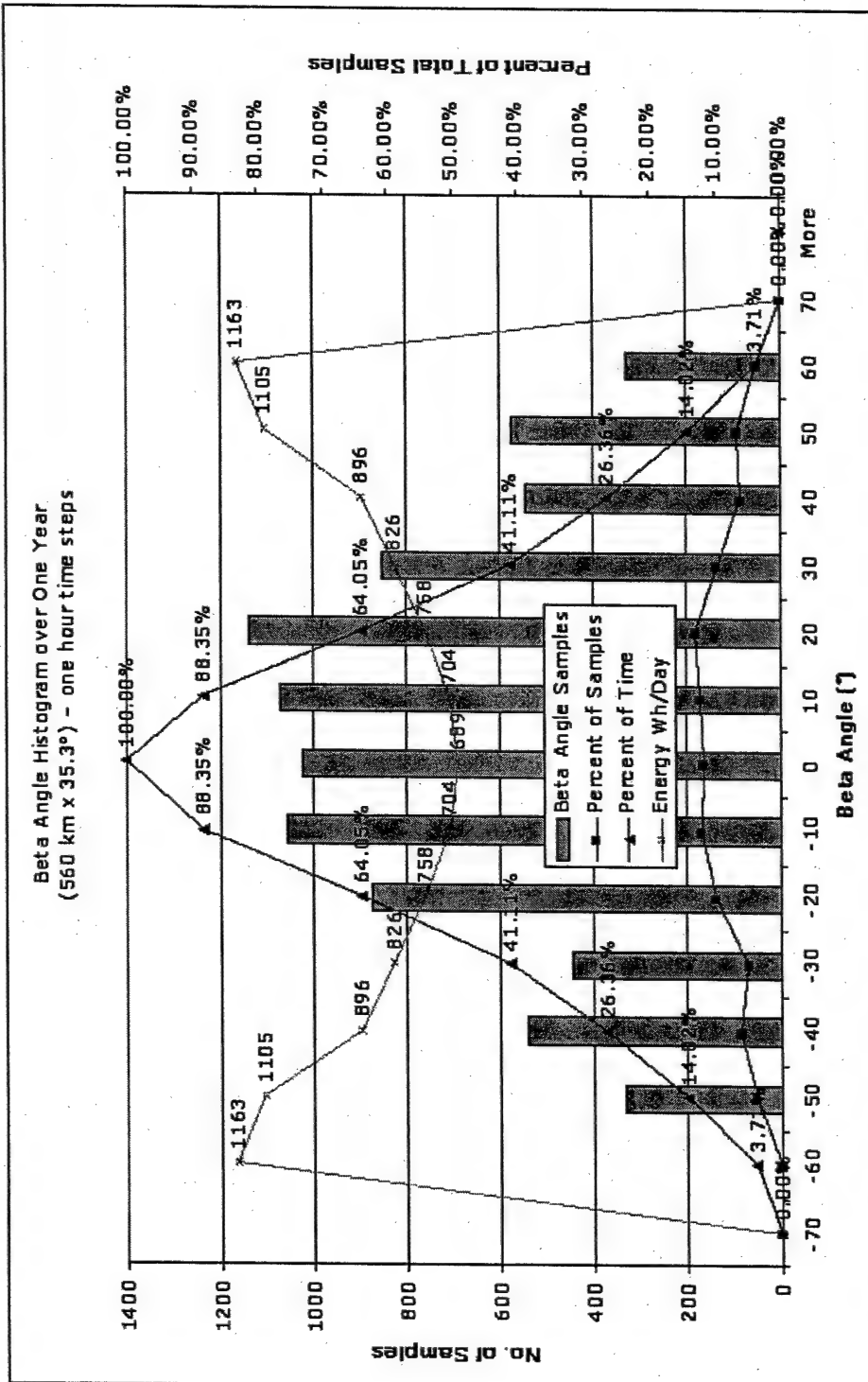
Range of Test Parameters

	Bolt Size - Threads per Inch	Bolt Shaft Diam., mm	Torque, m-N	Plate Thickness, mm	Roughness, σ , m	Flatness, TIR, m	Plate Temp., K	Conductance, W/K
Minimum	6-32	3.51	0.34	1.02	6.26E-07	1.02E-05	292.4	0.41
Maximum	1/4-20	6.35	9.39	12.7	2.26E-06	1.27E-04	400.4	13.8

THIS PAGE INTENTIONALLY LEFT BLANK

APPENDIX C. BETA ANGLE HISTOGRAM

This appendix provides the beta angle histogram. [Ref. 17]



THIS PAGE INTENTIONALLY LEFT BLANK

APPENDIX D. POWER BUDGET

This appendix presents a power budget provided by the Space Systems Academic Group. It was used as basis for duty cycle calculations. For high frequency devices the values in the "average" columns were used. For the low frequency devices the value in the "maximum" column was used in combination with developed duty cycles.

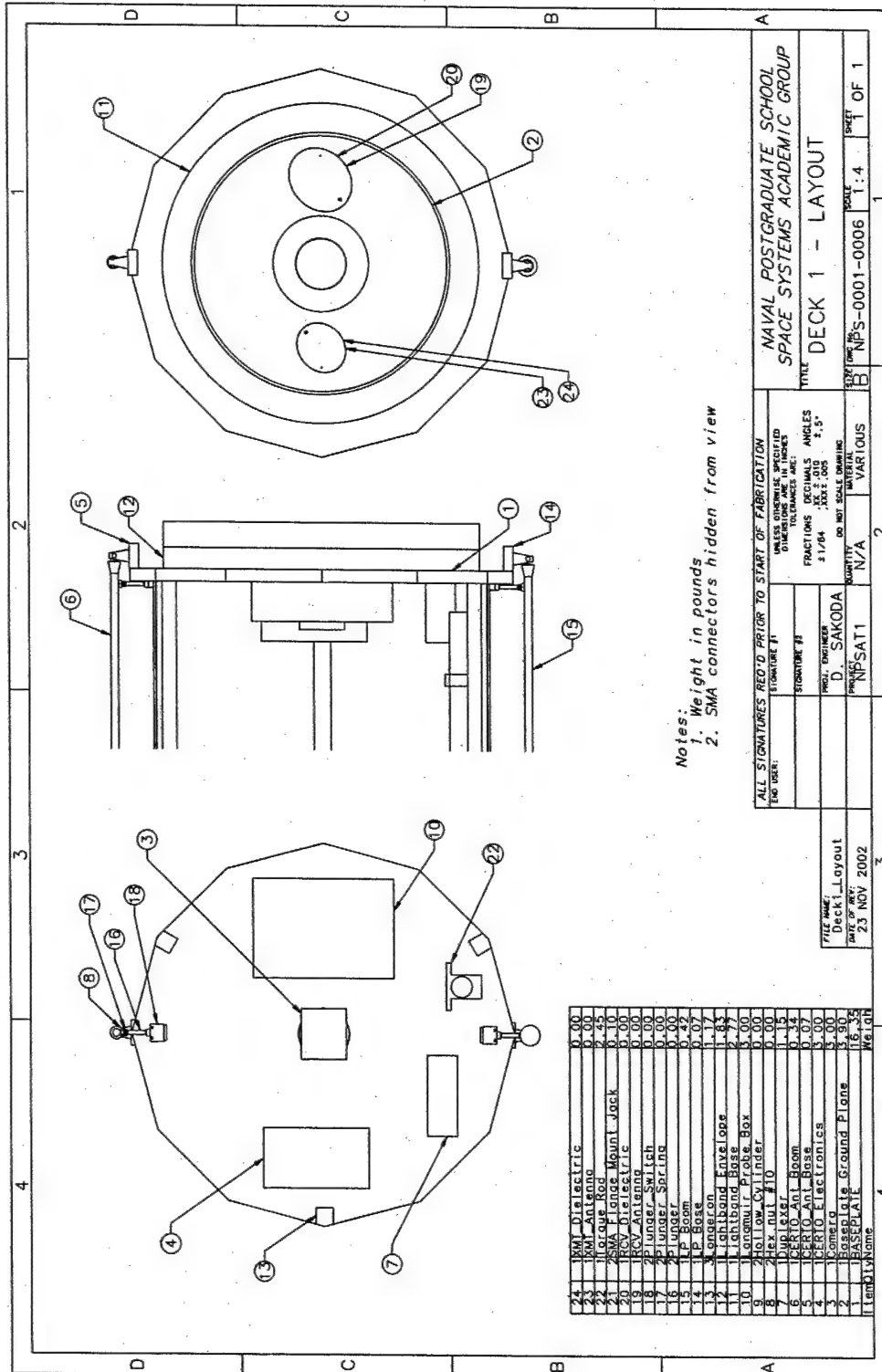
Cold case	Sunlight Period	Eclipse Period	Orbit Period	Sunlight Ave Power reqmnts	Eclipse Ave Power reqmnts	
	1.0042 hr	0.5933 hr	1.5975 hr	9.019 W	7.466 W	
				9.06 W-hr	4.43 W-hr	13.487 W-hr/orbit
Hot case	Sunlight Period	Eclipse Period	Orbit Period	Sunlight Ave Power reqmnts	Eclipse Ave Power reqmnts	
	1.2595 hr	0.3380 hr	1.5975 hr	9.019 W	7.466 W	
				11.36 W-hr	2.52 W-hr	13.883 W-hr/orbit

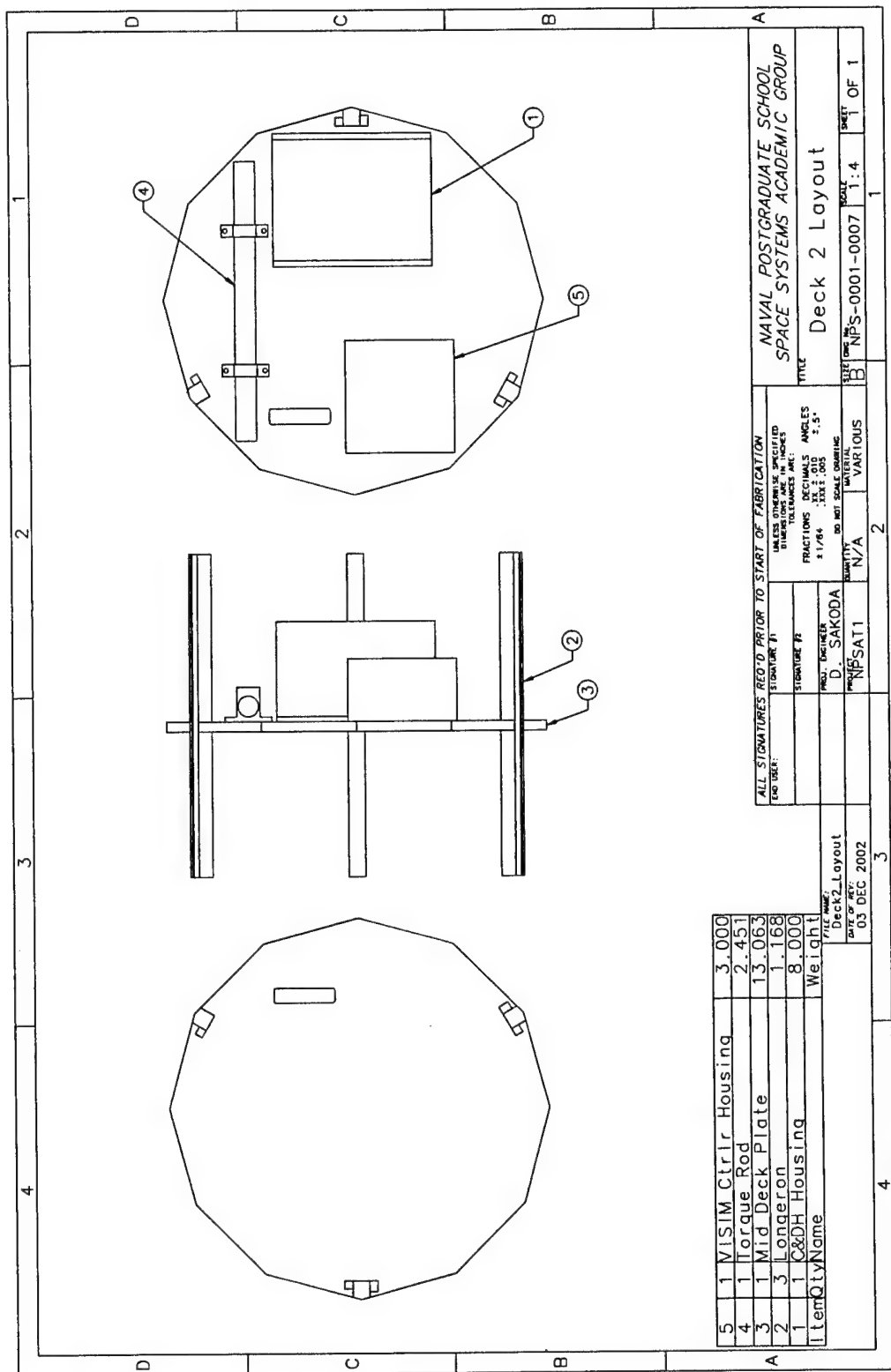
Subsystem		Maximum Power	Sunlight		Eclipse	
			Duty Cycle	Ave Power Req's	Duty Cycle	Ave Power Req's
EPS	Processor Board	1.500 W	50.0 %	0.750 W	50.0 %	0.750 W
	Switch Board	0.500 W	100.0 %	0.500 W	100.0 %	0.500 W
	A/D	0.065 W	50.0 %	0.033 W	50.0 %	0.033 W
	DAC	0.060 W	50.0 %	0.030 W	50.0 %	0.030 W
		2.125 W		1.313 W		1.313 W
ACS	Processor Board	1.500 W	50.0 %	0.750 W	50.0 %	0.750 W
C&DH/CPE	LO (+modem)	3.000 W	03.0 %	0.090 W	03.0 %	0.090 W
	386 Core (320mA @ 5V)	1.600 W	35.0 %	0.560 W	35.0 %	0.560 W
	RAM (1.236A @ 3.3V)	4.080 W	18.0 %	0.734 W	18.0 %	0.734 W
	SCC (15mA @ 5V)	0.080 W	100.0 %	0.080 W	100.0 %	0.080 W
	UART (45mA @ 5V)	0.210 W	33.0 %	0.069 W	33.0 %	0.069 W
	FPGA (75mA @ 3.3V)	0.250 W	35.0 %	0.088 W	35.0 %	0.088 W
	Solid State Disk	0.300 W	25.0 %	0.075 W	25.0 %	0.075 W
	A/D	0.200 W	50.0 %	0.100 W	50.0 %	0.100 W
	CPE	0.500 W	10.0 %	0.050 W	10.0 %	0.050 W
		10.220 W		1.846 W		1.846 W
RF-Switch	Tx/Rx (part of C&DH/CPE)	15.000 W	04.4 %	0.665 W	00.0 %	0.000 W
	Tx/Rx Switch	2.000 W	04.4 %	0.089 W	00.0 %	0.000 W
SMS	Processor Board	1.500 W	16.0 %	0.240 W	00.0 %	0.000 W
	A/D	0.065 W	16.0 %	0.010 W	00.0 %	0.000 W
	DAC	0.060 W	16.0 %	0.010 W	00.0 %	0.000 W
	1.625 W		0.260 W		0.000 W	
CERTO	Stndby(Cold)	3.470 W	12.5 %	0.434 W	12.5 %	0.434 W
	Stndby(Warm)	0.197 W	00.0 %	0.000 W	00.0 %	0.000 W
	Modes					
	150/400Mhz	7.640 W	20.0 %	1.528 W	20.0 %	1.528 W
	1067 Mhz	5.080 W	06.6 %	0.337 W	06.6 %	0.337 W
	16.387 W		2.298 W		2.298 W	
VISIM	Controller + Board	5.600 W	09.0 %	0.504 W	00.0 %	0.000 W
VISIM	Camera	0.400 W	09.0 %	0.036 W	00.0 %	0.000 W
Torque Rod (one)		0.030 W	50.0 %	0.015 W	50.0 %	0.015 W
Magnetometer		1.400 W	50.0 %	0.700 W	50.0 %	0.700 W
MEMS		2.400 W	05.0 %	0.120 W	05.0 %	0.120 W
Langmuir Probe		1.600 W	26.5 %	0.424 W	26.5 %	0.424 W
		60.287 W		9.019 W		7.466 W

THIS PAGE INTENTIONALLY LEFT BLANK

APPENDIX E. NPSAT1 DRAWINGS

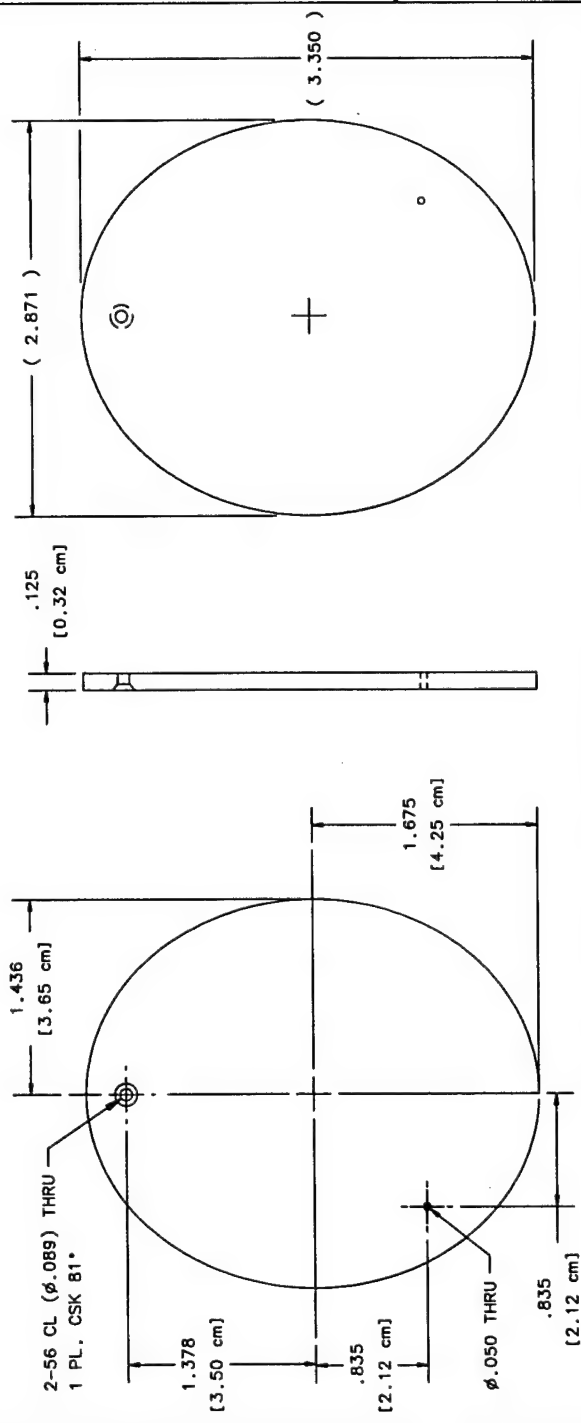
The drawings in this appendix are taken from Ref. 17. The selected ones are helpful to understand explanations in this thesis. All others can be found in Ref. 25.





DWG. NO. NPS-0001-0413 SH 0.1

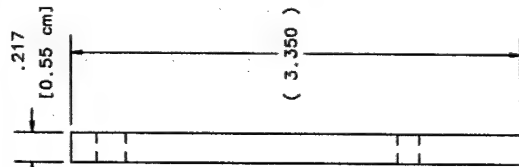
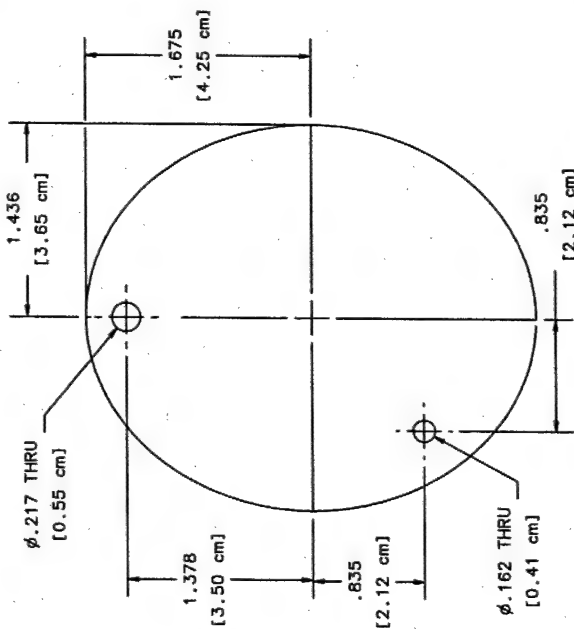
REVISIONS			
ZONE	REV	DESCRIPTION	DATE
	0.1	INITIAL	10/28/02
			D.S.



2	2	RCV ANTENNA	1.7 GHz Patch Receive Antenna	Copper	1
QTY REQD	FSQM NO	PART OR IDENTIFYING NO	NOMENCLATURE OR DESCRIPTION	MATERIAL SPECIFICATION	ITEM NO
PARTS LIST					
CONTRACT NO.			NPSAT1 PROJECT		
UNLESS OTHERWISE SPECIFIED DIMENSIONS ARE IN INCHES TOLERANCES ARE:			TITLE		
FRACTIONS DECIMALS ANGLES			NPSAT1 1.7 GHz PATCH ANTENNA		
± .XXX ±			DO NOT SCALE DRAWING		
TREATMENT			APPROVALS		
FINISH			DATE		
SIMILAR TO			DRAWN		
ACT. WT			CHECKED		
CALC WT			ISSUED		
SCALE 1:1			SIZE FSQM NO.		
SHEET 1 OF 1			DWG NO.		
			NPS-0001-0413		

REVISIONS

ZONE	REV	DESCRIPTION	DATE	APPROVED
	0.1	INITIAL	10/28/02	D.S.



QTY	RECD	FSQM NO	1.7GHz Dielectric	PART OR IDENTIFYING NO	NPSAT1 RECEIVE DIELECTRIC	NOMENCLATURE OR DESCRIPTION	TEFLON MATERIAL SPECIFICATION	ITEM NO
2								1

PARTS LIST

UNLESS OTHERWISE SPECIFIED DIMENSIONS ARE IN INCHES TOLERANCES ARE:		CONTRACT NO.		NPSAT1 PROJECT	
FRACTIONS	DECIMALS	ANGLES	APPROVALS	DATE	TITLE
±	.XX	±	DRAWN		NPSAT1 1.7 GHZ DIELECTRIC SPACER
DO NOT SCALE DRAWING			CHECKED		
TREATMENT			ISSUED		
FINISH					
SIMILAR TO	ART. WT	CALC WT	SIZE	FSQM NO.	DWG NO.
			A		NPS-0001-0414
			SCALE	1:1	SHEET 1 OF 1

THIS PAGE INTENTIONALLY LEFT BLANK

APPENDIX F. BOX BOLT DISTANCES

This appendix presents the calculated bolt distances for each component and derives the mesh size as explained in chapter V.B. Dimensions are taken from the drawings from Ref. 17. The number of mounting bolts is an assumption since this is not yet defined.

Deck 1:

Component	Mounting size	Number of mounting bolts	Shortest distance between two bolts	Required element length (in cm)
RF-Switch	10.16 x 3.18	4	3.18	< 5.51
CERTO	13.34 x 7.62	8	4.45	< 7.7
Camera	5 x 5	8	2.5	< 4.33
Torque Rod #3	n/a	2	n/a	n/a
Langmuir Probe	17.78 x 12.7	4	12.7	< 22
Structural Panel	12.55	3	4.18	< 7.24

Used: 4 cm

Deck 2:

Component	Mounting size	Number of mounting bolts	Shortest distance between two bolts	Required element length (in cm)
VISIM Ctrlr Housing	13.97 x 8	8	2.67	< 4.62
C&DH/Modem -RF/CPE	20.32 x 16.76	8	6.77	< 15.24
Torque Rod #2	34.9 x 6	4	5	< 5
Structural Panel	12.55	3	4.18	< 7.24

Used: 4.5 cm

Deck 3:

Component	Mounting size	Number of mounting bolts	Shortest distance between two bolts	Required element length (in cm)
EPS	25.4 x 9.65	8	8.47	< 14.67
ACS	25.4 x 9.65	8	8.47	< 14.67
Magnetometer	10.16 x 3.18	2	3.18	< 5.51
SMS	15.24 x 12.7	8	5.08	< 8.8
MEMS	6 x 6	3	4.24	< 7.34
Battery	19.71 x 17.78	6	9.86	< 17.08
Torque Rod #3	n/a	2	n/a	n/a
Torque Rod #1	34.9 x 6	4	5	< 8.66
Structural Panel	12.55	3	4.18	< 7.24

Used: 5 cm

APPENDIX G. EFFECTIVE SOLAR CELL ABSORPTANCE

This appendix provides the calculation of the effective solar absorptance for both commercial and experimental solar cells. The theoretical solar absorptance is influenced by the efficiency of the cells. To calculate the optical properties of the whole panel which carries the cells, a packing factor is used. The equation is obtained from Ref. 8.

Equation V.3:

$$\overline{\alpha_{sol,eff}} = \overline{\alpha_{sol}} - F_{pg} \cdot \eta$$

Commercial cells

Solar cell data [Ref. 19]:

Spectrolab 26.8 % Improved Triple Junction (ITJ) Solar Cells:

Emissivity: $\epsilon = 0.85$

Absorptivity: $\alpha = 0.92$

η_{op} : 26.5 % for BOL, 22.3 % for EOL

F_{pg} :

6 x 12 solar cells on a long/commercial panel. [Ref. 17]

One cell: $1.65 \text{ cm} \cdot 1.65 \text{ cm} = 2.7225 \text{ cm}^2$

72 cells $\cdot 2.7225 \text{ cm}^2/\text{cell} = 196.02 \text{ cm}^2$

Panel size from Ref. 17: $21.42 \text{ cm} \cdot 12.4 \text{ cm} = 265.608 \text{ cm}^2$

$F_{pg} = 196.02 \text{ cm}^2 / 265.608 \text{ cm}^2 = 73.8 \%$

BOL: $\overline{\alpha_{sol,eff}} = 0.92 - 0.738 \cdot 0.265 = \underline{0.72443}$

EOL: $\overline{\alpha_{sol,eff}} = 0.92 - 0.738 \cdot 0.223 = \underline{0.75543}$

Experimental cells

Solar cell data (provided by Space Systems Academic Group):

$$\eta_{op}: 24 \%$$

$$F_{pg}:$$

6 x 10 solar cells on a long/commercial panel. [Ref. 17]

$$\text{One cell: } 1.65 \text{ cm} \cdot 1.65 \text{ cm} = 2.7225 \text{ cm}^2$$

$$60 \text{ cells} \cdot 2.7225 \text{ cm}^2/\text{cell} = 163.35 \text{ cm}^2$$

$$\text{Panel size from Ref. 17: } 19.05 \text{ cm} \cdot 12.4 \text{ cm} = 236.22 \text{ cm}^2$$

$$F_{pg} = 163.35 \text{ cm}^2 / 236.22 \text{ cm}^2 = 69.15 \%$$

$$\overline{\alpha_{sol,eff}} = 0.92 - 0.6915 \cdot 0.24 = \underline{\underline{0.75404}}$$

APPENDIX H. MATERIAL THICKNESSES

This appendix provides all used material thicknesses that are necessary for the meshing (chapter V.B). They were derived from drawings [Ref. 17] or directly measured in the provided structural model, since this is built using the original properties.

<i>Part</i>	<i>Thickness in mm</i>
First and third deck	15.875
Second deck	12.7
Fourth deck	6.35
Lower structural panel	4.826
Upper structural panel	3.175
Antenna ground plates	3.175
Patch antenna	3.2
Lightband	36.068
Commercial solar cell panel	1.775 (AL-plate: 1.6, solar cell: 0.175)
Experimental solar cell panel	3.175 (AL-plate: 3, solar cell: 0.175)

THIS PAGE INTENTIONALLY LEFT BLANK

APPENDIX I. CAPACITANCE CALCULATIONS

This appendix provides two different approaches to calculate the thermal capacitance for the non-geometric elements representing the operating subsystems.

The first calculation is based on the maximum allowed weight for the components and the heat capacity, which is assumed to be representative for the complete components. Aluminum 6061-T6 was chosen, since all housings and the mechanical structure of NPSAT1 consists of this material. Its heat capacity is $896 \text{ J}/(\text{kg} \cdot \text{K})$. [Ref. 1] Weight and heat capacity are multiplied.

<u>Component</u>	<u>Weight (kg)</u>	<u>Capacitance (J/K)</u>
Camera	1.3608	1224.72
Langmuir Probe	1.3608	1224.72
CERTO	1.3608	1224.72
RF Switch	0.52164	469.476
C&DH/CPE	3.6288	3265.92
Camera controller	1.3608	1224.72
EPS	2.7216	2449.44
ACS Processor	2.7216	2449.44
Magnetometer	0.140616	126.5544
SMS	2.268	2041.2
MEMS (incl. mounting block)	0.766584	689.9256
Torque rod (one)	1.11132	1000.188
Battery	5.4432	4898.88

The second calculation is based on the geometry [Ref. 17] and on information and assumptions by the Space Systems Academic Group about the design of components.

From this a weight was calculated and multiplied with the heat capacitances. For camera and torque rod, the weight was known. Finally a margin was added.

Subsystem	Mounted Side		Height (m)	No of Boards	Bolts per Board	Weight of Bolt
	Length (m)	Width (m)				
Langmuir Probe lower box	0.1270	0.1778	0.0254	1	14	0.0018765
Langmuir Probe upper box	0.1270	0.1778	0.0254	1	14	0.0018765
CERTO lower box	0.0762	0.1334	0.0381	1	14	0.0018765
CERTO upper box	0.0762	0.0800	0.0381	1	14	0.0018765
RF Switch	0.1016	0.0381	0.0762	1	14	0.0018765
C&DH/CPE	0.2032	0.1676	0.1270	4	14	0.0018765
Camera controller	0.1524	0.1270	0.0762	1	14	0.0018765
EPS	0.2540	0.0965	0.2286	1	14	0.0018765
ADCS Processor	0.2540	0.0965	0.2286	1	14	0.0018765
Magnetometer	0.1016	0.0318	0.0349	2	14	0.0018765
SMS	0.1524	0.1270	0.0762	2	14	0.0018765
MEMS	0.0378	0.0378	0.0135	1	8	0.0018765
MEMS Mounting Block	0.0600	0.0600	0.0600	0	0	
Torque Rod	Weight (kg)	Material			Density (kg/m ³)	Specific Heat (J/(kg·K))
	1.05	Aluminum		Aluminum	2700	896
Camera	Weight (kg)	Material				
	0.3	Aluminum		Fiberglass	105	795

Basic calculation data.

Subsystem	Box Vol. (m ³)	Box Weight (kg)	Box Cap. (J/K)	Board Vol. (m ³)	Board Weight (kg)	Board Cap. (J/K)	Joint Weight (kg)	Joint Cap. (J/K)	$\Sigma + 10\%$ (J/K)
Langmuir Probe	0.000291	0.7865	704.7044	0.0001	0.0078	6.2202	0.0263	23.5388	807.9097
CERTO	0.000142	0.3840	344.0929	0.0000	0.0034	2.6973	0.0263	23.5388	407.3619
RF Switch	0.000068	0.1844	165.2345	0.0000	0.0024	1.9388	0.0263	23.5388	209.7833
C&DH/CPE	0.000400	1.0789	966.6692	0.0004	0.0429	34.1224	0.0263	23.5388	1126.7634
Camera controller	0.000197	0.5331	477.6259	0.0001	0.0061	4.8469	0.0263	23.5388	556.6128
EPS	0.000517	1.3953	1250.2001	0.0002	0.0183	14.5408	0.0263	23.5388	1417.1077
ADCS Processor	0.000517	1.3953	1250.2001	0.0002	0.0183	14.5408	0.0263	23.5388	1417.1077
Magnetometer	0.000036	0.0968	86.6906	0.0000	0.0022	1.7772	0.0263	23.5388	123.2073
SMS	0.000197	0.5331	477.6259	0.0001	0.0122	9.6939	0.0263	23.5388	561.9444
MEMS	0.000061	0.1637	146.6829	0.0000	0.0005	0.3587	0.0263	23.5388	187.6385
Subsystem	Weight (kg)	Capacitance (J/K)							
Torque Rod	1.05	940.80							
Camera	0.30	268.80							

Capacitance calculation based on geometry.

THIS PAGE INTENTIONALLY LEFT BLANK

APPENDIX J. GROUND STATION COVERAGE

This appendix provides the ground station coverage. This ground station coverage is used as duty cycle for CERTO and Langmuir Probe. The first table shows all accesses from the ground station. The next table accumulates them to obtain the duty cycles. The third table shows the relation to the orbits per day. NPSAT1 ground station coverage:

Access	Start Time (UTCG)	Stop Time (UTCG)	Duration (sec)	Location
1	0:09:19	0:22:07	767.366	Clemson
2	0:11:07	0:23:35	747.708	NRL, DC
3	1:50:14	2:03:21	786.979	Clemson
4	1:51:43	2:04:41	778.147	NRL, DC
5	3:31:30	3:44:37	786.963	Clemson
6	3:32:44	3:45:34	770.208	NRL, DC
7	5:12:45	5:25:30	765.95	Clemson
8	5:14:02	5:25:38	696.806	NRL, DC
9	5:20:48	5:29:06	497.167	Bogota
10	6:54:39	7:04:48	609.035	Clemson
11	6:57:11	7:03:01	350.592	NRL, DC
12	7:00:05	7:12:51	766.342	Bogota
13	7:05:11	7:12:16	425.718	Jicamarca
14	8:41:38	8:53:27	708.728	Bogota
15	8:43:22	8:56:07	765.375	Jicamarca
16	9:31:39	9:42:12	632.233	Waltair
17	10:24:51	10:37:01	730.372	Jicamarca
18	11:11:19	11:24:22	782.977	Waltair
19	12:09:02	12:16:49	466.845	Jicamarca
20	12:53:28	13:05:08	699.845	Waltair
21	14:37:00	14:46:07	546.958	Waltair
22	15:35:54	15:42:00	366.312	Jicamarca
23	16:19:31	16:28:52	560.982	Waltair
24	17:15:30	17:26:54	683.513	Jicamarca
25	18:00:24	18:12:21	716.873	Waltair
26	18:56:02	19:09:03	781.005	Jicamarca
27	19:00:07	19:11:50	702.593	Bogota
28	19:41:14	19:54:15	780.807	Waltair
29	20:38:42	20:48:22	579.262	Jicamarca
30	20:40:39	20:53:27	768.711	Bogota
31	21:23:45	21:33:30	585.371	Waltair
32	22:24:18	22:32:48	510.164	Bogota
33	22:25:11	22:36:26	674.833	Clemson
34	22:27:08	22:37:58	649.735	NRL, DC

NPSAT1 coverage of ground stations (accumulated):

<i>Accumulated duty cycle</i>					
<u>Access</u>	<u>Start Time</u> (UTCG in h)	<u>Stop Time</u> (UTCG in h)	<u>Duration (s)</u>	<u>Location</u>	<u>Orbitnr.</u>
1	0:09:19	0:23:35	0:14:16	Clemson, NRL	1
2	1:50:14	2:04:41	0:14:28	Clemson, NRL	2
3	3:31:30	3:45:34	0:14:04	Clemson, NRL	3
4	5:12:45	5:29:06	0:16:21	Clemson, NRL, Bogota	4
5	6:54:39	7:12:51	0:18:12	Clemson, NRL, Bogota, Jicamarca	5
6	8:41:38	8:56:07	0:14:29	Bogota, Jicamarca	6
7	9:31:39	9:42:12	0:10:32	Waltair	6+7
8	10:24:51	10:37:01	0:12:10	Jicamarca	7
9	11:11:19	11:24:22	0:13:03	Waltair	8
10	12:09:02	12:16:49	0:07:47	Jicamarca	8
11	12:53:28	13:05:08	0:11:40	Waltair	9
12	14:37:00	14:46:07	0:09:07	Waltair	10
13	15:35:54	15:42:00	0:06:06	Jicamarca	10
14	16:19:31	16:28:52	0:09:21	Waltair	11
15	17:15:30	17:26:54	0:11:24	Jicamarca	11
16	18:00:24	18:12:21	0:11:57	Waltair	12
17	18:56:02	19:11:50	0:15:47	Jicamarca, Bogota	12+13
18	19:41:14	19:54:15	0:13:01	Waltair	13
19	20:38:42	20:53:27	0:14:45	Jicamarca, Bogota	13+14
20	21:23:45	21:33:30	0:09:45	Waltair	14
21	22:24:18	22:37:58	0:13:40	Bogota, Clemson, NRL	15

NPSAT1 ground station coverage per orbit:

<u>Orbit starttime (h)</u>	<u>Orbitnr.</u>	<u>Nr. of duties per orbit</u>
0:00:00	1	1
1:35:51	2	1
3:11:42	3	1
4:47:33	4	1
6:23:24	5	1
7:59:15	6	2
9:35:06	7	2
11:10:57	8	2
12:46:48	9	1
14:22:39	10	2
15:58:30	11	2
17:34:21	12	2
19:10:12	13	3
20:46:03	14	2
22:21:54	15	1
23:57:45	16	

APPENDIX K. DUTY CYCLES FOR LOW FREQUENCY DEVICES

This appendix provides the duty cycles for all low frequency devices. If the duty cycles depend on sun and eclipse, both are provided. The format is the one used to build "tabular data" in I-DEAS. The option "constant over interval" has to be chosen. Those duty cycles used for more than one device do not have a heat load value, but only a cut-in and cut-off time. The heat load value of them is adjusted via a multiplier in the thermal boundary condition, were the table is used with the specific value.

<i>Time (h)</i>	<i>Heat Load (W)</i>
Battery (cold case)	
0	0
1.0042	0.843
1.5975	0.843
Battery (hot case)	
0	0
1.25947	0.682
1.5975	0.682
CERTO and Langmuir Probe	
0	0
1.55277	1
0.393055	0
1.83722	1
2.078055	0
3.525	1
3.759444	0
5.2125	1
5.485	0
6.91	1
7.214166	0
8.693889	1
8.935555	0
9.527500	1
9.703333	0
10.414167	1
10.616944	0
11.188611	1
11.406111	0
12.150555	1
12.280278	0

<i>Time (h)</i>	<i>Heat Load (W)</i>
12.891111	1
13.08555	0
14.616667	1
14.768611	0
15.598333	1
15.7	0
16.325278	1
16.481111	0
17.258333	1
17.448333	0
18.006667	1
18.205833	0
18.933889	1
19.197222	0
19.687222	1
19.904167	0
20.645000	1
20.890833	0
21.395833	1
21.558333	0
22.405	1
22.632778	0
24	0
RF-Switch (cold case)	
0	0
16.3938	1
16.5605	0
17.9913	1
18.158	0
19.5888	1
19.7554	0
21.1863	1
21.3529	0
24	0
RF-Switch (hot case)	
0	0
16.5214	1
16.6881	0
18.1189	1
18.2856	0
19.7164	1
19.883	0
21.3139	1
21.4805	0
24	0

<i>Time (h)</i>	<i>Heat Load (W)</i>
SMS (cold case)	
0	1.63
0.080336	0
0.923864	163
1.00421	0
1.5975	0
SMS (hot case)	
0	1.63
0.080336	0
1.17914	1.63
1.25947	0
1.5975	0
VISIM	
0	5
0.090378	0
1.5975	0

THIS PAGE INTENTIONALLY LEFT BLANK

APPENDIX L. BATTERY HEAT GENERATION

This appendix provides the calculation of the battery heat generation resulting from discharge. The efficiency η is 90 % [Ref. 18]. The calculation is based on equation V.4:

$$P = \frac{(1 - \eta) \cdot W_{ecl}}{\eta \cdot \Delta t_{ecl}}$$

Cold case:

Energy supplied by the battery: 4.5 Wh (rounded conservatively from 4.43 Wh taken from the power budget in App. D)

$$\Delta t_{ecl} = 0.5933 \text{ h (Tab. 2)}$$

$$P = \frac{(1 - 0.9) \cdot 4.5 \text{ Wh}}{0.9 \cdot 0.5933 \text{ h}} = \underline{\underline{0.843 \text{ W}}}$$

Hot case:

Energy supplied by the battery: 2.56 Wh (adjusted to the hot case orbit from the power budget in App. D)

$$\Delta t_{ecl} = 0.338 \text{ h (Tab. 2)}$$

$$P = \frac{(1 - 0.9) \cdot 2.56 \text{ Wh}}{0.9 \cdot 0.338 \text{ h}} = \underline{\underline{0.682 \text{ W}}}$$

THIS PAGE INTENTIONALLY LEFT BLANK

APPENDIX M. CONTACT CONDUCTANCES

This appendix provides the comparison and calculation of thermal contact conductances used in the thermal model. The used thicknesses of the decks in the upper section of the table for equation III.15 represent the real thicknesses from App. H, but are in this case arbitrary assumptions, because the mounting is done in a rectangular angle.

		Bratkovich	Gluck dimensional	Gluck non-dimensional	TRW small stiff
	Equation:	III.15	III.16	III.17	
Part 1	Part 2	W/K	W/K	W/K	W/K
Fourth deck	Side Panel	0.93	0.82	1.78	1.32
Third deck	Side Panel	1.07	0.69	1.61	0.8
Second deck	Side Panel	0.98	0.69	1.61	0.8
First deck	Side Panel	1.30	0.82	1.78	1.32
Beam	Side Panel	0.81	0.55	1.41	0.42
Beam	Third deck	1.79	0.82	1.78	1.32
Beam	Second deck	1.71	0.82	1.78	1.32
Beam	First deck	1.79	0.82	1.78	1.32
First deck	Lightband	3.97	1.12	2.12	3.51
EPS	Third deck	1.10	0.69	1.61	0.8
ACS	Third deck	1.10	0.69	1.61	0.8
Magnetometer	Third deck	0.54	0.23	0.74	0.26
SMS	Third deck	1.07	0.69	1.61	0.8
MEMS	Third deck	0.56	0.23	0.74	0.26
Battery	Third deck	1.10	0.69	1.61	0.8
Torque rod Y	Third deck	1.39	0.82	1.78	1.32
Torque rod Z	Third deck	1.39	0.82	1.78	1.32
Torque rod X	Second deck	1.29	0.82	1.78	1.32
Torque rod Z	First deck	1.39	0.82	1.78	1.32
C&DH/CPE	Second deck	1.02	0.69	1.61	0.8
VISIM controller	Second deck	0.99	0.69	1.61	0.8
VISIM camera	First deck	0.74	0.55	1.41	0.42
Langmuir Probe	First deck	1.75	0.82	1.78	1.32
CERTO	First deck	0.74	0.55	1.41	0.42
RF Switch	First deck	0.54	0.23	0.74	0.26
TRW: Test results for small stiff surfaces from TRW Inc., provided by Ref. 5					

Calculation using Bratkovich-equation (III.15):

Part 1	Part 2	thickness 1 (t_1)	thickness 2 (t_2)	aver. thickn. (t_m)	bolt size	area (A_b)	max. torque (T_{max})	aver. temp. °C	abs. aver. temp. K	Coef. of Expan. ($\alpha \cdot 10^{-6}$)	Thermal Conductivity (k)	Yield Stress (σ)	Finish (R_a)	Cont. Cond. (C_p)
		m	m	m		m ²	Nm			1/K	W/(m·K)	N/m ²	10 ⁻⁴ m	WK
Fourth deck	Side Panel	0.006350	0.003175	0.0048	#10-32	0.00007317	3.5792153	4	277.15	22.59	148.843	253,175,000	0.635	0.927
Third deck	Side Panel	0.015875	0.004826	0.0104	#8-32	0.00005451	2.2355982	4	277.15	22.59	148.843	253,175,000	0.635	1.065
Second deck	Side Panel	0.012700	0.004826	0.0088	#8-32	0.00005451	2.2355982	4	277.15	22.59	148.843	253,175,000	0.635	0.982
First deck	Side Panel	0.015875	0.004826	0.0095	#10-32	0.00007317	3.5792153	4	277.15	22.59	148.843	253,175,000	0.635	1.301
Beam	Side Panel	0.020540	0.004826	0.0127	#6-32	0.00003860	1.0839264	4	277.15	22.59	148.843	253,175,000	0.635	0.813
Beam	Third deck	0.020540	0.015875	0.0182	#10-32	0.00007317	3.5792153	4	277.15	22.59	148.843	253,175,000	0.635	1.786
Beam	Second deck	0.020540	0.012700	0.0166	#10-32	0.00007317	3.5792153	4	277.15	22.59	148.843	253,175,000	0.635	1.708
Beam	First deck	0.020540	0.015875	0.0182	#10-32	0.00007317	3.5792153	4	277.15	22.59	148.843	253,175,000	0.635	1.786
First deck	Lightband	0.015876	0.059660	0.0378	#1/4-20	0.00012668	8.4907568	4	277.15	22.59	148.843	253,175,000	0.635	3.968
EPS	Third deck	0.008350	0.015875	0.0111	#8-32	0.00005451	2.2355982	4	277.15	22.59	148.843	253,175,000	0.635	1.103
ACS	Third deck	0.006350	0.015875	0.0111	#8-32	0.00005451	2.2355982	4	277.15	22.59	148.843	253,175,000	0.635	1.103
Magnetometer	Third deck	0.005080	0.015875	0.0105	#4-40	0.00002542	0.5871268	4	277.15	22.59	148.843	253,175,000	0.635	0.541
SMS	Third deck	0.005080	0.015875	0.0105	#8-32	0.00005451	2.2355982	4	277.15	22.59	148.843	253,175,000	0.635	1.072
MEMS	Third deck	0.006223	0.015875	0.0110	#4-40	0.00002542	0.5871268	4	277.15	22.59	148.843	253,175,000	0.635	0.555
Battery	Third deck	0.006350	0.015875	0.0111	#8-32	0.00005451	2.2355982	4	277.15	22.59	148.843	253,175,000	0.635	1.103
Torque rod Y	Third deck	0.005994	0.015875	0.0109	#10-32	0.00007317	3.5792153	4	277.15	22.59	148.843	253,175,000	0.635	1.392
Torque rod Z	Third deck	0.005994	0.015875	0.0109	#10-32	0.00007317	3.5792153	4	277.15	22.59	148.843	253,175,000	0.635	1.392
Torque rod X	Second deck	0.005994	0.012700	0.0093	#10-32	0.00007317	3.5792153	4	277.15	22.59	148.843	253,175,000	0.635	1.289
Torque rod Z	First deck	0.005994	0.015875	0.0109	#10-32	0.00007317	3.5792153	4	277.15	22.59	148.843	253,175,000	0.635	1.392
C&D/H/CPE	Second deck	0.006350	0.012700	0.0095	#8-32	0.00005451	2.2355982	4	277.15	22.59	148.843	253,175,000	0.635	1.023
VISIM controller	Second deck	0.005080	0.012700	0.0089	#8-32	0.00005451	2.2355982	4	277.15	22.59	148.843	253,175,000	0.635	0.989
VISIM camera	First deck	0.005080	0.015875	0.0105	#8-32	0.00003860	1.0839264	4	277.15	22.59	148.843	253,175,000	0.635	0.740
Langmuir Probe	First deck	0.019050	0.015875	0.0175	#10-32	0.00007317	3.5792153	4	277.15	22.59	148.843	253,175,000	0.635	1.750
CERTO	First deck	0.005080	0.015875	0.0105	#6-32	0.00003860	1.0839264	4	277.15	22.59	148.843	253,175,000	0.635	0.740
RF Switch	First deck	0.005080	0.015875	0.0105	#4-40	0.00002542	0.5871268	4	277.15	22.59	148.843	253,175,000	0.635	0.541
Thicknesses: Ref. 17														
Bolt size: Ref. 17 if yet designed, otherwise assumption by SSAG														
area: equation from Ref. 4 with bolt shaft diameter from Ref. 4														
max. torque: depending on screws size, Ref. 4														
average temperature: average of most extrem temperatures in App. A														
Coef of therm. expansion, thermal conductivity, yield stress: Ref. 2														
Finish thickness: Ref. 4														
Used equation for contact conductance: III.15														

Calculation using Glucks equations (III.16 and III.17):

Part 1	Part 2	bolt size	installation torque (ti)	aver. temp. °C	abs. aver. temp. K	Thermal Conductivity (k)	RMS (σ)	Bolt Diameter (D _B)	effective modulus (E')	Equation III.17		Equation III.16	
										Conductance (C _j)	Conductance (C _j)	Conductance (C _j)	Conductance (C _j)
			Nm		K	W/(m·K)	m	m	N/m ²	W/K	W/K	W/K	W/K
Fourth deck	Side Panel	#10-32	0.56	4	277.15	148.843	5.66E-07	0.004826	3.87E+10	1.78	1.78	0.82	0.82
Third deck	Side Panel	#8-32	0.45	4	277.15	148.843	5.66E-07	0.004166	3.87E+10	1.61	1.61	0.69	0.69
Second deck	Side Panel	#8-32	0.45	4	277.15	148.843	5.66E-07	0.004166	3.87E+10	1.61	1.61	0.69	0.69
First deck	Side Panel	#10-32	0.56	4	277.15	148.843	5.66E-07	0.004826	3.87E+10	1.78	1.78	0.82	0.82
Beam	Side Panel	#6-32	0.34	4	277.15	148.843	5.66E-07	0.003505	3.87E+10	1.41	1.41	0.55	0.55
Beam	Third deck	#10-32	0.56	4	277.15	148.843	5.66E-07	0.004826	3.87E+10	1.78	1.78	0.82	0.82
Beam	Second deck	#10-32	0.56	4	277.15	148.843	5.66E-07	0.004826	3.87E+10	1.78	1.78	0.82	0.82
Beam	First deck	#10-32	0.56	4	277.15	148.843	5.66E-07	0.004826	3.87E+10	1.78	1.78	0.82	0.82
First deck	Lightband	#1/4-20	0.85	4	277.15	148.843	5.66E-07	0.006350	3.87E+10	2.12	2.12	1.12	1.12
EPS	Third deck	#8-32	0.45	4	277.15	148.843	5.66E-07	0.004166	3.87E+10	1.61	1.61	0.69	0.69
ACS	Third deck	#8-32	0.45	4	277.15	148.843	5.66E-07	0.004166	3.87E+10	1.61	1.61	0.69	0.69
Magnetometer	Third deck	#4-40	0.11	4	277.15	148.843	5.66E-07	0.002845	3.87E+10	0.74	0.74	0.23	0.23
SMS	Third deck	#8-32	0.45	4	277.15	148.843	5.66E-07	0.004166	3.87E+10	1.61	1.61	0.69	0.69
MEMS	Third deck	#4-40	0.11	4	277.15	148.843	5.66E-07	0.002845	3.87E+10	0.74	0.74	0.23	0.23
Battery	Third deck	#8-32	0.45	4	277.15	148.843	5.66E-07	0.004166	3.87E+10	1.61	1.61	0.69	0.69
Torque rod Y	Third deck	#10-32	0.56	4	277.15	148.843	5.66E-07	0.004826	3.87E+10	1.78	1.78	0.82	0.82
Torque rod Z	Third deck	#10-32	0.56	4	277.15	148.843	5.66E-07	0.004826	3.87E+10	1.78	1.78	0.82	0.82
Torque rod X	Second deck	#10-32	0.56	4	277.15	148.843	5.66E-07	0.004826	3.87E+10	1.78	1.78	0.82	0.82
Torque rod Z	First deck	#10-32	0.56	4	277.15	148.843	5.66E-07	0.004826	3.87E+10	1.78	1.78	0.82	0.82
CAD/ICPE	Second deck	#8-32	0.45	4	277.15	148.843	5.66E-07	0.004166	3.87E+10	1.61	1.61	0.69	0.69
VISIM controller	Second deck	#8-32	0.45	4	277.15	148.843	5.66E-07	0.004166	3.87E+10	1.61	1.61	0.69	0.69
VISIM camera	First deck	#6-32	0.34	4	277.15	148.843	5.66E-07	0.003505	3.87E+10	1.41	1.41	0.55	0.55
Langmuir Probe	First deck	#10-32	0.56	4	277.15	148.843	5.66E-07	0.004826	3.87E+10	1.78	1.78	0.82	0.82
CERTO	First deck	#6-32	0.34	4	277.15	148.843	5.66E-07	0.003505	3.87E+10	1.41	1.41	0.55	0.55
RF Switch	First deck	#4-40	0.11	4	277.15	148.843	5.66E-07	0.002845	3.87E+10	0.74	0.74	0.23	0.23
Bolt size: Ref. 17 if yet designed, otherwise assumption by SSAG													
Installation torque: Ref. 18													
average temperature: average of most extrem temperatures in App. A													
Thermal conductivity: Ref. 2													
RMS: Ref. 5													
Bolt Diameter: Ref. 4													
effective modulus of elasticity: Ref. 5													
Coeff of therm. exp. (α) α _{al} - α _{ss} (1/K)													
0.00000576412 (Ref. 2)													

Conductance calculation for spacers:

	Radius (R _i)	Radius (R _o)	Area (A)	Thickness (l)	Therm. Cond. (k)	Conductance (C _j)
	m	m	m ²	m	W/m·K	W/K
Battery-Plate Spacer (Teflon)	0.001981	0.005563	0.000085	0.001016	0.25	0.0209
Battery-Plate Bolt		0.001981	0.000012	0.005000	12.6	0.0311
Battery-Plate Spacer (steel)	0.001981	0.005563	0.000085	0.005000	12.6	0.2139
Battery-Plate (sum)						0.2450
Antenna-Ground Bolt		0.001130	0.000004	0.005500	12.6	0.0092
AntennaGrPlate-4thPlate Bolt		0.001753	0.000010	0.038087	12.6	0.0032
AntennaGrPlate-4thPlate Spacer	0.001753	0.017500	0.000952	0.038087	12.6	0.3151
AntennaGrPlate-4thPlate (sum)						0.3183
Bolt radii: Ref. 4						
Spacer radii: assumption						
Therm. conductivity: Ref. 1						
Thickness: Ref. 17, battery spacer: assumption						
used equation: V.5						

APPENDIX N. PYTHON SOURCE CODE

This appendix provides Python source code of data transfer scripts that are described with a flowchart in chapter VI. Only one code example for extraction of data from the TMPF and from the REPF file is shown, since the others have only changes in numbers. They can be found in Ref. 25.

Python script for extraction of TMPF file from I-DEAS TMG output:

```
import dircache, string, sys

# variable initialization
start_val = 0
time_step = 120
temp_num = 15
a = 0
# set variable input_name to file name
input_name = 'TMPF'

# open the file for processing read-only
fp = open(input_name,'r')
fout=open('Results_non-geom.csv','w')

# write table header
fout.write(",Ele#99984,Ele#99985,Ele#99986,Ele#99987,Ele#99988,Ele#99989,Ele#99990,Ele#99991,Ele#99992,Ele#99993,Ele#99994,Ele#99995,Ele#99996,Ele#99997,Ele#99998\n")
fout.write("Time,Battery,RF-Switch,SMS,VISIM_Controller,VISIM_camera,Langmuir,CERTO,EPS,ACS,TorqueX,TorqueY,TorqueZ,Magnetometer,MEMS,C&DH/CPE\n")

# read and split first line of input file
line1 = fp.readline()
ele_num = int(line1[:7])
temperature = float(line1[8:])

# process until EOF
while len(line1) > 0:

    # process for element of interest
    if (ele_num > 99983) & (ele_num < 99999):
        # write all element temperatures for one time step
        if a == 0:
            fout.write("%d,"%(start_val))
            fout.write("%f,"%(temperature))
            a=a+1
        # end of time step, start of next time step
        if a == temp_num:
            fout.write("\n")
            start_val = start_val + time_step
```

```

        a = 0
    # read and split next line of input file
    line1 = fp.readline()
    ele_num = int(line1[:7])
    temperature = float(line1[8:])
# close files and end script
fp.close()
fout.close()

```

Python script for extraction of REPF file from I-DEAS TMG output:

```

import dircache, string, sys

# variable initialization
start_val = 0
time_step = 120
# set variable input_name to file name
input_name = 'REPF'

# open the file for processing read-only
fp = open(input_name, 'r')
fout = open('Results_battery_heatflow.csv', 'w')

# write table header
fout.write("Time,Battery\n")

# write first time step
fout.write("%d,%d"%(start_val, time_step))

# process until last time step
while start_val < 86520:

    # read line from input file and extract information
    line1 = fp.readline()
    ele_num = str(line1[1:6])
    temperature = str(line1[57:66])
    heattype = str(line1[67:74])

    # write heatflow if battery and heat flow type are found
    if ele_num == "99984" and heattype == "Convect":
        fout.write("%s,%s"%(start_val, temperature))

    # end time step and start new time step in table, if indicator is found
    if ele_num == "99984" and heattype == "Heatsum":
        start_val = start_val + time_step
        fout.write("\n")
        if start_val < 86520:
            fout.write("%d,%d"%(start_val, time_step))

# close file and end script
fp.close()
fout.close()

```


LIST OF REFERENCES

- [1] Automation Creation Inc., *MatWeb*, www.matweb.com, 10th January 2003
- [2] Department of Defense (USA), *Military Handbook, Metallic Materials and Elements for Aerospace Vehicle Structures*, MIL-HDBK-5H, 1998
- [3] Department of Defense (USA), *Military Handbook, Design, Construction, and Testing Requirements for One of a Kind Space Equipment*, DOD-HDBK-343, Department of the Airforce, Washington, 1986
- [4] Gilmore, David G., *Satellite Thermal Control Handbook*, The Aerospace Corporation Press, El Segundo, 1994
- [5] Gilmore, David G., *Spacecraft Thermal Control Handbook, Volume I: Fundamental Technologies*, 2nd edition, The Aerospace Press, El Segundo, 2002
- [6] Gluck, D. and Baturkin, V., *Update of Thermal Control of Mountings and Interfaces*, Spacecraft Thermal Control Workshop, The Aerospace Corporation, El Segundo, March 11-13, 2003
- [7] Incropera, F. P. and DeWitt, D.P., *Fundamentals of Heat and Mass Transfer*, 4th edition, John Wiley & Sons, New York, 1996
- [8] Jet Propulsion Laboratory, *Solar Cell Array Design Handbook*, Volume 1, National Aerospace and Space Administration (NASA), Pasadena, 1976
- [9] Karam, R. D., *Satellite Thermal Control for Systems Engineers*, American Institute of Aeronautics and Astronautics, Inc., Reston, 1998
- [10] Lawry, M. H., *I-deas Master Series Student Guide*, Structural Dynamics Research Corporation, Milford, 1999
- [11] Moffit, B. A. and Batty, J. C., *Predictive Thermal Analysis of the Combat Sentinel Satellite*, Utah State University, Logan
- [12] NASA Headquarters, *WIRE Mishap Investigation Board Report, June 8, 1999*, ftp://ftp.hq.nasa.gov/pub/pao/reports/1999/wire_summary.pdf, 12th March 2003

- [13] NASA Manned Spacecraft Center, *Thermal Network Modeling Handbook*, reformatted by K&K Associates, Westminster, 2000
- [14] Pisacane, V. L. and Moore, R. C., *Fundamentals of Space Systems*, Oxford University Press, New York, 1994
- [15] Sakoda, D. and Horning, J. A., *Overview of the NPS Spacecraft Architecture and Technology Demonstration Satellite, NPSAT1*, Naval Postgraduate School (NPS), Monterey, 2002
- [16] Sellers, Jerry J., *Understanding Space, An Introduction to Astronautics*, 2nd edition, McGraw Hill Companies, New York, 2000
- [17] Space Systems Academic Group, Naval Postgraduate School, *NPSAT1 Drawing Package*, internal document, 2002
- [18] Space Systems Academic Group, Naval Postgraduate School, *NPSAT1 Mission System Interface Control Document*, internal document, 2002
- [19] Spectrolab Inc., *26.8% Improved Triple Junction (ITJ) Solar Cells*, <http://www.spectrolab.com/DataSheets/TNJCell/tnj.pdf>, 20th January 2003
- [20] Stoecker, H., *Taschenbuch mathematischer Formeln und moderner Verfahren*, 4th edition, Verlag Harri Deutsch, Frankfurt am Main, 1999
- [21] Structural Dynamics Research Corporation, *I-DEAS TMG Thermal Analysis User Guide*, I-DEAS 9 online help, 2001
- [22] Toh, K. C. and Ng, K. K., *Thermal Contact Conductance of Typical Interfaces in Electronic Packages Under Low Contact Pressure*, Institute of Electrical and Electronics Engineers (IEEE), 1997
- [23] Welch, J. W., *Review of NPSAT1 Thermal Control CDR Charts*, The Aerospace Corporation IOC 02.5445.32-27, 26 April 2002
- [24] Welch, J. W., *Review of NPSAT1 Thermal Control Delta-CDR Charts*, The Aerospace Corporation IOC 03.5445.32-15, 27 November 2002

- [25] Gruhlke, M., *CD to Diplomarbeit "Computer Aided Thermal Analysis of a Technology Demonstration Satellite"*, NPS Space Systems Academic Group, internal document, 2003

THIS PAGE INTENTIONALLY LEFT BLANK

INITIAL DISTRIBUTION LIST

- | | | |
|----|--|---|
| 1. | Defense Technical Information Center
8725 John J. Kingman Rd., STE 0944
Ft. Belvoir, VA 22060-6218 | 2 |
| 2. | Dudley Knox Library, Code 013
Naval Postgraduate School
Monterey, CA 93943-5100 | 2 |
| 3. | Research Office, Code 09
Naval Postgraduate School
Monterey, CA 93943-5138 | 1 |